

Flows in curved spaces

Doctoral Thesis**Author(s):**

Debus, Jens-Daniel

Publication date:

2016

Permanent link:

<https://doi.org/10.3929/ethz-a-010795142>

Rights / license:

[In Copyright - Non-Commercial Use Permitted](#)

Diss. ETH No. 23828

Flows in curved spaces

A thesis submitted to attain the degree of
DOCTOR OF SCIENCES of **ETH ZURICH**
(Dr. sc. ETH Zurich)

presented by
JENS-DANIEL DEBUS
MSc ETH Physics, ETH Zurich

born 15.12.1988

citizen of Germany

accepted on the recommendation of
Prof. Dr. Hans Jürgen Herrmann, examiner
Prof. Dr. Sauro Succi, co-examiner

2016

Acknowledgment

First, I would like to thank Prof. Hans J. Herrmann for his supervision and guidance during my PhD studies. Hans offered me the chance to enter the interesting field of computational physics. Under his supervision, I got involved into many interesting projects within an interdisciplinary environment. I highly appreciate his broad scientific knowledge, his experience and advice, in particular during the publication process.

I specially want to thank Dr. Miller Mendoza for his supervision and personal guidance during my PhD studies. I really appreciated his great expertise, his brilliant ideas as well as many fruitful discussions. Our numerous meetings provided many new impulses for this work.

I also would like to thank Prof. Sauro Succi for the co-supervision of my PhD studies, for many useful discussions and for valuable recommendations during the publication process.

I want to thank the whole Comphys group at ETH Zurich for all the help, for the pleasant working atmosphere, for the social activities and for all the nonsense that made our working life more enjoyable.

Finally, I would like to thank Zsófia Pröhle as well as my family for their unconditional support during the whole period of my PhD studies.

This work was financially supported by the European Research Council Advanced Grant “Fluid flow in complex and curved spaces” (ERC Adv. Grant No. 319968-FlowCCS).

Contents

Zusammenfassung	xi
Abstract	xv
1 Introduction	1
1.1 Overview and motivation	1
1.2 Numerical methods	9
1.3 Structure and organization	13
2 Lattice Boltzmann in curved space	15
2.1 A short review of Riemannian geometry	16
2.2 Kinetic theory in curved space	20
2.3 Gauss-Hermite quadrature	22
2.4 The lattice Boltzmann equation in curved space	24
2.5 Forcing term implementations	28
2.5.1 Third-order inertial forcing term	28
2.5.2 Second-order inertial forcing term	29
2.5.3 Cancelation of discrete lattice effects by moment cor- rections	30
2.5.4 Cancelation of discrete lattice effects by improved forc- ing term	31
2.5.5 Improved lattice derivatives	32
3 Dean instability in curved channels	35
3.1 Introduction	35

3.2	Validation: Flows through cylindrical channels	40
3.2.1	Geometry and simulation setup	41
3.2.2	Simulation results for cylindrical channels	42
3.2.3	Dependence on the grid resolution	47
3.3	Flows through double-curved channels	48
3.3.1	Geometry and simulation setup	48
3.3.2	Simulation results for double-curved channels	50
3.4	Summary	57
4	Poiseuille flow in curved spaces	59
4.1	Introduction	59
4.2	Simulation setup	61
4.3	Poiseuille flow in curved spaces	63
4.3.1	Transport in 2D curved media	63
4.3.2	Transport in 3D curved media	70
4.4	Comparison with a previous study	72
4.5	Method validation	73
4.5.1	Improvements by cancelation of discrete lattice effects	73
4.5.2	Finite resolution study	76
4.5.3	Flux conservation	77
4.6	Summary	78
5	Energy dissipation induced by curvature	81
5.1	Introduction	81
5.2	Computational and experimental setup	83
5.3	Dissipation induced by curvature	84
5.3.1	Flow past a deformation of space	84
5.3.2	Curvature-induced dissipation in soap films	89
5.4	Transport law for general geometries	89
5.5	Method validation	94
5.6	Summary	96

6 Quantum lattice Boltzmann in curved space	97
6.1 Introduction	97
6.2 The Dirac equation in curved space	100
6.3 Quantum lattice Boltzmann method	103
6.4 Method validation	106
6.4.1 Free quantum particle	107
6.4.2 Quantum harmonic oscillator	109
6.4.3 Dirac plane waves in curved space	112
6.5 Dirac formalism for strained graphene	115
6.6 Landau levels in curved graphene	120
6.7 Summary	126
7 Conclusion and Outlook	129
7.1 Summary and significance	129
7.2 Extensibility and future prospects	131
Appendix	135
A.1 Navier-Stokes equation from discrete LB equation	135
A.1.1 Cancelation of discrete lattice effects by moment corrections	138
A.1.2 Cancelation of discrete lattice effects by improved forcing term	141
A.2 Improved discrete gradient operator	143
References	145

List of Figures

1.1	Schematic illustration of flow through curved channels	2
1.2	Curved soap films	4
1.3	Lipid bilayer membrane	5
1.4	Simulation of flow through a randomly curved surface	6
1.5	Curved graphene sheet	8
1.6	Dirac cone	8
1.7	Lattice Boltzmann streaming step	11
2.1	Sketch of a Riemann manifold	16
2.2	Illustration of Riemann curvature	19
2.3	Streaming on the $D2Q17$ lattice	26
3.1	Geometry of the cylindrical channel	37
3.2	Geometry of the double-curved channel	38
3.3	Vorticity vs. Dean number for a cylindrical channel	44
3.4	Velocity profiles of vortex flow in a cylindrical channel	45
3.5	Critical Dean numbers vs. aspect ratio of a cylindrical channel	46
3.6	Error of the critical Dean number vs. grid resolution	47
3.7	Vorticity vs. Dean number for a double-curved channel	51
3.8	Critical Dean number vs. streamwise curvature radius \mathcal{R}_θ for a double-curved channel	52
3.9	Critical Dean number vs. cross-sectional curvature radius \mathcal{R}_ϕ for a double-curved channel	54
3.10	Velocity profiles of vortex flow in a double-curved channel . .	56

4.1	Velocity streamlines of a fluid driven through a curved medium with randomly distributed metric perturbations	60
4.2	Curved medium with regularly arranged metric perturbations	63
4.3	Flux vs. metric parameters for 2D regularly arranged metric perturbations	64
4.4	Flux deficit for two different types of metric perturbations .	66
4.5	General flux law in 2D and 3D	68
4.6	Curved medium with randomly arranged metric perturbations	68
4.7	Curved medium with mixed positive and negative metric perturbations	70
4.8	Flux vs. metric parameters for 3D regularly arranged metric perturbations	71
4.9	Improvement of the velocity field by cancelation of discrete lattice effects	74
4.10	Improvement of the divergence of the flow velocity by cancellation of discrete lattice effects.	75
4.11	Convergence of the numerical flux law with increasing grid resolution	76
4.12	Position-dependent numerical fluctuation of the conserved flux	77
5.1	Flow down a curved soap film compared to our numerical simulation	82
5.2	Surface with a Gaussian-shaped deformation.	85
5.3	Flow past a spatial deformation	86
5.4	Convergence of the flux to a stationary state	87
5.5	Flow past a randomly curved medium	90
5.6	Transport law for a curved medium with 16 metric perturbations	91
5.7	Dependence of the reciprocal permeabilities α and β on the geometry	93
5.8	Dependence of the simulation results on the grid resolution .	95
6.1	Graphene lattice	98
6.2	Probability density of a free quantum particle	108

6.3	Spread and total probability of a free quantum particle	108
6.4	Probability density of a quantum harmonic oscillator	110
6.5	Spread and total probability of a particle confined in a har- monic potential	111
6.6	Curved wavy surface	112
6.7	Dirac plane wave in curved space	113
6.8	Energy-momentum relation of a plane wave in curved space .	114
6.9	Position-dependent energy-momentum relation in rippled gra- phene	118
6.10	Position-dependent Fermi velocity and carrier density	119
6.11	Landau levels in a magnetic field	122
6.12	Landau level energies vs. energy quantum number for flat and curved graphene sheets	123
6.13	ξ vs. deformation parameters of the graphene sheet	125

Zusammenfassung

In dieser Arbeit betrachten wir verschiedene Arten von Strömungen in gekrümmten Räumen, wie sie in vielen physikalischen Systemen in der Natur vorkommen, angefangen von klassischen Flüssigkeiten in gekrümmten Kanälen bis hin zu Elektronenflüssen in gekrümmten Graphenschichten. Für die computergestützten Simulationen der Flüsse verwenden wir das Lattice-Boltzmann-Verfahren (LB), eine numerische Methode, die sich in den vergangenen Jahrzehnten wachsender Beliebtheit erfreut hat. Um Strömungen in gekrümmten Räumen zu beschreiben, verwenden wir eine verallgemeinerte Version der LB-Methode für Flüsse auf Mannigfaltigkeiten, welche erst kürzlich von M. Mendoza, S. Succi und H. J. Herrmann entwickelt wurde [1, 2]. Im Rahmen dieser Arbeit entwickeln wir diese LB-Methode weiter, indem wir die numerische Genauigkeit und Effizienz des Algorithmus verbessern.

Das erste physikalische Phänomen, welches wir in dieser Arbeit betrachten, ist die Dean-Instabilität, eine Strömungs-Instabilität, die in Kanälen mit gekrümmten Wänden auftritt. Die Dean-Instabilität zeichnet sich durch einen krümmungsabhängigen Übergang von laminarer Strömung zu Wirbelströmung aus und wurde bereits umfassend an rechteckigen Kanälen studiert. Im Rahmen dieser Arbeit untersuchen wir das Phänomen in komplexeren Kanalgeometrien, welche neben einer strömungsgerichteten Kanalkrümmung auch eine Krümmung in Breitenrichtung besitzen. Für die Strömungssimulationen verwenden wir die LB-Methode in krummlinigen Koordinaten, welche perfekt auf die Geometrie des Kanals abgestimmt sind. Interessanterweise stellt sich heraus, dass die Dean-Instabilität entscheidend

vom Verhältnis der beiden Kanalkrümmungen abhängt. Für sehr stark gekrümmte Kanäle beobachten wir sogar Strömungsübergänge höherer Ordnung, welche durch eine Vielzahl von Flusswirbeln gekennzeichnet sind.

Während die Strömung bei der Dean-Instabilität die Krümmung der Kanalwände lediglich als externe Randbedingung wahrnimmt, die die Flüssigkeit auf das Innere des Kanals eingrenzt, existieren auch hydrodynamische Systeme mit einer intrinsischen Raumkrümmung. Beispiele hierfür bilden Seifenblasen, gekrümmte Lipid-Doppelschichten oder Elektronentransport in Graphen, einem der fasziniersten Materialen des letzten Jahrzehnts aufgrund seiner aussergewöhnlichen mechanischen, elektronischen und optischen Eigenschaften. All diese Systeme besitzen ein hydrodynamisches Regime, in welchem sie effektiv als zweidimensionale Flüssigkeit auf einer gekrümmten Oberfläche beschrieben werden können. Dabei ruft die komplexe Wechselwirkung zwischen der Flüssigkeit und der Raumkrümmung überraschende neue Effekte hervor, die wir im Rahmen dieser Arbeit genauer untersuchen werden. Dazu simulieren wir Strömungen über intrinsisch gekrümmte Oberflächen, die durch einen allgemeinen metrischen Tensor beschrieben werden können. Interessanterweise finden wir, dass der Fluss durch einen intrinsisch gekrümmten Kanal nur von der mittleren Deformation des Raumes abhängt, nicht aber von der spezifischen örtlichen Verteilung der Krümmung. Diese Erkenntnis erlaubt es uns, ein allgemeines Flussgesetz für eine grosse Familie von zwei- und dreidimensionalen gekrümmten Räumen zu formulieren. Noch erstaunlicher ist die Beobachtung, dass Flüssigkeiten in gekrümmten Räumen selbst in der kompletten Abwesenheit von Wänden und Hindernissen einen Energieverlust erfahren, der allein auf die Krümmung des Raumes zurückzuführen ist. Tatsächlich erscheint es zunächst widersprüchlich, dass eine geometrische Eigenschaft des Raumes Energiedissipation in Flüssigkeiten verursachen kann. Wir erklären dieses faszinierende Phänomen durch das Auftreten von viskosen Kräften innerhalb der Flüssigkeit, welche von der Raumkrümmung hervorgerufen werden und infolgedessen zu einer physikalischen Energiedissipation führen. Wir zeigen ausserdem, dass Strömungen in gekrümmten Räumen einem nichtlinearen

Transportgesetz folgen, welches der Form nach dem Darcy-Forchheimer Gesetz [3] ähnelt. Darüberhinaus charakterisieren wir die Permeabilität von gekrümmten Medien in Abhängigkeit von der räumlichen Deformation.

Schliesslich widmen wir uns den elektronischen Eigenschaften von Graphen, indem wir die elektronische Bandstruktur von Graphenschichten bei niedrigen Temperaturen mithilfe des Dirac-Formalismus beschreiben. Dazu verwenden wir die Quanten-Lattice-Boltzmann-Methode (QLB) [4], welche wir zunächst auf gekrümmte Räume verallgemeinern. Damit sind wir prinzipiell in der Lage, Graphenschichten in beliebigen Formen numerisch zu simulieren. Im Rahmen dieser Arbeit konzentrieren wir uns auf wellige Graphen-Oberflächen, für welche wir verschiedene Eigenschaften, wie z.B. die ortsabhängige Fermi-Geschwindigkeit sowie die inhomogene Ladungsträgerdichte [5, 6], korrekt reproduzieren können. Darüberhinaus simulieren wir Graphenschichten in einem äusseren Magnetfeld, wobei wir eine krümmungsabhängige Verschiebung der Landau-Energieniveaus beobachten. Diese Verschiebung wurde — unseres Wissens nach — bisher noch nicht beobachtet und regt zu weiteren zukünftigen Untersuchungen an.

Abstract

In this work we study flows through curved spaces, starting from classical fluid flows through curved channels and ending with electron flows in curved graphene sheets. For our numerical simulations, we use the lattice Boltzmann (LB) method, a powerful numerical technique, which has gained increasing popularity during the last decades. To simulate flows in curved spaces, we improve and extend the LB method on manifolds, which has been proposed recently by M. Mendoza, S. Succi and H. J. Herrmann [1, 2].

As a first application, we study the Dean instability. This flow instability occurs in channels with curved walls and is characterized by a curvature-dependent transition from laminar flow to vortex flow. While the Dean instability has been widely studied for rectangular channels, we simulate more complex channel geometries by curving the channel in both streamwise and spanwise direction, using the LB method in curvilinear coordinates. We find that the flow instability depends significantly on the relative strength of the streamwise and spanwise curvature. For strongly curved channels, we even observe higher-order transitions, characterized by a multitude of counter-rotating vortices.

While for the Dean instability the curvature of the channel walls affects the flow only as an extrinsic constraint, confining the fluid inside the channel, there also exist hydrodynamic systems with an intrinsic curvature of space. Some examples are curved soap films, lipid bilayer membranes or electron flow in graphene, being one of the most fascinating materials of the last decade due to its extraordinary mechanical, electronic and optical properties. In the hydrodynamic regime, all these systems can effectively be

described as a two-dimensional viscous fluid, moving on a curved surface. The complex interaction between the fluid motion and the spatial curvature gives rise to surprising macroscopic effects, as studied in the present work. To this end, we simulate flow through intrinsically curved spaces, which are described by a general metric tensor. Interestingly, we find that the mass flow through an intrinsically curved channel depends only on the average deformation of space, but not on the specific distribution of curvature. This allows us to formulate a general flux law, applicable to a wide family of curved spaces in two and three dimensions. More surprisingly, we find that even in the complete absence of solid walls or obstacles, the free motion of fluids exhibits loss of energy only due to the intrinsic curvature of space. It appears counter-intuitive that a geometrical property of space yields physical dissipation in fluid flows. We explain this intriguing observation by curvature-induced viscous stresses, which create velocity gradients between adjacent fluid layers, leading to an irreversible dissipation of energy. We show that flows in curved spaces follow a non-linear transport law, resembling in form Darcy-Forchheimer's law [3]. In addition, we characterize the permeability of curved media in terms of the spatial deformation.

Finally, we study electron flow in graphene from a different approach by using the Dirac formalism, which describes the electronic band structure of graphene sheets at low temperatures. By improving and extending the quantum lattice Boltzmann (QLB) method [4] to curved spaces, we are able to simulate graphene sheets of, in principle, arbitrary smooth shapes. In this work, we focus on rippled graphene sheets, for which we correctly recover the space-dependent Fermi velocity and the inhomogeneous carrier density predicted in Ref. [5, 6]. Furthermore, we observe a curvature-dependent shift of the Landau levels, arising in a magnetic field, which — to the best of our knowledge — has not been reported before and deserves future investigation.

Chapter 1

Introduction

1.1 Overview and motivation

Curved spaces are encountered in many physical systems in nature, ranging from biological nanomembranes all the way up to general relativity on cosmological scales. Despite the diversity of applications, many of these systems share common properties, which can be analyzed by means of effective conservation equations. As an example, in many systems, the collective motion of particles constitutes a hydrodynamic flow, which can be described by the Navier-Stokes conservation equations for viscous fluids,

$$\partial_t \rho + \partial_i(\rho u^i) = 0, \quad \partial_t(\rho u^i) + \partial_j T^{ij} = 0, \tag{1.1}$$

characterizing the time evolution of the fluid density ρ and velocity u , where T^{ij} denotes the energy-stress tensor of the fluid. In their general form, the Navier-Stokes equations account for various hydrodynamic phenomena, such as convective and hydrostatic effects as well as viscous forces caused by shear and bulk stresses within the fluid.

The understanding of hydrodynamic flows in the presence of spatial curvature is essential for many applications, ranging from practical engineering to fundamental physical questionings. One of these applications having attracted fluid dynamics researchers for over a hundred years is flow through

¹In the course of this thesis, we use the abbreviations $\partial_t := \frac{\partial}{\partial t}$ and $\partial_i := \frac{\partial}{\partial x^i}$.

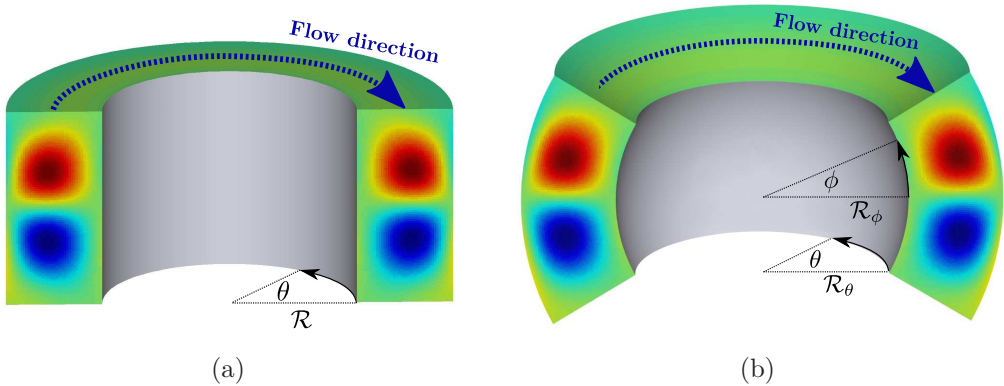


Figure 1.1: **Schematic illustration of flow through curved channels.** (a) Flow through a single-curved channel made of two concentric cylinders with curvature radius \mathcal{R}_θ . The colors on the channel cross-sections at the inlet and outlet illustrate the pair of counter-rotating vortex tubes, oriented in clockwise (blue) or counterclockwise direction (red) around the z -axis. (b) Flow through a double-curved channel, made of two coaxial ellipsoids. In addition to the streamwise curvature of radius \mathcal{R}_θ , the double-curved channel possesses a cross-sectional curvature of radius \mathcal{R}_ϕ .

curved channels, in which the motion of the fluid is confined by curved channel walls. Since the flow is considerably affected by the curvature of the boundaries, interesting flow instabilities can be observed. A popular example is the *Dean instability*, characterized by a transition from primary laminar flow to secondary vortex flow due to increasing centrifugal forces along the curved boundary. The bifurcation is named after William R. Dean, who in 1928 showed analytically that the fully developed flow between two concentric cylinders (see Figure 1.1(a)) can be characterized by a single parameter only, the Dean number $\mathcal{D}e$. This dimensionless parameter depends on the Reynolds number $\mathcal{R}e$ as well as on the channel geometry [7]:

$$\mathcal{D}e := \mathcal{R}e \cdot \sqrt{\frac{d}{\mathcal{R}}},$$

where d denotes the channel width and \mathcal{R} the curvature radius of the inner cylinder wall. In particular, Dean showed by a stability analysis that the laminar flow between two concentric cylinders becomes unstable for Dean

1.1. OVERVIEW AND MOTIVATION

numbers larger than a critical value of $\mathcal{D}e_c \approx 36$. Above this value, pairs of counter-rotating streamwise-oriented vortices develop, constituting the “Dean vortex flow”. The theoretical predictions by Dean have been confirmed in various experiments [8, 9] and have even been extended to channels of different aspect ratios, using high-accuracy linear stability analysis [10, 11, 12].

All the studies mentioned above consider very idealized channel geometries, namely channels with rectangular cross sections, which are uniformly curved along the streamwise direction only. Thinking of practical engineering applications (e.g. water ducts), however, channels do not possess perfectly rectangular cross sections, but can also be bent perpendicularly to the streamwise direction, for instance under the influence of gravity. The resulting cross section becomes the section of a circular ring, as illustrated in Figure 1.1(b), imposing a second, cross-sectional curvature. As part of this work, we study the Dean instability in such double-curved channels, which, to the best of our knowledge, has never been done before. We show that the critical Dean number, at which the transition to vortex flow occurs, depends considerably on both the streamwise and the cross-sectional curvature. In addition, for strongly-curved channels, we even observe higher-order transitions to vortex flow with a multitude of counter-rotating vortex cells.

While in the case of curved channels, the flow is influenced by the extrinsic curvature of the channel walls, there is a variety of physical systems, in which the embedding space itself is intrinsically curved. The most famous example is Albert Einstein’s general theory of relativity, which relates the local curvature of space-time to the surrounding matter and energy according to the Einstein field equations [14]. In such curved spaces, fluids can be described by the covariant Navier-Stokes equations,

$$\partial_t \rho + \nabla_i (\rho u^i) = 0, \quad \partial_t (\rho u^i) + \nabla_j T^{ij} = 0, \quad (1.2)$$

being a generalization of Eq. (1.1), where ∇ denotes the covariant derivative and T^{ij} the energy-momentum tensor of the fluid.

Although curved spaces are commonly associated with general relativity, there also exist various fields of application on Earth dealing for example

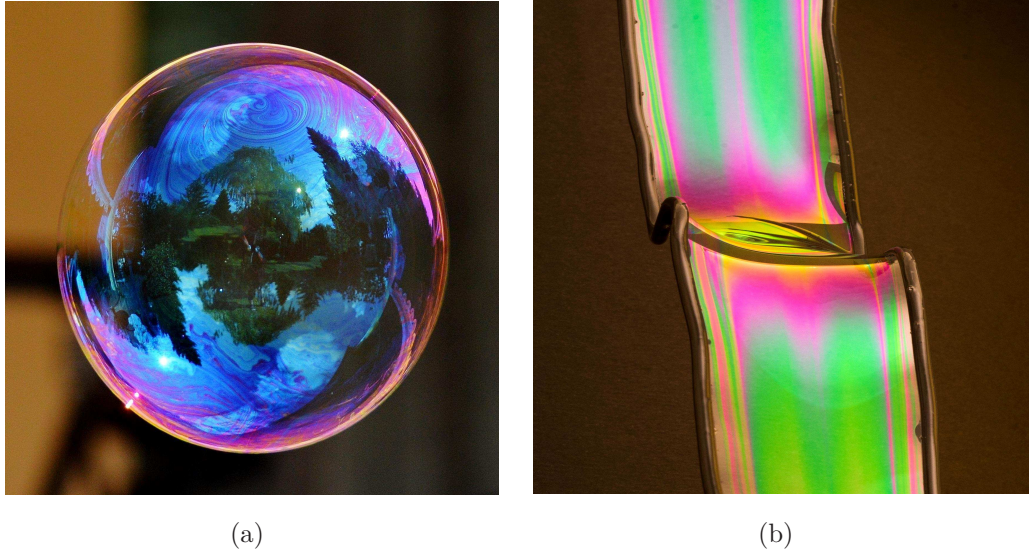


Figure 1.2: **Curved soap films.** (a) A soap bubble, consisting of a curved, two-dimensional film of soapy water. [Reprinted with permission from Ref. [13].] (b) A soap film, spanned between two curved wires. The soap film flows downwards by gravity, forming a two-dimensional fluid flow on a curved surface. [Own picture.]

with flows on curved two-dimensional surfaces. A daily-life example is given by soap bubbles (see Figure 1.2(a)), consisting of a curved film of soapy water. Since the thickness of the soap film is negligibly small, soap bubbles are commonly described as a two-dimensional fluid moving on a curved surface [15, 16]. Soap films can be produced in a wealth of shapes and are thus particularly interesting for the experimental study of two-dimensional fluid flow [17, 18, 19]. As an illustration, Figure 1.2(b) depicts a self-made photo of a flowing soap film, spanned between two curved wires.

Another important example of flow on curved surfaces are lipid bilayer membranes in microbiology, which constitute the envelope of most of the cell components, such as the cell nucleus, the organelles, the transport vesicles and the cell membrane itself. Figure 1.3(a) depicts an image of a bacterium, whose outer shell consists of a lipid bilayer, serving as a containment unit with a variety of biological functions (e.g. barrier for ions and proteins). The schematic structure of a lipid bilayer is illustrated in Figure 1.3(b). Around 1970, researchers started to recognize that above a certain transition

1.1. OVERVIEW AND MOTIVATION

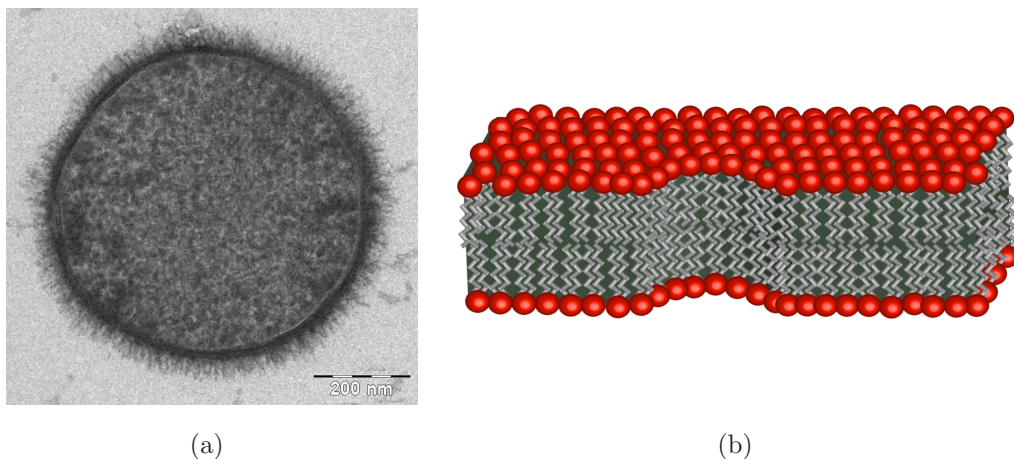


Figure 1.3: **Lipid bilayer membrane.** (a) Image of a bacterium measured by transmission electron microscopy. The circular cell membrane consists of lipid bilayer (and a fuzzy coat of long-chain sugar molecules attached to the cell membrane). [Reprinted with permission from Ref. [20].] (b) Schematic image of a curved lipid bilayer, consisting of a double layer of lipid molecules. The red balls represent the hydrophilic head groups, while the zig-zag-shaped chains denote the lipophilic tails of the lipid molecules. The collective motion of the lipids can be described as a viscous fluid, known as “membrane fluidity”. [Reprinted with permission from Ref. [21].]

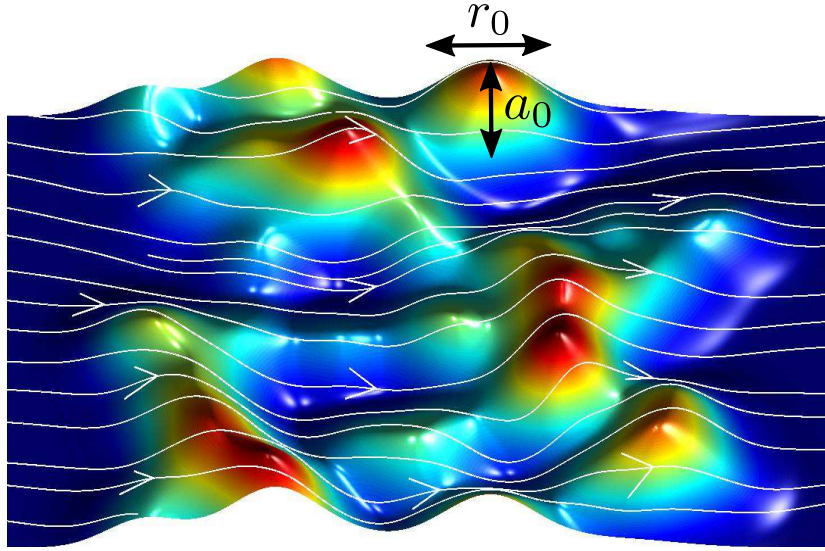


Figure 1.4: Simulation of flow through a randomly curved surface. The white lines depict the flow streamlines of a fluid moving through a curved surface, composed of randomly arranged metric perturbations of amplitude a_0 and width r_0 . The colors correspond to the local amount of deformation, quantified by the diagonal components of metric tensor, from blue (flat space) to red (high deformation).

temperature, the lipid molecules are able to move freely along the bilayer membrane, showing hydrodynamic properties, such as diffusion and viscosity [22, 23]. Since then, the membrane fluidity of lipid bilayers has been subject to numerous studies, showing that the bilayers can effectively be described as a two-dimensional fluid [24, 25, 26], which has been confirmed experimentally [27, 28, 29]. Beside lipid bilayers, there exist many examples of curved interfaces behaving as two-dimensional viscous fluids, such as molecular films around emulsions or aerosol droplets, foam bubbles [30, 31], and, on larger scales, the Earth’s atmosphere as well as the photosphere of the Sun [32, 33].

In the present work, we study the effects of intrinsic curvature on channel flow by considering a channel with local sources of curvature, implemented as perturbations δg of the flat Riemann metric tensor g . The perturbations are regularly or randomly arranged within the medium and are characterized by their amplitude a_0 , width r_0 and number density n . As an illustration, Figure

1.1. OVERVIEW AND MOTIVATION

1.4 depicts our simulation of fluid flow on a randomly curved surface. For different metric perturbations, we study the mass flow in the stationary state and establish a connection between the flux and the curvature parameters. Surprisingly, we find that — in the wide parameter range considered — the flux depends neither on the spatial arrangement nor on the specific shape of the metric perturbations, but only on the average metric perturbation $\langle \delta g \rangle$. We combine our findings into an empirical transport law, generalizing previously published results [1].

More surprisingly, we observe that even in the complete absence of solid walls or obstacles, the free motion of fluids exhibits loss of energy due only to the intrinsic curvature of space. We find that local sources of curvature generate viscous stresses due to the inertial forces, which tend to narrow or widen the streamlines (see Figure 1.4) and thus introduce velocity gradients between adjacent fluid layers. Consequently, the viscous stresses lead to an irreversible dissipation of energy, induced indirectly by the spatial curvature. In addition, we show that the viscous and inertial forces result in a non-linear transport law,

$$|\nabla P| = \alpha \nu \Phi + \beta \Phi^2,$$

where Φ denotes the mass flow, ∇P the pressure gradient, ν the kinematic viscosity, and α and β are parameters, which depend on the spatial deformation of the medium.

Finally, we study the electronic properties of an extraordinary material, which has attracted more and more attention over the last ten years due to its exceptional mechanical, electronic and optical properties [34, 35, 36, 37]: *Graphene*. Graphene consists of a single layer of carbon atoms, arranged on a honeycomb crystal structure (see Figure 1.5), and is the first two-dimensional material discovered. Recent research has shown that graphene possesses a hydrodynamic regime, in which the electronic transport satisfies the Navier-Stokes equations [38, 39]. In this work, we pursue a different approach to describe the electronic properties of graphene, based on the fact that the low-energetic electronic states are well-described by the massless Dirac equation [34, 37, 36], which can be derived from a tight-binding model.

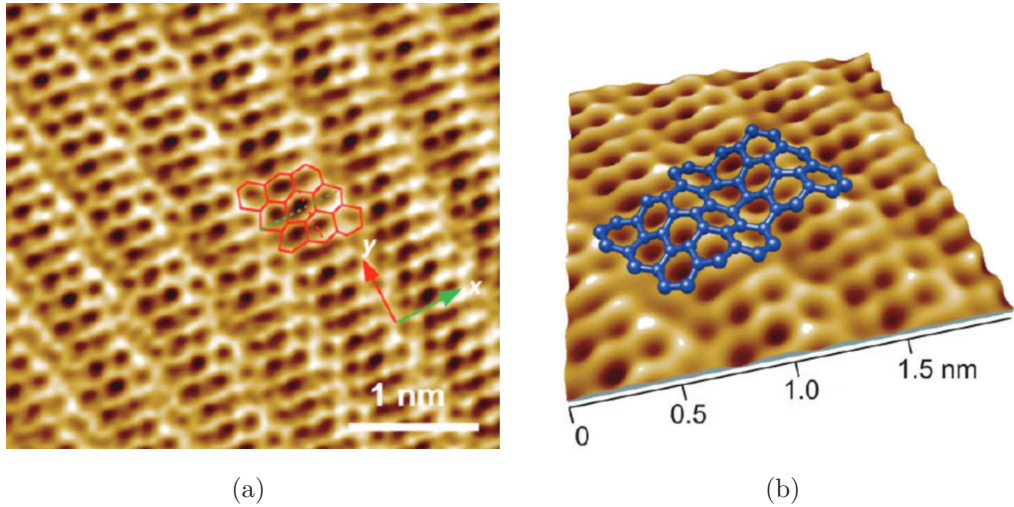


Figure 1.5: Curved graphene sheet. (a) Image of a graphene surface, measured with a transmission electron microscope by Y. Mao *et al.* [40]. The hexagonal atomic lattice structure is well visible. The long parallel strips correspond to periodic surface ripples, generating an out-of-plane curvature. (b) Graphene sheet at finer resolution. The atoms and bonds are highlighted by the blue balls and sticks, respectively. [Reprinted with permission from Ref. [40]. Copyright (2011) American Chemical Society.]

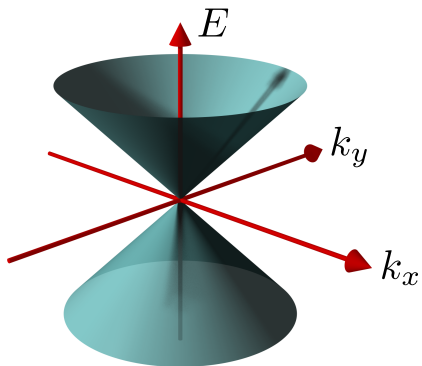


Figure 1.6: Dirac cone. At low energies, the electronic band structure of graphene possesses a linear energy-dispersion relation, $E = v_F \|\mathbf{k}\|$, where E denotes the energy, v_F the Fermi velocity and $\mathbf{k} = (k_x, k_y)$ the wave vector of the electrons. [Reprinted with minor editing with permission from Ref. [41].]

1.2. NUMERICAL METHODS

In its original context, the Dirac equation describes the space-time evolution of charged relativistic quantum particles, represented by a wave function Ψ , in line with quantum mechanics and special relativity:

$$i\gamma^\mu \partial_\mu \Psi = m\Psi, \quad (1.3)$$

where γ^μ denote the Dirac matrices and m the mass of the particle. In the context of graphene, the wave function Ψ represents electrons and holes in the low-energetic states, which are characterized by a linear energy-dispersion relation, the “Dirac cone” (see Figure 1.6).

Although graphene is often modeled and visualized as an idealized, perfectly flat two-dimensional sheet, real graphene sheets are subject to intrinsic strain, lattice impurities and external influences, such as mechanical or electromagnetic forces. As a consequence, graphene sheets typically possess local lattice deformations, leading to both in-plane and out-of-plane curvature, which for example has been observed in the form of intrinsic ripples (see Figure 1.5) [42, 43]. This gives rise to new curvature-induced effects, which we study in the present work by using numerical simulations. In the course of this, we correctly recover the space-dependent Fermi velocity as well as the inhomogeneous carrier density, predicted in Refs. [5, 6]. In addition, we study rippled graphene surfaces in a magnetic field and show that the Landau energy levels are shifted due to the curvature of the sheets. All these effects influence the electronic properties of graphene significantly and are thus indispensable for the full understanding of electron transport in curved graphene sheets.

1.2 Numerical methods

Understanding the dynamics of hydrodynamic systems requires solving complex nonlinear equations (the Navier-Stokes equations (1.2)), rendering the analytic treatment of practical problems extremely difficult, if not impossible. Hence, various numerical methods have been developed to study the motion of hydrodynamic flow. Whereas many computational techniques try

to directly solve the Navier-Stokes equations, we tackle the problem from the microscopic point of view, based on the Boltzmann transport equation [44]:

$$\frac{df}{dt} = \frac{\partial f}{\partial t} + v^i \frac{\partial f}{\partial x^i} + F^i \frac{\partial f}{\partial v^i} = \mathcal{C}[f].$$

The Boltzmann equation describes the motion of fluid particles in terms of a statistical distribution function $f = f(x, v, t)$, which depends on the positions x and microscopic velocities v of the fluid particles. Here, F^i represents internal or external forces (e.g. inertial forces or gravity), and $\mathcal{C}[f]$ denotes the Boltzmann collision operator, accounting for the forces acting between the particles in collisions. The collective motion of the microscopic particles constitutes the fluid flow, whose macroscopic density ρ and velocity u^i are given by the moments of the distribution function,

$$\rho = \int f d^D v \quad \text{and} \quad \rho u^i = \int f v^i d^D v,$$

where D denotes the spatial dimension of the system. In the hydrodynamic limit of small Knudsen numbers, the Boltzmann equation converges to the Navier-Stokes equation (1.1), as can be shown rigorously by a Chapman-Enskog expansion.

In computer simulations, the Boltzmann equation is solved locally on the grid points of a uniform, equally spaced lattice. This method, known as the “lattice Boltzmann (LB) method”, is a relatively new and popular computational technique for complex fluid systems. The LB method describes the motion of fictive microscopic particles, which are represented by discretized distribution functions f_λ , moving consecutively from lattice point to lattice point according to the LB equation [45],

$$f_\lambda(x + c_\lambda \Delta t, t + \Delta t) - f_\lambda(x, t) = \mathcal{C}[f], \quad (1.4)$$

where Δt denotes the time step size, being identical to the lattice spacing. Each time step consists of a collision step, represented by the collision operator $\mathcal{C}[f]$, and a streaming step (corresponding to the left-hand side of Eq. (1.4)), in which the fictitious particles propagate on the lattice with discrete velocities c_λ , as illustrated in Figure 1.7.

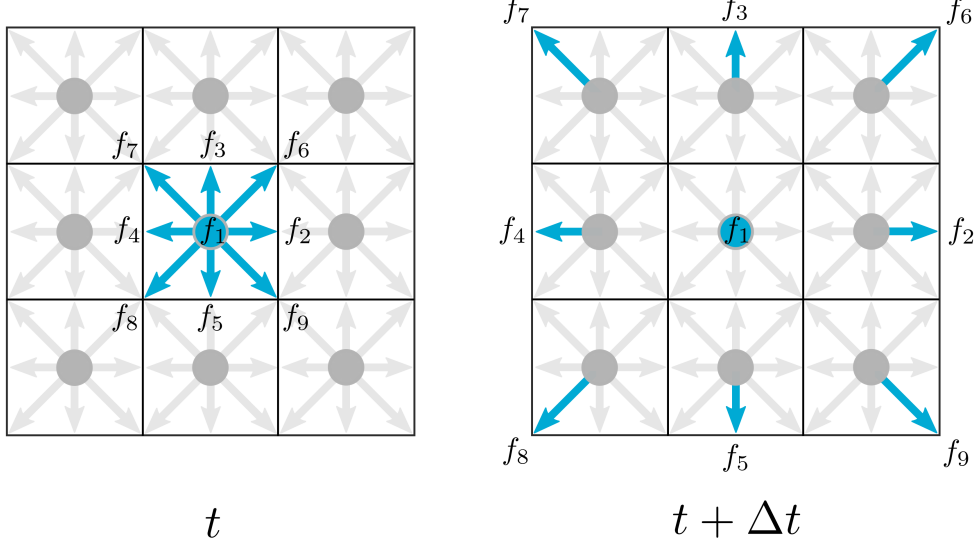


Figure 1.7: **Lattice Boltzmann streaming step.** The lattice distribution functions $f_\lambda(x, t)$ stream from grid point x to grid point $(x + c_\lambda \Delta t)$ during each time step $t \rightarrow (t + \Delta t)$ (shown here for the two-dimensional $D2Q9$ -lattice, consisting of 9 lattice vectors c_λ).

During the last two decades, the LB method has gained increasing popularity due to its computational simplicity, easy handling of complex geometries, and high flexibility with respect to parallel computing. Compared to direct solvers of the Navier-Stokes equations, the LB method benefits from numerous advantages: Firstly, the structure of the LB equation is relatively simple compared to the Navier-Stokes equations, since the LB equation contains neither nonlinear terms in f_λ nor derivatives. Secondly, by splitting each time step into a streaming and a collision part, the LB equation can easily be parallelized to increase the efficiency of the method for large system sizes. Thirdly, complex geometries and boundary conditions, as they appear for example in porous media or in particle-laden flows, can be implemented relatively easily. Finally, the LB method appeals because of its direct physical interpretability as the molecular description of a fluid. The increasing popularity of the LB method demonstrates its wide applicability for complex fluid systems and beyond, although — as for every numerical

method — there are some limitations, concerning for example high-Mach number flows, strongly compressible flows or highly-viscous fluids.

In 2013, the LB method has been extended to general Riemannian manifolds by M. Mendoza, S. Succi and H. J. Herrmann [1, 2], solving the covariant Navier-Stokes equations (1.2) for fluids in curved spaces. This opens the possibility to simulate fluid flow in nearly arbitrary, smooth geometries, characterized by a general metric tensor. Once the metric tensor is handed to the LB method, the algorithm adapts automatically to the new geometry, since the underlying LB equation is implemented in a covariant way. Thus, the LB method on manifolds naturally generalizes previous implementations of the LB equation in non-Cartesian coordinate systems, for example for the study of axisymmetric flow in polar coordinates [46]. The geometry of the curved space enters the LB equation (1.4) through an additional forcing term, representing the inertial forces on the manifold. By introducing curvature in this way, the fictitious particles continue propagating on a flat, equally spaced lattice, “feeling” the curvature of manifold due only to the inertial forces, which drive them along the geodesic lines. Thus, even for strongly warped spaces, interpolation between lattice points is avoided, and the on-grid streaming and collision steps remain unchanged.

In the course of this thesis, we improve the LB method on manifolds considerably by canceling spurious discrete lattice effects, which originate from the forcing term of the LB equation and lead to spurious source terms in the Navier-Stokes equations (1.2). By significantly reducing the discrete lattice effects, we are able to increase the accuracy of the LB method introduced in Ref. [1, 2] from first-order to second-order in space and time.

While hydrodynamic flows through curved spaces can be described by the LB equation on manifolds, the probability flow of charged relativistic quantum particles follows the Dirac equation (1.3), which can also be used to describe the electronic properties of graphene at low temperatures. However, due to the high complexity of the Dirac formalism in curved space, analytical solutions for the quantum wave functions can only be derived for very simplified and idealized systems, as considered for example in Ref. [5, 6].

1.3. STRUCTURE AND ORGANIZATION

In experiments, graphene sheets appear in arbitrarily complex shapes, giving rise to high local strains and curvatures, which cannot be treated analytically any more and thus require numerical methods. In the course of this work, we also develop a numerical solver which is capable of simulating electron transport in curved graphene sheets. The solver is based on the quantum lattice Boltzmann method (QLB), first introduced by S. Succi and R. Benzi in 1993 [4] and further developed by D. Lapitski, P. Dellar, S. Palpacelli and S. Succi [47, 48]. In this thesis, we extend the QLB method to curved manifolds and apply our solver to both charged relativistic quantum particles in curved spaces and electronic transport in curved graphene sheets. We validate our method on a couple of analytically solvable benchmark problems, such as free quantum particles, the quantum harmonic oscillator and plane wave solutions, before we apply our method to curved graphene surfaces.

Recently, it has been shown that for graphene under nonuniform strain, the Dirac Hamiltonian needs a correction to take into account the strain-induced shift of the Dirac points [6]. In this work, we implement this correction by using an effective metric tensor, which automatically leads to the correct Hamiltonian. Thus, we show that also nonuniformly strained graphene can be described by the original Dirac formalism in curved space-time, which has not been reported before.

1.3 Structure and organization

This work is organized as follows:

In **Chapter 2**, the lattice Boltzmann (LB) method in curved space is presented. After a short summary of the basic ingredients of Riemannian geometry, we shortly review kinetic theory in curved spaces, based on the Boltzmann equation on manifolds. After the key concepts of kinetic theory have been introduced, we present the LB method on manifolds, used for all fluid simulations in Chapters 3-5.

Chapter 3 deals with the Dean instability in differently curved channels, modeled in general coordinates by using the LB method on manifolds. Start-

ing with the validation of our model by measuring the bifurcation points in cylindrical channels, we proceed by studying the Dean instability in double-curved channels, using ellipsoidal coordinates. To this end, we measure the dependence of the bifurcation points on the streamwise and cross-sectional curvature of the double-curved channel.

In **Chapter 4**, we study Poiseuille flow in intrinsically-curved spaces by introducing local sources of spatial curvature, implemented as perturbations of the metric tensor. Using the LB method on manifolds, we analyze the dependence of the mass flow on the geometrical properties of space by considering differently curved media in two and three dimensions. As a conclusion, we formulate a general flux law, describing the transport properties of Poiseuille flow for a broad family of curved spaces. We compare our findings to a previous study and validate a considerable improvement of our method, achieved by canceling discrete lattice effects.

In **Chapter 5**, we present the most interesting finding of this work: energy dissipation in flows through curved spaces. Using the LB method on manifolds, we show that a freely moving fluid exhibits energy loss due only to the intrinsic curvature of space. We discuss the consequences of curvature-induced dissipation and characterize the transport properties of intrinsically-curved media by a nonlinear transport law. Furthermore, we present a daily-life application of this effect: curved soap films.

In **Chapter 6**, we introduce the quantum lattice Boltzmann (QLB) method, extended to general manifolds, and use this numerical method to solve the Dirac equation in curved spaces. Besides the standard solutions for relativistic quantum particles, used to validate our algorithm, the most interesting application of the QLB method is electronic transport in graphene, which can be described by the Dirac equation on manifolds. In particular, we measure the theoretically predicted space-dependent Fermi velocity and the inhomogeneous carrier density in rippled graphene. Furthermore, we study the dependence of the Landau levels, arising in the presence of a magnetic field, on the curvature of the graphene sheet.

Chapter 2

Lattice Boltzmann in curved space

The lattice Boltzmann (LB) method has been developed during the last decades to simulate fluids by means of simple arithmetic operations instead of directly solving the complicated macroscopic equations of continuum fluid mechanics (the Navier-Stokes equations). The method itself is based on the Boltzmann equation, which describes the motion of the microscopic fluid particles from the perspective of the kinetic theory of gases. For a review of the standard LB method we refer to Ref. [49, 50, 51]. Because of its simplicity and straightforward parallelizability, the LB method has gained more and more popularity among scientists and engineers in the past. While it was originally designed to simulate fluids, the LB method has been applied to electrodynamics [52], magnetohydrodynamics [53], relativistic flows [54] and even to quantum mechanics [4]. While most of the LB applications operate in standard Cartesian coordinates, the LB method has recently been extended to general Riemannian manifolds [1, 2], enabling us to simulate fluid flow in nearly arbitrary, smooth geometries, which offers a variety of interesting new applications.

In this work, we improve the computational method introduced in Ref. [2] in terms of accuracy and efficiency, as will be explained in the following sections. In this context, the treatment of spurious discrete lattice effects, originating from the forcing term of the LB equation (cf. Ref. [55]), plays

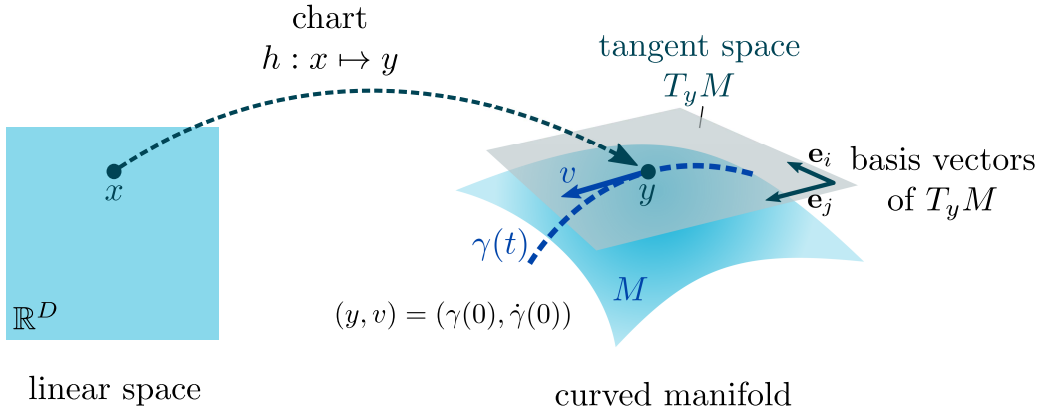


Figure 2.1: **Sketch of a Riemann manifold.** The manifold M is locally homeomorphic to the linear space \mathbb{R}^D , meaning that every point y on the manifold is described as the image of a point $x \in \mathbb{R}^D$ under a local chart h . The velocity v of an object at point y can be defined as the tangent vector of a curve $\gamma(t)$ passing through y . Thus, by construction, velocity vectors are tangential to the manifold and form a linear vector space, the tangent space $T_y M$.

an essential role.

2.1 A short review of Riemannian geometry

At first, we will shortly review the basic ingredients of Riemannian geometry, used in our model to simulate fluids in curved space. Mathematically, a D -dimensional curved space is represented by a *Riemannian manifold* M , which is locally described by a smooth diffeomorphism h , called the *chart*, see Figure 2.1. The set of tangential vectors attached to each point y on the manifold is called the *tangent space* $T_y M$. In the fluid model, all vectorial quantities (e.g. fluid velocity \vec{u} , driving force \vec{F} , pressure gradient $\vec{\nabla} P$) are represented as elements of the tangent space. A natural basis of the tangent space is the *standard basis* $(\mathbf{e}_1, \dots, \mathbf{e}_D) = (\frac{\partial h}{\partial x^1}, \dots, \frac{\partial h}{\partial x^D})$, defined by the derivatives of the chart h .

To measure the length of a vector or the angle between two vectors, the tangent space is equipped with a *metric tensor* g , acting as a generalized dot product. In local coordinates, the components of the metric tensor are

given by

$$g_{ij}(x) = \langle \mathbf{e}_i(x), \mathbf{e}_j(x) \rangle = \left\langle \frac{\partial h}{\partial x^i}, \frac{\partial h}{\partial x^j} \right\rangle \quad (2.1)$$

where $\langle \cdot, \cdot \rangle$ denotes the standard Euclidean scalar product. Given the metric tensor, the norm of a vector $v = v^i \mathbf{e}_i \in T_y M$ can be defined as $\|v\|_g = \sqrt{g(v, v)} = \sqrt{v^i g_{ij} v^j}$ ¹. For each vector $v = v^i \mathbf{e}_i \in T_y M$ there exists a corresponding dual vector $v^* = v_i dx^i \in T_y^* M$ in the cotangent space, which is spanned by the differential 1-forms $dx^i = g(\mathbf{e}_i, \cdot)$. The coefficients v_i of the dual vector are typically denoted by a lower index and are related to the upper-index coefficients v^i by contraction with the metric tensor, $v_i = g_{ij} v^j$ (*index lowering*). Equivalently, $v^i = g^{ij} v_j$ (*index raising*), where g^{ij} denotes the inverse of the metric tensor. The upper-index coefficients v^i of a vector v are typically called *contravariant components*, whereas the lower-index coefficients v_i of the dual vectors v^* are known as *covariant components*.

A necessary feature for the description of objects moving on the manifold is *parallel transport* of vectors along the manifold. To this end, the tangent space is equipped with a *covariant derivative* ∇ (*Levi-Civita connection*), which connects the tangent spaces at different points on the manifold and thus allows to transport a tangent vector from one tangent space to the other along a given curve $\gamma(t)$. The covariant derivative can also be viewed as the orthogonal projection of the Euclidean derivative ∂ onto the tangent space, such that the tangency of the vectors is preserved during the transport. In local coordinates, the covariant derivative is fully characterized by its connection coefficients Γ_{jk}^i (*Christoffel symbols*), which are defined by the action of the covariant derivative on the basis vectors, $\nabla_j \mathbf{e}_k = \Gamma_{jk}^i \mathbf{e}_i$. In the standard basis $\mathbf{e}_i = \frac{\partial h}{\partial x^i}$, the Christoffel symbols are related to the metric tensor by

$$\Gamma_{jk}^i = \frac{1}{2} g^{il} (\partial_j g_{kl} + \partial_k g_{jl} - \partial_l g_{jk}). \quad (2.2)$$

Acting on a general vector $v = v^i \mathbf{e}_i \in T_y M$, the covariant derivative be-

¹We are following the Ricci calculus throughout the whole thesis: Two repeated tensor indices, one upper and one lower, are summed over, e.g. $v_i w^i = \sum_i v_i w^i$.

comes:

$$\nabla_k v = (\partial_k v^i + \Gamma_{kj}^i v^j) \mathbf{e}_i, \quad (2.3)$$

where the product rule has been applied, using that the covariant derivative acts as a normal derivative on the scalar functions v^i . This can be extended straightforwardly to tensors of higher rank, for example to second-order tensors $T = T^{ij} \mathbf{e}_i \otimes \mathbf{e}_j \in T_y M \otimes T_y M$:

$$\nabla_k T = (\partial_k T^{ij} + \Gamma_{kl}^i T^{lj} + \Gamma_{kl}^j T^{il}) \mathbf{e}_i \otimes \mathbf{e}_j. \quad (2.4)$$

In the course of this thesis, the basis vectors \mathbf{e}_i are generally dropped, leaving the corresponding equations for the tensor coefficients only, as is typically done in the physical literature. Another important feature of the covariant derivative is its compatibility with the metric tensor, meaning that $\nabla_k g^{ij} = \nabla_k g_{ij} = 0$. This property allows us to commute the covariant derivative with the metric tensor ad libitum, which is particularly useful for the raising or lowering of tensor indices in derivative expressions.

The motion of a particle on a manifold can be described by a curve $\gamma(t)$, which parametrizes the position of the particle at time t . Free particles are moving on energy-conserving curves, meaning that their velocity vectors $v = \dot{\gamma}$ are transported parallelly along $\gamma(t)$. In mathematical terms, $\nabla_{\dot{\gamma}} \dot{\gamma} = 0$, which is called the *geodesic equation*, which in local coordinates, $\gamma(t) = \gamma^i(t) \mathbf{e}_i$, becomes

$$\ddot{\gamma}^i + \Gamma_{jk}^i \dot{\gamma}^j \dot{\gamma}^k = 0. \quad (2.5)$$

The geodesic equation can be interpreted as the generalization of Newton's law of inertia to curved spaces. The solutions to Eq. (2.5) are called *geodesic lines* or simply *geodesics*, representing the lines of constant kinetic energy on a manifold.

Manifolds can be arbitrarily curved in general, bringing along the need for a general measure for curvature, applicable to all Riemann manifolds. A quantity fulfilling this requirement is the *Riemann curvature tensor* R , which intuitively measures the curvature-induced change of a tangent vector

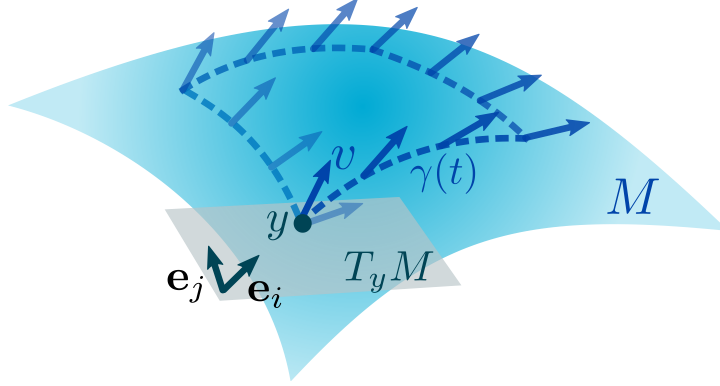


Figure 2.2: **Illustration of Riemann curvature.** A tangent vector $v \in T_y M$ at point y is parallelly transported around a closed curve $\gamma(t)$. In the presence of curvature, the final tangent vector deviates from the initial vector v , which – in the limit of an infinitesimal loop – is measured by the Riemann curvature tensor.

v when transported around a closed loop (see Figure 2.2). In the infinitesimal limit this change is quantified by

$$R(\mathbf{e}_i, \mathbf{e}_j) v = \nabla_i \nabla_j v - \nabla_j \nabla_i v,$$

which can also be interpreted as a measure of the noncommutativity of the covariant derivative. In a local coordinate basis $\{\mathbf{e}_i\}$, the coefficients of the Riemann curvature tensor are given by

$$R_{ijk}^l = g(R(\mathbf{e}_i, \mathbf{e}_j) \mathbf{e}_k, \mathbf{e}_l) = \partial_j \Gamma_{ik}^l - \partial_k \Gamma_{ij}^l + \Gamma_{jm}^l \Gamma_{ik}^m - \Gamma_{km}^l \Gamma_{ij}^m. \quad (2.6)$$

Important simplifications of the Riemann curvature tensor are obtained by tensor contraction, yielding the *Ricci tensor* $R_{ij} = R_{ikj}^k$ and the *Ricci scalar* $R = g^{ij} R_{ij}$.

Finally, it should be mentioned that all important differentiation operators appearing in fluid dynamics, such as the gradient, divergence, Laplacian

and vector Laplacian, can be generalized to curved space as follows:

$$\begin{aligned} (\text{grad } f)^i &= \nabla^i f = g^{ij} \partial_j f, \\ \text{div } v &= \nabla_i v^i = \frac{1}{\sqrt{g}} \partial_i (\sqrt{g} v^i), \\ \Delta_g f &= \text{div grad } f = \nabla_i \nabla^i f = \frac{1}{\sqrt{g}} \partial_i (\sqrt{g} g^{ij} \partial_j f), \\ \Delta_g v^k &= \nabla_i \nabla^i v^k = \frac{1}{\sqrt{g}} \partial_i (\sqrt{g} g^{ij} \nabla_j v^k), \end{aligned}$$

where \sqrt{g} denotes the square root of the determinant of the metric tensor. Regarding integration on manifolds, the integral of a function f over a curved volume V is defined by $\int_V Q dV$, where $dV = \sqrt{g} dx^1 \cdots dx^D =: \sqrt{g} d^D x$ denotes the volume form of a manifold.

2.2 Kinetic theory in curved space

In this section, we will shortly review the Boltzmann equation in curved space, being the fundamental equation underlying our model. The Boltzmann equation on a Riemann manifold, equipped with a stationary metric g , is defined as [56, 1]

$$\frac{\partial f}{\partial t} + v^i \frac{\partial f}{\partial x^i} - \Gamma_{jk}^i v^j v^k \frac{\partial f}{\partial v^i} + = \mathcal{C}[f], \quad (2.7)$$

where $f = f(x, v, t)$ denotes the particle distribution function, depending on the local coordinate $x = (x^1, \dots, x^D)$, on the microscopic velocity $v = (v^1, \dots, v^D)$ as well as on time t . The left-hand side of the Boltzmann equation represents free streaming along the geodesics of the manifold, whereas the right-hand side corresponds to particle collisions. Here, the forcing term $-\Gamma_{jk}^i v^j v^k \frac{\partial f}{\partial v^i}$ originates from the geodesic equation (2.5) and represents the inertial forces exerted on the particles. Collisions between particles are accounted for by the Boltzmann collision operator $\mathcal{C}[f]$, which we approximate by the simplified Bhatnagar-Gross-Krook (BGK) operator [57]

$$\mathcal{C}[f] = -\frac{1}{\tau} (f - f^{\text{eq}}),$$

where τ denotes the relaxation time and f^{eq} the Maxwell-Boltzmann equilibrium distribution on manifolds. The latter is given by [1]

$$f^{\text{eq}}(x, v, t) = \frac{\rho}{(2\pi\theta)^{D/2}} \exp\left(-\frac{\|v^i - u^i\|_g^2}{2\theta_T}\right), \quad (2.8)$$

where $\theta_T = k_B T/m$ denotes the normalized temperature, v^i is the microscopic velocity, and ρ and u^i denote the macroscopic density and velocity of the fluid. In the course of this thesis, we always work in the isothermal limit $\theta_T = 1$.

The macroscopic quantities, such as the density ρ , the velocity u^i and the energy-stress tensor T^{ij} of the fluid, are given by the moments of the distribution function,

$$\rho = \int f \sqrt{g} d^D v, \quad \rho u^i = \int f v^i \sqrt{g} d^D v, \quad T^{ij} = \int f v^i v^j \sqrt{g} d^D v, \quad (2.9)$$

where

$$T^{ij} = Pg^{ij} + \rho u^i u^j - \nu (\nabla^i(\rho u^j) + \nabla^j(\rho u^i) + g^{ij} \nabla_k(\rho u^k)).$$

The first term of the energy-stress tensor contains the hydrostatic pressure $P = \rho \theta_T$, the second term $\sim \rho u^2$ contributes to the convection of the flow, and the last term $\sim \nabla(\rho u)$ represents viscous stresses, where the parameter ν denotes the kinematic viscosity.

In order to describe fluids (instead of rarefied gases), it is assumed that the ratio of the molecular mean free path to the representative physical length scale (measured by the Knudsen number), is small. Under this assumption, the system satisfies the hydrodynamic conservation equations (Navier-Stokes equations), as can be shown rigorously by a Chapman-Enskog expansion [58, 59]. In covariant form, the Navier-Stokes equations read

$$\partial_t \rho + \nabla_i(\rho u^i) = 0, \quad \partial_t(\rho u^i) + \nabla_j T^{ij} = 0, \quad (2.10)$$

where the first equation ensures the conservation of mass (continuity equation), and the second equation incorporates the conservation of momentum (momentum equation). Here, ∇ denotes the covariant derivative, as defined in Eqs. (2.3) and (2.4), and T^{ij} the energy-stress tensor mentioned above.

2.3 Gauss-Hermite quadrature

In order to solve the Boltzmann equation numerically on a discrete lattice, the distribution function as well as the forcing term are expanded into a polynomial basis, consisting of the tensor Hermite polynomials, which are perfectly adapted to the Gaussian-shaped Maxwell-Boltzmann equilibrium distribution (2.8). Mathematically, the Hermite polynomials are defined by

$$\mathcal{H}_{(n)}^{i_1, \dots, i_n}(v) = (-1)^n w(v)^{-1} \frac{\partial}{\partial v_{i_1}} \cdots \frac{\partial}{\partial v_{i_n}} w(v),$$

where $w(v)$, the weight function, is given by

$$w(v) = \frac{1}{(2\pi)^{D/2}} \exp\left(-\frac{1}{2}\|v\|^2\right)^2,$$

and thus resembles the Maxwell-Boltzmann distribution in flat space. Explicitly, the first four Hermite polynomials read

$$\begin{aligned} \mathcal{H}_{(0)} &= 1, \\ \mathcal{H}_{(1)}^i &= v^i, \\ \mathcal{H}_{(2)}^{ij} &= v^i v^j - \delta^{ij}, \\ \mathcal{H}_{(3)}^{ijk} &= v^i v^j v^k - (\delta^{ij} v^k + \delta^{jk} v^i + \delta^{ki} v^j). \end{aligned}$$

The Hermite polynomials form a complete and orthogonal functional basis, satisfying the following orthogonality relation:

$$\int w(v) \mathcal{H}_{(n)}^{I_n}(v) \mathcal{H}_{(m)}^{J_m}(v) d^D v = \delta_{nm} \delta^{I_n J_n}, \quad n, m \in \mathbb{N}, \quad (2.11)$$

where $I_n = (i_1, \dots, i_n)$ and $J_m = (j_1, \dots, j_m)$ denote index tuple and $\delta^{I_n J_n} := \sum_{\sigma \in S_n} (\delta^{i_1 j_{\sigma(1)}} \cdots \delta^{i_n j_{\sigma(n)}})^3$.

Expanding the distribution function into Hermite polynomials yields the following expression:

$$f(x, v, t) = \frac{w(v)}{\sqrt{g}} \sum_{n=0}^{\infty} \frac{1}{n!} a_{(n)}^{i_1, \dots, i_n}(x, t) \mathcal{H}_{(n)}^{i_1, \dots, i_n}(v), \quad (2.12)$$

²Note that the weight functions are defined with respect to the Euclidean norm $\|v\| = \sqrt{\langle v, v \rangle}$ instead of the norm on manifolds $\|\cdot\|_g$.

³The sum runs over all index permutations in $J_n = (j_1, \dots, j_n)$, labeled by $\sigma \in S_n$, where S_n denotes the symmetric group.

2.3. GAUSS-HERMITE QUADRATURE

where $a_{(n)}$ are the coefficients of the expansion, which can be calculated from f as follows:

$$a_{(n)}^{i_1, \dots, i_n}(x, t) = \int f(x, v, t) \mathcal{H}_{(n)}^{i_1, \dots, i_n}(v) \sqrt{g} d^D v.$$

As can be seen by plugging in the explicit expressions of the first Hermite polynomials, the coefficients $a_{(n)}$ are directly related to the macroscopic moments of the distribution function (2.9).

A key feature of the LB method is the exact computation of the macroscopic moments (2.9) on the lattice by using Gauss-Hermite quadrature [44], meaning that velocity space integrals are essentially replaced by sums over a discrete set of velocity vectors without loss of accuracy. To this end, the underlying lattice must possess certain symmetries in order to satisfy the orthogonality relation (2.11) up to the order N of the quadrature, i.e.

$$\sum_{\lambda=1}^Q w_\lambda \mathcal{H}_{(n)}^{I_n}(v_\lambda) \mathcal{H}_{(m)}^{J_m}(v_\lambda) = \delta_{nm} \delta^{I_n J_n}, \quad 0 \leq n, m \leq N, \quad (2.13)$$

where $\{v_\lambda\}_{\lambda=1}^Q$ is a discrete set of velocity vectors, and $\{w_\lambda\}_{\lambda=1}^Q$ are the weights of the Gauss-Hermite quadrature. Eq. (2.13) defines a system of equations for the lattice vectors v_λ and weights w_λ . The solutions are commonly classified by the spatial dimension D and number of discrete velocities Q . Typically, the discrete velocities are rescaled by the lattice-dependent speed of sound c_s to obtain integer values for the lattice velocities, $c_\lambda = c_s v_\lambda$, pointing exactly from lattice point to lattice point. Examples are given by the two-dimensional $D2Q17$ (Table 2.1) lattice or the three-dimensional $D3Q41$ lattice (Table 2.2), both satisfying the orthogonality relations up to order $N = 3$. Eq. (2.13) can also be rewritten in terms of symmetry

relations,

$$\begin{aligned} \sum_{\lambda=1}^Q w_\lambda &= 1, \\ \sum_{\lambda=1}^Q w_\lambda c_\lambda^i c_\lambda^j &= c_s^2 \delta^{ij}, \\ \sum_{\lambda=1}^Q w_\lambda c_\lambda^i c_\lambda^j c_\lambda^k c_\lambda^l &= c_s^4 (\delta^{ij} \delta^{kl} + \delta^{ik} \delta^{jl} + \delta^{il} \delta^{jk}), \end{aligned} \quad (2.14)$$

which are satisfied up to the $(2N)$ -th power of c_λ , where sums over odd powers of c_λ vanish by isotropy.

λ	c_λ	w_λ
1	$(0, 0)$	$\frac{575+193\sqrt{193}}{8100}$
2-5	$(\pm 1, 0), (0, \pm 1)$	$\frac{3355-91\sqrt{193}}{18000}$
6-9	$(\pm 1, \pm 1)$	$\frac{655+17\sqrt{193}}{27000}$
10-13	$(\pm 2, \pm 2)$	$\frac{685-49\sqrt{193}}{54000}$
14-17	$(\pm 3, 0), (0, \pm 3)$	$\frac{1445-101\sqrt{193}}{162000}$

Table 2.1: *D2Q17 lattice vectors c_λ and weights w_λ .* For the *D2Q17* lattice, the speed of sound reads $c_s = \sqrt{\frac{5}{6} - \frac{\sqrt{193}}{30}}$.

2.4 The lattice Boltzmann equation in curved space

Given a suitable lattice with lattice vectors $\{c_\lambda\}$, we can finally formulate the LB equation on manifolds, as introduced by M. Mendoza *et al.* [1, 2]:

$$f_\lambda(x + c_\lambda \Delta t, t + \Delta t) - f_\lambda(x, t) = -\frac{1}{\tau} (f_\lambda - f_\lambda^{\text{eq}}) + \Delta t \mathcal{F}_\lambda. \quad (2.15)$$

This equation describes the evolution of the discrete distribution functions $\{f_\lambda(x, t)\}_{\lambda=1}^Q$ on the lattice, where λ labels the distribution function corresponding to the velocity vector c_λ . Here, τ denotes the relaxation time,

2.4. THE LATTICE BOLTZMANN EQUATION IN CURVED SPACE

λ	c_λ	w_λ
1	(0, 0, 0)	$\frac{2}{2025} (5045 - 1507\sqrt{10})$
2-7	$(\pm 1, 0, 0), (0, \pm 1, 0), (0, 0, \pm 1)$	$\frac{37}{5\sqrt{10}} - \frac{91}{40}$
8-19	$(\pm 1, \pm 1, 0), (\pm 1, 0, \pm 1), (0, \pm 1, \pm 1)$	$\frac{1}{50} (55 - 17\sqrt{10})$
20-27	$(\pm 1, \pm 1, \pm 1)$	$\frac{1}{1600} (233\sqrt{10} - 730)$
28-33	$(\pm 3, 0, 0), (0, \pm 3, 0), (0, 0, \pm 3)$	$\frac{1}{16200} (295 - 92\sqrt{10})$
34-41	$(\pm 3, \pm 3, \pm 3)$	$\frac{1}{129600} (130 - 41\sqrt{10})$

Table 2.2: **D3Q41 lattice vectors c_λ and weights w_λ .** For the D3Q41 lattice, the speed of sound reads $c_s = \sqrt{1 - \sqrt{\frac{2}{5}}}$.

f_λ^{eq} the equilibrium distribution and \mathcal{F}_λ the forcing term, representing the inertial forces on the manifold. Due to the specific shape of the streaming operator (left-hand side of Eq. 2.15)), the spacing of the lattice grid points is identical to the time step size Δt .

In order to solve the LB equation numerically, the equation is typically split into a collision step

$$f_\lambda^*(x, t) = -\frac{1}{\tau} (f_\lambda - f_\lambda^{\text{eq}}) + \Delta t \mathcal{F}_\lambda,$$

and a streaming step

$$f_\lambda(x, t + \Delta t) = f_\lambda^*(x - c_\lambda \Delta t, t),$$

where f^* denotes an auxiliary field. Figure 2.3 illustrates the streaming step on a two-dimensional D2Q17 lattice.

The equilibrium distribution f^{eq} , appearing in the collision step, is expanded into Hermite polynomials up to 3rd order, as explained in the previous section:

$$f_\lambda^{\text{eq}} = \frac{w_\lambda}{\sqrt{g}} \sum_{n=0}^3 \frac{1}{n! c_s^n} a_{(n)}^{\text{eq}, i_1, \dots, i_n} \mathcal{H}_{(n), \lambda}^{i_1, \dots, i_n}, \quad (2.16)$$

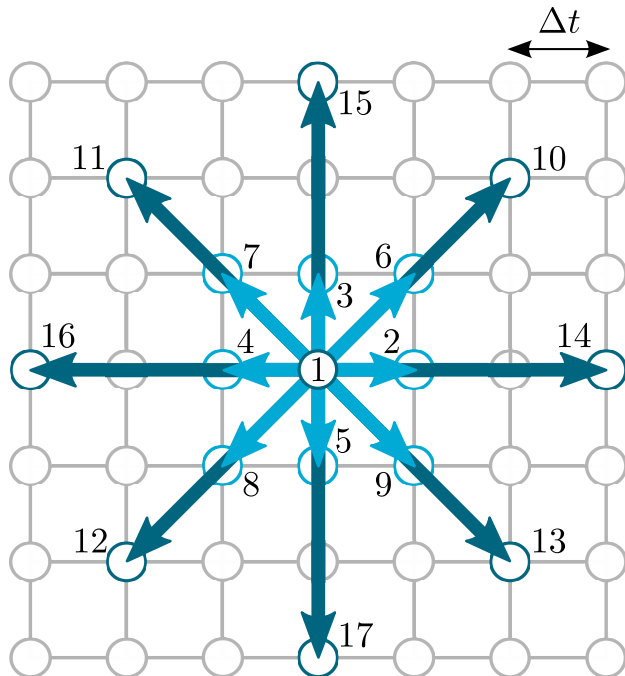


Figure 2.3: **Streaming on the $D2Q17$ lattice.** The $D2Q17$ lattice consists of 17 isotropically distributed velocity vectors c_λ , where the lattice spacing is given by Δt . Since this lattice is a higher-order lattice, the distribution functions stream not only to the nearest neighboring nodes (1 – 9), but also to higher-order neighbors (10 – 17) at each time step.

where we have defined $\mathcal{H}_{(n),\lambda} = \mathcal{H}_{(n)}(v_\lambda) = \mathcal{H}_{(n)}(c_\lambda/c_s)$. Due to the symmetry properties of the lattice (2.14) (based on the Gauss-Hermite quadrature), the moments of the Maxwell-Boltzmann equilibrium distribution are recovered exactly up to 3rd order, even for a discrete set of velocity vectors:

$$\rho = \int f^{\text{eq}} \sqrt{g} d^D v = \sum_{\lambda} f_{\lambda}^{\text{eq}} \sqrt{g}, \quad (2.17)$$

$$\rho u^i = \int f^{\text{eq}} v^i \sqrt{g} d^D v = \sum_{\lambda} f_{\lambda}^{\text{eq}} c_{\lambda}^i \sqrt{g}, \quad (2.18)$$

$$\begin{aligned} \Pi^{\text{eq},ij} {}^4 &= \int f^{\text{eq}} v^i v^j \sqrt{g} d^D v = \sum_{\lambda} f_{\lambda}^{\text{eq}} c_{\lambda}^i c_{\lambda}^j \sqrt{g} \\ &= \rho (c_s^2 g^{ij} + u^i u^j), \end{aligned} \quad (2.19)$$

$$\begin{aligned} \Sigma^{\text{eq},ijk} &= \int f^{\text{eq}} v^i v^j v^k \sqrt{g} d^D v = \sum_{\lambda} f_{\lambda}^{\text{eq}} c_{\lambda}^i c_{\lambda}^j c_{\lambda}^k \sqrt{g} \\ &= \rho c_s^2 (u^i g^{jk} + u^j g^{ik} + u^k g^{ij}) + \rho u^i u^j u^k. \end{aligned} \quad (2.20)$$

Correspondingly, the expansion coefficients of the equilibrium distribution in Eq. (2.16) are given by

$$a_{(0)}^{\text{eq}} = \rho, \quad a_{(1)}^{\text{eq},i} = \rho u^i, \quad a_{(2)}^{\text{eq},ij} = \rho c_s^2 \Delta^{ij} + \rho u^i u^j, \quad (2.21)$$

$$a_{(3)}^{\text{eq},ijk} = \rho c_s^2 (\Delta^{ij} u^k + \Delta^{jk} u^i + \Delta^{ki} u^j) + \rho u^i u^j u^k, \quad (2.22)$$

where $\Delta^{ij} := g^{ij} - \delta^{ij}$.

Regarding the forcing term \mathcal{F}_λ , there are many possible implementations, as presented in Section 2.5. Independently of the specific numerical implementation, the forcing term must possess the following set of macroscopic

⁴ $\Pi^{\text{eq},ij}$ denotes the equilibrium part of the energy-stress tensor $T^{ij} = \Pi^{\text{eq},ij} - \sigma^{ij}$. The non-equilibrium part is given by the viscous stress tensor $\sigma^{ij} = -\left(1 - \frac{1}{2\tau}\right) \Pi^{\text{neq},ij}$, where $\Pi^{\text{neq},ij} = \sum_{\lambda} (f_{\lambda} - f_{\lambda}^{\text{eq}}) c_{\lambda}^i c_{\lambda}^j \sqrt{g}$.

moments in order to converge to the covariant Navier-Stokes equation (2.10):

$$A = \sum_{\lambda} \mathcal{F}_{\lambda} \sqrt{g} = -\Gamma_{ij}^i \rho u^j - \Gamma_{ij}^j \rho u^i, \quad (2.23)$$

$$B^i = \sum_{\lambda} \mathcal{F}_{\lambda} c_{\lambda}^i \sqrt{g} = -\Gamma_{jk}^k T^{ij} - \Gamma_{jk}^i T^{jk} - \Gamma_{jk}^j T^{ki}, \quad (2.24)$$

$$C^{ij} = \sum_{\lambda} \mathcal{F}_{\lambda} c_{\lambda}^i c_{\lambda}^j \sqrt{g} = -\Gamma_{kl}^l \Sigma^{\text{eq},ijk} - \Gamma_{kl}^i \Sigma^{\text{eq},jkl} - \Gamma_{kl}^j \Sigma^{\text{eq},kli} - \Gamma_{kl}^k \Sigma^{\text{eq},lij}. \quad (2.25)$$

In the presence of an additional external force F_{ext} (e.g. gravity) the first moment receives an additional contribution: $B^i \rightarrow B^i + F_{\text{ext}}^i$. As for the continuum case, it can be rigorously shown that, in the hydrodynamic limit of small Knudsen numbers, the LB equation merges into the covariant Navier-Stokes equations (2.10), as shown in Appendix A.1. In the Navier-Stokes equations, the hydrostatic pressure is given by $P = \rho c_s^2$, where c_s denotes the lattice-specific speed of sound, and the kinematic viscosity ν is directly related to the LB relaxation time τ by the relation $\nu = (\tau - \frac{1}{2}) c_s^2 \Delta t$.

2.5 Forcing term implementations

The forcing term \mathcal{F}_{λ} in the LB equation (2.15) represents the inertial forces exerted on the fluid in curved space. There are many different ways to implement the forcing term, all of them satisfying the correct Navier-Stokes equations, but differing in accuracy and computational cost.

2.5.1 Third-order inertial forcing term

The first approach starts from the continuum Boltzmann equation (2.7), by plugging the expanded distribution function (2.12) into the analytical forcing term [2]:

$$-\Gamma_{jk}^i v^j v^k \frac{\partial f}{\partial v^i} = \frac{w(v)}{\sqrt{g}} \sum_{n=0}^{\infty} \frac{1}{n!} a_{(n)}^{i_1, \dots, i_n} \Gamma_{jk}^i v^j v^k \mathcal{H}_{(n+1)}^{i, i_1, \dots, i_n}(v). \quad (2.26)$$

The discrete forcing term is obtained by discretizing Eq. (2.27) on the lattice (replacing continuous velocities and weights by the corresponding

discrete ones) and truncating the expansion at third order in the Hermite polynomials:

$$\mathcal{F}_\lambda = -\frac{w_\lambda}{\sqrt{g}} \sum_{n=0}^2 \frac{1}{n! c_s^{(n+1)}} a_{(n)}^{i_1, \dots, i_n} F_\lambda^i \mathcal{H}_{(n+1), \lambda}^{i, i_1, \dots, i_n}, \quad (2.27)$$

where $F_\lambda^i = -\Gamma_{jk}^i c_\lambda^j c_\lambda^k$ are the inertial forces and external forces can be added by replacing $F_\lambda^i \rightarrow (F_\lambda^i + F_{\text{ext}}^i)$. As an improvement of the forcing term used in Ref. [2], not all of the expansion coefficients $a_{(n)}$ are approximated by the corresponding coefficients of the equilibrium distribution (2.21), but we set

$$a_{(0)} = a_{(0)}^{\text{eq}}, \quad a_{(1)}^i = a_{(1)}^{\text{eq}, i}, \quad a_{(2)}^{ij} = a_{(2)}^{\text{eq}, ij} - \sigma^{ij},$$

where $\sigma^{ij} = -(1 - \frac{1}{2\tau}) \sum_\lambda (f_\lambda - f_\lambda^{\text{eq}}) c_\lambda^i c_\lambda^j \sqrt{g}$ denotes the viscous stress tensor. In this way, the forcing term moments depicted in Eqs. (2.23-2.25) are exactly recovered, as required for the covariant Navier-Stokes equations, which are numerically satisfied at first order in the lattice spacing Δt .

2.5.2 Second-order inertial forcing term

An alternative implementation of the forcing term can be obtained by constructing a second-order Hermite expansion ab initio such that the moments of the forcing term are correctly recovered. To this end, we make the following ansatz:

$$\mathcal{F}_\lambda = \frac{w_\lambda}{\sqrt{g}} \sum_{n=0}^2 \frac{1}{n! c_s^n} b_{(n)}^{i_1, \dots, i_n} \mathcal{H}_{(n)}^{i_1, \dots, i_n}. \quad (2.28)$$

In order to match the correct moments, Eqs. (2.23-2.25), the expansion coefficients must be chosen as follows:

$$b_{(0)} = A, \quad b_{(1)}^i = B^i, \quad b_{(2)}^{ij} = C^{ij} - c_s^2 \delta^{ij} A,$$

where A , B^i and C^{ij} are the moments given by Eqs. (2.23-2.25).

The second-order forcing term recovers the Navier-Stokes equations at the same accuracy as the forcing term presented in the previous section, namely at first order in Δt . However, compared to the previous forcing

term, this implementation saves computational costs, since the order of the Hermite expansion is reduced by one. In this thesis, both forcing term implementations will be used.

In order to recover the Navier-Stokes equation at second order in Δt , a more involved forcing scheme is necessary, as presented in the following sections.

2.5.3 Cancelation of discrete lattice effects by moment corrections

As for standard LB schemes, the forcing term is known to generate spurious artifacts at first order in Δt [55]. These discrete lattice effects manifest themselves as spurious additional terms of order Δt in the Navier-Stokes equations:

$$\partial_t \rho + \nabla_i (\rho u^i) = -\frac{\Delta t}{2} (\partial_t A + (\partial_i - \Gamma_{ji}^j) B^i), \quad (2.29)$$

$$\partial_t (\rho u^i) + \nabla_j T^{ij} = -\frac{\Delta t}{2} \partial_t B^i, \quad (2.30)$$

where A and B^i are the moments of the forcing term, defined in Eqs. (2.23-2.24). The terms on the right-hand side of Eqs. (2.29) - (2.30) are error terms, which act as spurious source terms and should thus be canceled to achieve second-order accuracy. If the external force only depends on space and time (but not on the velocity), this can be done through a simple redefinition of the fluid velocity as suggested in Ref. [55]. In our case, however, the inertial forces, $F_\lambda^i = -\Gamma_{jk}^i c_\lambda^j c_\lambda^k$, also depend on the lattice velocities c_λ^i , which crucially affects the moments of the forcing term. Moreover, our forcing term contributes not only to the momentum equation, but also to the continuity equation, making it impossible to cancel all error terms by a redefinition of the velocity alone. Still, it is possible to eliminate all spurious terms of order Δt by correcting not only the velocity u but also the density ρ at each time step:

$$\rho \longrightarrow \hat{\rho} = \rho + \Delta t S(\hat{\rho}, \hat{u}), \quad (2.31)$$

$$\rho u^i \longrightarrow \hat{\rho} \hat{u}^i = \rho u^i + \Delta t U^i(\hat{\rho}, \hat{u}), \quad (2.32)$$

where $S(\hat{\rho}, \hat{u})$ and $U^i(\hat{\rho}, \hat{u})$ denote correction terms, given by

$$S(\hat{\rho}, \hat{u}) = -\frac{1}{2} (\Gamma_{ij}^i \hat{\rho} \hat{u}^j + \Gamma_{ji}^i \hat{\rho} \hat{u}^j),$$

$$U^i(\hat{\rho}, \hat{u}) = -\frac{1}{2} (\Gamma_{jk}^i \hat{\Pi}^{\text{eq},jk} + \Gamma_{jk}^j \hat{\Pi}^{\text{eq},ki} + \Gamma_{kj}^j \hat{\Pi}^{\text{eq},ki}),$$

where $\hat{\Pi}^{\text{eq},ij} = \hat{\rho} c_s^2 g^{ij} + \hat{\rho} \hat{u}^i \hat{u}^j$ is the free momentum-flux tensor, evaluated on the corrected density and velocity. The correction terms S and U^i correspond in form to the moments of the forcing term (2.23-2.24) and thus account for inertial effects on the fluid velocity and on the energy-stress tensor, originating from the covariant derivatives in the Navier-Stokes equations (2.10). Equations (2.31) and (2.32) define a system of coupled quadratic equations in $\hat{\rho}$ and \hat{u} , which can be solved numerically, by using for example Newton's algorithm, which converges to the solution rapidly after a few iterations (see Appendix A.1.1 for details). The equilibrium distribution, $f^{\text{eq}} = f^{\text{eq}}(\hat{\rho}, \hat{u})$, as well as the forcing term, $\mathcal{F} = \mathcal{F}(\hat{\rho}, \hat{u})$, are evaluated with the corrected density $\hat{\rho}$ and velocity \hat{u} at each time step. Additionally, the forcing term \mathcal{F}_λ in the LB equation (2.15) must be rescaled as follows:

$$\mathcal{F}_\lambda \longrightarrow (1 - \frac{1}{2\tau}) \mathcal{F}_\lambda. \quad (2.33)$$

As for the first moment of the forcing term B^i , the correction function U^i receives an additional contribution in the presence of an additional external force F^{ext} :

$$U^i(\hat{\rho}, \hat{u}) \longrightarrow U^i(\hat{\rho}, \hat{u}) + \frac{1}{2} \hat{\rho} F_{\text{ext}}^i.$$

With these corrections the Navier-Stokes equations are recovered at second order in space and time, as can be shown rigorously by a Chapman-Enskog expansion (see Appendix A.1.1 for the details). Thus, the accuracy of the method is significantly improved, as will be validated in Chapter 4.

2.5.4 Cancelation of discrete lattice effects by improved forcing term

Another way to cancel discrete lattice effects is to employ the trapezoidal rule for the time integration in the LB equation (2.15) by using an improved

forcing term, given by

$$\mathcal{F}_\lambda^*(x, t) := \mathcal{F}_\lambda(x, t) + \frac{1}{2} (\mathcal{F}_\lambda(x + c_\lambda \Delta t, t) - \mathcal{F}_\lambda(x, t - \Delta t)). \quad (2.34)$$

This forcing term can be implemented in an easy way by modifying the collision and streaming step of the LB algorithm as follows:

$$\begin{aligned} f_\lambda^*(x, t) &= -\frac{1}{\tau} (f_\lambda - f_\lambda^{\text{eq}}) + \Delta t \mathcal{F}_\lambda(x, t) - \frac{\Delta t}{2} \mathcal{F}_\lambda(x, t - \Delta t), \\ f_\lambda(x, t + \Delta t) &= f_\lambda^*(x - c_\lambda \Delta t, t) + \frac{\Delta t}{2} \mathcal{F}_\lambda(x, t). \end{aligned}$$

As for the forcing scheme presented in the previous subsection, the Navier-Stokes equations are recovered at second order in Δt , as shown in Appendix A.1.2. The advantage of this correction scheme, as compared to the previous scheme, is that the macroscopic moments (density ρ , velocity u etc.) are not modified and thus retain their original physical meaning. In the literature, the trapezoidal rule is commonly applied by a redefinition of the distribution function ($\bar{f}_\lambda = f_\lambda - \frac{1}{2}(\mathcal{C}[f_\lambda] + \Delta t \mathcal{F}_\lambda)$, cf. Ref. [60]). However, for the forcing term used in our model, this would again require a correction of the macroscopic moments (ρ and u), which we want to avoid.

2.5.5 Improved lattice derivatives

In the course of this work, we are often forced to compute derivatives of quantities defined on discrete lattice points. As an example, the computation of the Christoffel symbols, Eq. (2.2) requires the differentiation of the metric tensor. The same applies to the Riemann curvature tensor (2.6), consisting of a combination of Christoffel symbols and derivatives of them. Here, we present an improved way of calculating discrete derivatives on the lattice with up to fourth-order precision. To this end, we use the isotropic discrete differential operators proposed in Ref. [61], which employ the symmetry of the isotropic LB lattices to obtain second-order accuracy. For example, the

gradient and the Laplacian of a lattice function f is given by

$$\partial_i f(x) = \frac{1}{c_s^2 \Delta t} \sum_{\lambda} w_{\lambda} c_{\lambda}^i f(x + c_{\lambda} \Delta t) + \mathcal{O}(\Delta t^2) \quad (2.35)$$

$$\text{and } \Delta f(x) = \frac{2}{c_s^2 \Delta t^2} \sum_{\lambda} w_{\lambda} (f(x + c_{\lambda} \Delta t) - f(x)) + \mathcal{O}(\Delta t^2). \quad (2.36)$$

While in Ref. [61], the differential operators are computed at second-order precision in Δt , we can improve the discrete gradient operator $\partial_i f(x)$ to fourth-order accuracy by using the lattice symmetry relations given by Eq. (2.14). This yields:

$$\partial_i f(x) = \frac{1}{c_s^2 \Delta t} \sum_{\lambda} w_{\lambda} c_{\lambda}^i \left(f(x + c_{\lambda} \Delta t) - \frac{c_s^2 \Delta t^2}{2} (\Delta f)(x + c_{\lambda} \Delta t) \right) + \mathcal{O}(\Delta t^4), \quad (2.37)$$

where Δf denotes the Laplacian of f , which can be precomputed using Eq. (2.36) (for the full proof, see Appendix A.2).

By using the improved gradient operator (2.37), all differential geometrical objects such as the metric tensor, the Christoffel symbols and the Ricci curvature can be precomputed at high numerical precision $\mathcal{O}(\Delta t^4)$.

Chapter 3

Dean instability in double-curved channels

This chapter is reprinted with minor editing from *J.-D. Debus, M. Mendoza, H. J. Herrmann: “Dean instability in double-curved channels”, Phys. Rev. E 90, 053308 (2014)*, Ref. [62]. Copyright (2014) by the American Physical Society.

3.1 Introduction

It is well known that the properties of flows can be characterized by the Reynolds number, quantifying the relative importance of inertial forces and viscous forces in a fluid. At low Reynolds numbers, the flow through a curved duct is perfectly laminar, and its velocity profile resembles the parabolic profile of plane channel flow. Following Ref. [10], we refer to this type of flow as “curved channel Poiseuille flow”. For increasing Reynolds numbers, however, the flow pattern is more and more determined by centrifugal forces until it becomes unstable and bifurcates to secondary vortex flow. For the case of two concentric cylinders, as depicted in Figure 3.1, the bifurcation from laminar flow to vortex flow can be characterized by a dimensionless number, the Dean number $\mathcal{D}e$,

$$\mathcal{D}e := Re \cdot \sqrt{\frac{d}{\mathcal{R}}},$$

relating the geometry of the channel to the Reynolds number of the flow. Here, $d = r_o - r_i$ denotes the channel width, r_i and r_o the radii of the inner and outer cylinder, respectively, and \mathcal{R} the curvature radius of the inner wall (for a cylinder, $\mathcal{R} = r_i$). When the Dean number $\mathcal{D}e$ exceeds a critical value of $\mathcal{D}e_c \approx 36$, the flow becomes unstable with respect to small fluctuations, as shown analytically by William R. Dean [7] for narrow cylindrical channels with aspect ratio $\eta = r_i/r_o \approx 1$. At the bifurcation point, the flow transitions into Dean vortex flow, which is characterized by pairs of counter-rotating streamwise-oriented vortices.

While most of the studies in the literature deal with very idealized geometries, for example rectangular channels [8, 9, 10, 11, 12], we study the Dean instability in double-curved channels, possessing both a streamwise and a cross-sectional curvature, as depicted in Figure 3.2.

Firstly, we vary the streamwise curvature radius \mathcal{R}_θ while keeping the cross-sectional curvature radius \mathcal{R}_ϕ fixed (see Figure 3.2), finding that the lowest Dean number at which the Dean instability occurs corresponds to the configuration in which both curvature radii are approximately equal. For channels with both weaker or stronger streamwise curvature, we measure an (almost linear) increase of the critical Dean number with \mathcal{R}_θ . For strongly-curved channels, we even observe a second bifurcation to vortex flow with 4 counter-rotating vortices.

Secondly, we vary the cross-sectional curvature radius \mathcal{R}_ϕ while keeping the streamwise curvature fixed. Again, we find a minimum of the critical Dean number for the case $\mathcal{R}_\theta \approx \mathcal{R}_\phi$, in consistence with our previous results. For increasing \mathcal{R}_ϕ , the curvature perpendicular to the streamwise direction becomes smaller and smaller, such that the double-curved channel approaches a cylindrical geometry in the limit $\mathcal{R}_\phi \rightarrow \infty$. Correspondingly, for increasing \mathcal{R}_ϕ , the critical Dean number for the double-curved channel approaches the corresponding value for cylindrical channels, given by $\mathcal{D}e_c \approx 36$.

For the flow simulations performed in this chapter, we use the LB method on manifolds with the improved third-order forcing term described in Section

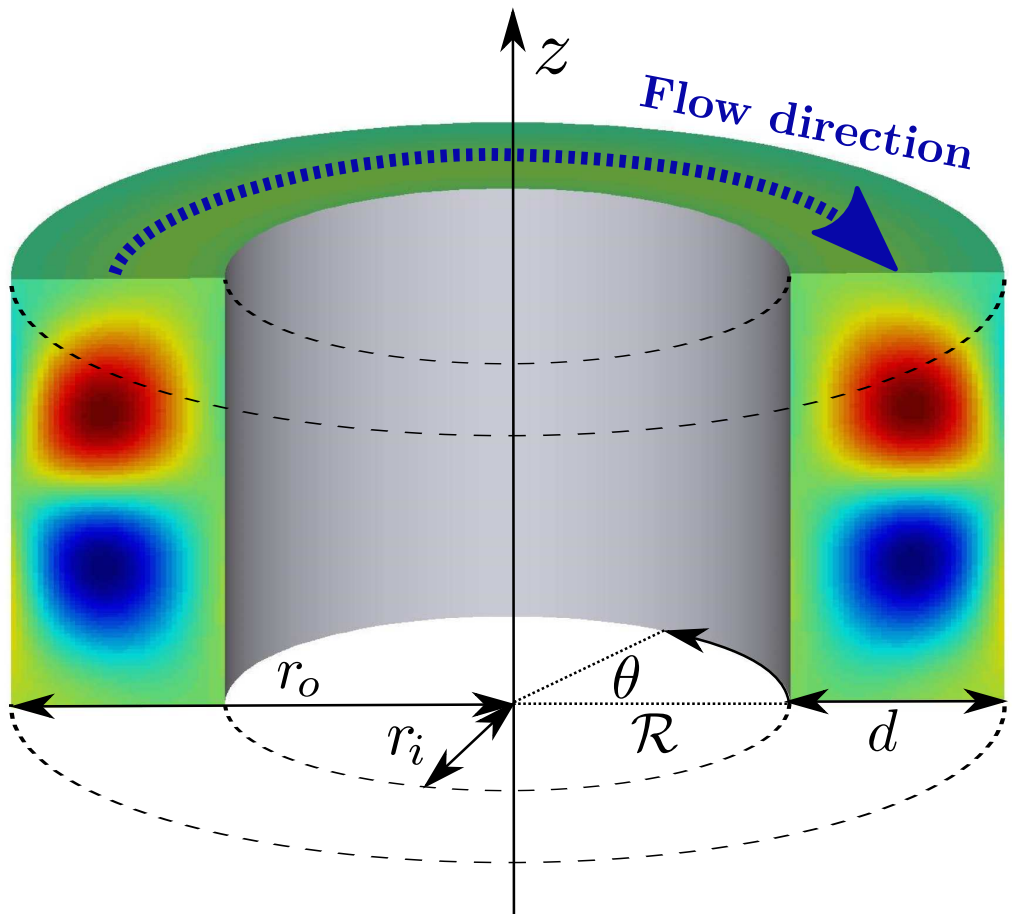


Figure 3.1: **Geometry of the cylindrical channel.** The colored cross-sections depict the counter-rotating vortex tubes, oriented in clockwise (blue) or counterclockwise direction (red) around the z -axis. The dashed lines indicate the periodicity of the channel in θ -direction.

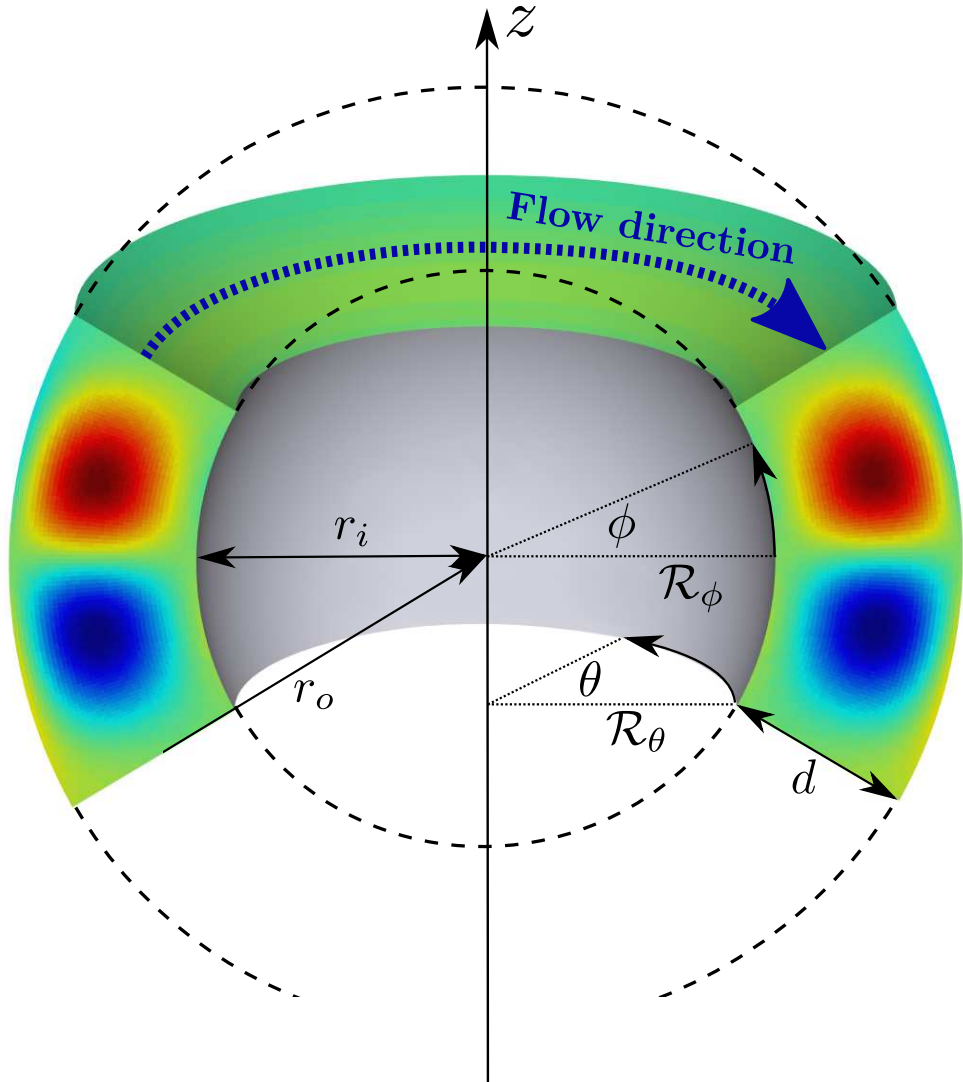


Figure 3.2: **Geometry of the double-curved channel.** The colored spots on the channel cross-sections at the inlet and outlet illustrate the pair of counter-rotating vortex tubes, oriented in clockwise (blue) or counterclockwise direction (red) around the z -axis. The dashed lines indicate the periodicity of the channel in ϕ -direction.

3.1. INTRODUCTION

2.5.1. We first validate the computational method by measuring the critical Dean number at the transition from laminar to vortex flow for a curved rectangular channel, obtaining very good agreement with the literature values by Finlay *et al.*, Ref. [12]. Furthermore, we compare our improved forcing term scheme presented in Section 2.5.1 to the original method introduced in Ref. [1] and show that the accuracy of the simulation results is considerably increased.

Since the LB method on manifolds can handle almost arbitrary, smooth geometries, we model curved channels by using generalized, curvilinear coordinates, which are perfectly adapted to the channel boundaries. Note that although the corresponding metric tensor differs from the Cartesian metric tensor, curvilinear coordinates do not give rise to a physical curvature of space (measured by the Riemann curvature tensor (2.6)), since the space is not intrinsically curved. Instead, curvilinear coordinates provide an alternative parametrizing of flat Euclidean space, while the flow “feels” the curvature of the channel only through the interaction with the curved walls, modeled by no-slip boundary conditions. The usage of generalized coordinates simplifies the implementation of the boundary conditions considerably, since the coordinates are precisely adjusted to the deformed channel walls. This offers a high flexibility with respect to complex curved boundary shapes, which in curvilinear coordinates can be described exactly by a uniform cubic lattice. As a consequence, to resolve the boundary shape to a given precision, the LB method on manifolds typically requires a lower grid resolution as compared to conventional techniques (such as immersed boundary techniques), which increases the computational efficiency. In particular, complicated and time-consuming approximation schemes of the curved walls (such as staircase approximations or interpolation schemes) can be avoided, which is one of the great advantages of the LB method on manifolds over existing methods operating in Cartesian coordinates. In addition, as demonstrated in the following section, three-dimensional solutions with rotational symmetries (e.g. flow between two rotating cylinders) can effectively be simulated by the LB method in two dimensions, which reduces the computational ef-

fort considerably. While in the literature, curvilinear coordinates are often implemented ab initio by deriving the Boltzmann equation explicitly in the specific coordinate system (as done for example for axisymmetric flow in polar coordinates [46]), the LB method on manifolds automatically attunes to the desired coordinate system, once the corresponding metric tensor is specified.

3.2 Validation: Flows through cylindrical channels

At first, we validate our model for the case of a cylindrical channel, for which we measure the dependence of the critical Dean number on the channel aspect ratio $\eta = r_i/r_o$. To this end, we consider the idealized case of flow in a closed cylindrical channel, as depicted in Figure 3.1. In an experimental application, the channel would not be completely closed, but would have a finite opening angle $< 2\pi$ with open boundaries at the inlet and outlet. However, for long and narrow channels, as considered in this study, the ratio between the streamwise extent and the spanwise extent d (being relevant for the instability) is very small ($\sim 10^{-2}$) such that possible finite-size effects at the inlet/outlet can be neglected. To drive the fluid, a pressure gradient between the inlet and outlet of a channel can be applied. In our simulations, we use a constant external force instead, which for nearly incompressible flow is equivalent to a pressure gradient.

Depending on the aspect ratio of the channel as well as on the Reynolds number Re , the primary Poiseuille flow transitions to secondary flow (Dean flow) at a specific critical value of the Dean number,

$$\mathcal{D}e := Re \cdot \sqrt{\frac{d}{\mathcal{R}}} = \frac{\langle v_\theta \rangle d}{\nu} \cdot \sqrt{\frac{d}{\mathcal{R}}}, \quad (3.1)$$

where $\langle v_\theta \rangle$ denotes the mean azimuthal fluid velocity, $\nu = (\tau - \frac{1}{2}) c_s^2 \Delta t$ the kinematic viscosity, $d = r_o - r_i$ the channel width, r_i and r_o the inner and outer radius, respectively, and \mathcal{R} the curvature radius of the inner wall (for a cylinder: $\mathcal{R} = r_i$). The transition to secondary vortex flow is caused by

centrifugal instabilities and is characterized by a pair of counter-rotating vortex tubes which are oriented along the stream direction. Using the LB method as described in Section 2.4, we model axisymmetric fluid flow for different channel aspect ratios $\eta = r_i/r_o$.

3.2.1 Geometry and simulation setup

In our model, the cylindrical channel is described by cylindrical coordinates $(x^1, x^2, x^3) = (r, \theta, z)$, which are perfectly adapted to the geometry of the system, thus avoiding imprecise staircase approximations of the channel boundaries. The corresponding coordinate chart is given by

$$h(r, \theta, z) = \begin{pmatrix} r \cos \theta \\ r \sin \theta \\ z \end{pmatrix},$$

inducing the standard basis $(\mathbf{e}_r, \mathbf{e}_\theta, \mathbf{e}_z) = (\frac{\partial h}{\partial r}, \frac{\partial h}{\partial \theta}, \frac{\partial h}{\partial z})$, in which all vectorial and tensorial quantities will be expressed. The corresponding metric tensor is given by

$$g_{ij} = \left\langle \frac{\partial h}{\partial x^i}, \frac{\partial h}{\partial x^j} \right\rangle = \begin{pmatrix} 1 & 0 & 0 \\ 0 & r^2 & 0 \\ 0 & 0 & 1 \end{pmatrix},$$

and the Christoffel symbols, Eq. (2.2), read

$$\Gamma_{ij}^r = \begin{pmatrix} 0 & 0 & 0 \\ 0 & -r & 0 \\ 0 & 0 & 0 \end{pmatrix}, \quad \Gamma_{ij}^\theta = \begin{pmatrix} 0 & \frac{1}{r} & 0 \\ \frac{1}{r} & 0 & 0 \\ 0 & 0 & 0 \end{pmatrix}, \quad \Gamma_{ij}^z = \begin{pmatrix} 0 & 0 & 0 \\ 0 & 0 & 0 \\ 0 & 0 & 0 \end{pmatrix}.$$

Since the cylindrical channel is rotational invariant in θ , we impose periodic boundaries in θ , which effectively reduces the three-dimensional problem to a two-dimensional one. Thus, each velocity component depends only on the spanwise dimensions r and z , explaining the name “two-dimensional” vortex solutions (as they are called in Ref. [63]).

For our simulations, we use a D3Q41 lattice (Table 2.2) of size $L_r \times L_\theta \times L_z = 128 \times 1 \times 256$, where each lattice node is labeled by integer lattice

indices $(\hat{r}, \hat{\theta}, \hat{z}) \in [1, L_r] \times [1, L_\theta] \times [1, L_z]$. The transformation between lattice units and physical units is given by

$$r = r_i + \hat{r} \cdot \Delta r, \quad \theta = \hat{\theta} \cdot \Delta\theta, \quad z = \hat{z} \cdot \Delta z,$$

where Δr , $\Delta\theta$ and Δz denote the lattice spacings in the radial, azimuthal and axial direction respectively. In our simulations, we set $\Delta r = \Delta\theta = \Delta z = \Delta t$ and $r_i = 1$. Thus, for a given aspect ratio $\eta = r_i/r_o$, the corresponding lattice spacing is given by $\Delta r = (1 - \eta)/(\eta L_r)$. In order to compare our results to the work by Finlay et al. [12], we only vary the radial aspect ratio $\eta = r_i/r_o$, keeping the spanwise aspect ratio fixed, $L_z/L_r = 2$. At the two channel walls at $r = r_i$ and $r = r_o$, we impose Dirichlet boundary conditions on the fluid velocity, $u(r_o) = u(r_i) = 0$. This condition enters the algorithm through the equilibrium distribution f^{eq} , which is evaluated with $u = 0$ at $r = r_i$ and $r = r_o$ at each time step. In the θ - and z -directions, we use periodic boundary conditions. We note that by considering periodicity in z , a symmetry condition is imposed on the solution, since the spanwise wave length of the Dean vortices is restricted to the values $\lambda = 2L_z/k$ (where k denotes the number of vortex cells). However, the choice $L_z/L_r = 2$ is motivated by the fact that the channel cross-section is perfectly adapted to the 2-cell vortex solution, since in this case the Dean cells can occupy the total cross-section.

The LB relaxation parameter τ is used to tune the Reynolds number (and thus the Dean number) to the parameter range of interest, where the bifurcation occurs. For the simulations, we choose a $\tau = 0.9$, which also enhances fast convergence to the stationary state.

3.2.2 Simulation results for cylindrical channels

In order to study the bifurcation from curved channel Poiseuille flow to secondary Dean flow, we vary the Dean number $\mathcal{D}e$ by varying the strength of the driving force. At the critical Dean number $\mathcal{D}e_c$, we expect the formation of counter-rotating vortex tubes, which should increase in strength for higher values of $\mathcal{D}e$. This can be measured by calculating the vorticity of the

3.2. VALIDATION: FLOWS THROUGH CYLINDRICAL CHANNELS

flow, given by $\omega = \nabla \times u$. (Note that some authors use the helicity, $H = u \times \omega$, instead, to analyze the Dean vortices. However, for the streamwise oriented vortices considered in this study, both quantities are equivalent, since the vorticity is fully characterized by its streamwise component, ω^θ). In particular, we are interested in the mean absolute vorticity, averaged over the whole cross-section of the channel,

$$\langle \omega^\theta \rangle = \frac{1}{S} \int_S \left| \frac{\partial u^r}{\partial z} - \frac{\partial u^z}{\partial r} \right| r dr dz,$$

where $S = \int dr dz$ denotes the cross-sectional area. At the critical Dean number $\mathcal{D}e_c$, the vorticity is expected to increase considerably. Indeed, this behavior has been observed in the simulations.

Exemplarily, Figure 3.3 shows the average vorticity $\langle \omega^\theta \rangle$ depending on the Dean number $\mathcal{D}e$ for a channel with aspect ratio $\eta = 0.80$. The curve agrees with the expectations, showing a clear transition from zero-vorticity Poiseuille flow for $\mathcal{D}e < 42$ to vortex flow for $\mathcal{D}e > 42$. The behavior of the vorticity at $\mathcal{D}e_c \approx 42$ is indicative of an imperfect bifurcation, as can be seen in the recent work by Haines *et. al* in Ref. [64]. At $\mathcal{D}e_c$, two counter-rotating vortex tubes form, which increase in strength for higher Dean numbers. The colored pictures in Figure 3.3 illustrate the velocity streamlines on a cross-section of the channel perpendicular to the stream direction at different Dean numbers. The colors represent the strength of the streamwise vorticity ω^θ , where blue and red colors correspond to clockwise and counterclockwise rotating vortices, respectively. Figure 3.3 also reveals a second bifurcation, which is indicated by a further increase of the vorticity at $\mathcal{D}e_{c2} \approx 54$, where a second pair of vortex tubes begins to form. Figure 3.4 shows the radial, streamwise and axial velocity profiles versus the z -position for the 4-cell vortex flow for $\eta = 0.80$ and $\mathcal{D}e = 56$.

We have measured the critical Dean number at the bifurcation from Poiseuille flow to 2-cell vortex flow for different channel aspect ratios $\eta = r_i/r_o$. The results are shown in Figure 3.5, which depicts the dependence of the critical Dean number on the aspect ratio of the channel. The errorbars result from the uncertainty in determining the critical Dean number from

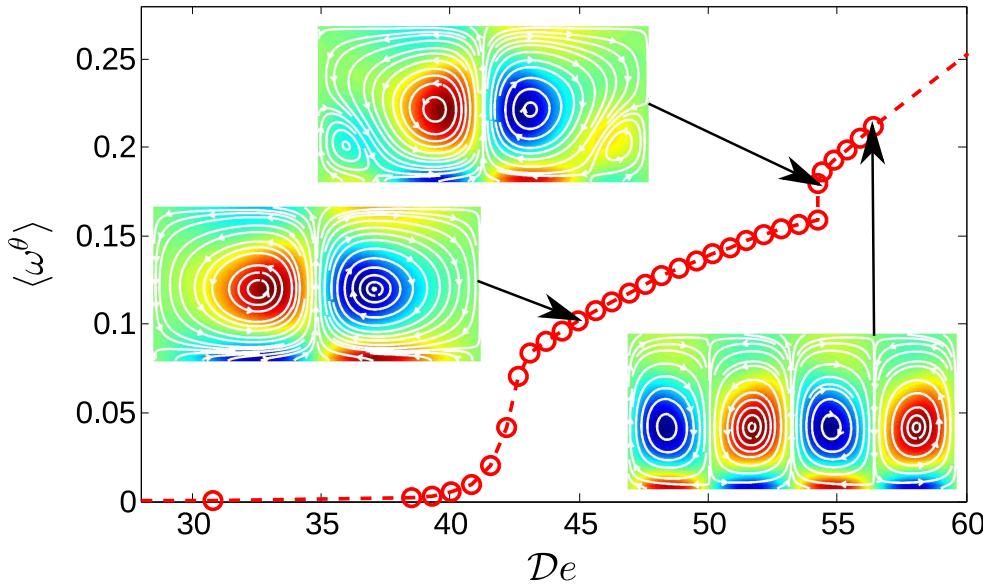


Figure 3.3: **Vorticity vs. Dean number for a cylindrical channel.** The curve depicts the average vorticity $\langle \omega^\theta \rangle$ as function of the Dean number $\mathcal{D}e$ for a cylindrical channel with aspect ratio $\eta = r_i/r_o = 0.80$. As can be seen, the bifurcation from Poiseuille flow to 2-cell vortex flow occurs at $\mathcal{D}e_c \approx 42$, followed by a second bifurcation to 4 vortices at $\mathcal{D}e_{c2} \approx 54$. The colored pictures depict the velocity streamlines on a channel cross-section perpendicular to the stream direction. The colors represent the strength of the vorticity, where blue and red colors correspond to clockwise and counterclockwise rotating vortices, respectively.

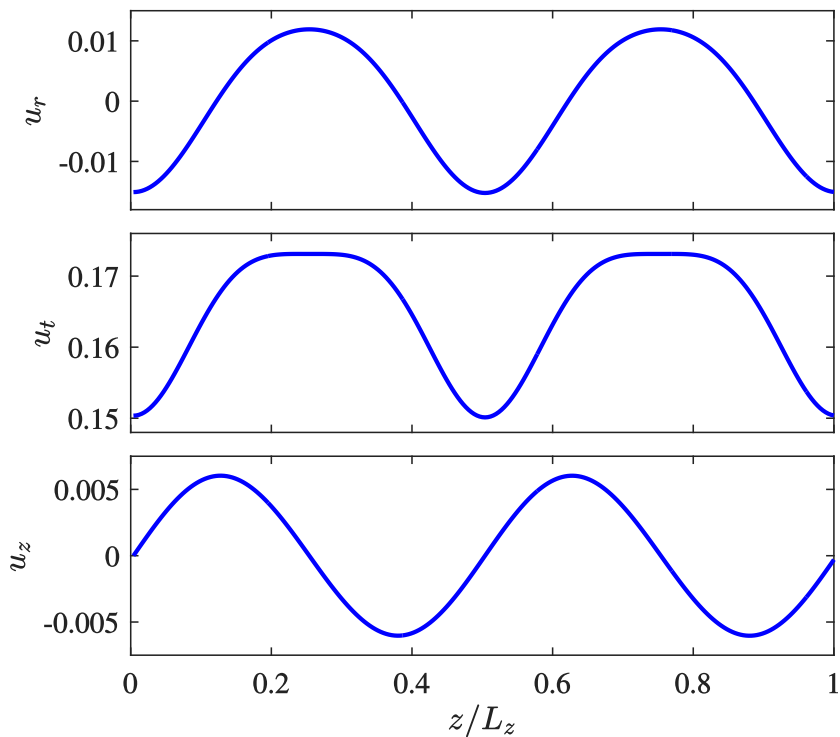


Figure 3.4: **Velocity profiles of vortex flow in a cylindrical channel.** The three curves correspond to the radial, streamwise and axial velocity profiles, respectively, for 4-cell vortex flow in a cylindrical channel with aspect ratio $\eta = 0.80$ at Dean number $\mathcal{D}e = 56$.

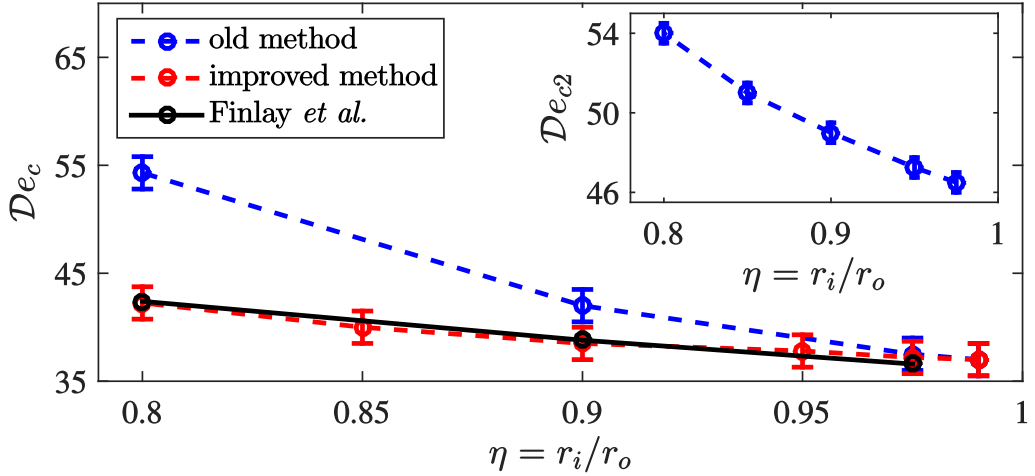


Figure 3.5: **Critical Dean numbers vs. aspect ratio of a cylindrical channel.** The critical Dean number $\mathcal{D}e_c$ is measured at the first bifurcation point from Poiseuille flow to 2-cell vortex flow. As can be seen, the results obtained by our improved method agree very well with the literature values of Finlay *et al.* Inset: Second critical Dean number $\mathcal{D}e_{c2}$ at the second bifurcation point from 2-cell vortex flow to 4-cell vortex flow as function of the aspect ratio $\eta = r_i/r_o$.

the vorticity curve, since the vorticity increases smoothly at the bifurcation point (as can be seen in Figure 3.3). We have also compared the present improved version of our method with the old version used in a previous publication [1], where the moments of the distribution function f in the forcing term have been approximated by the moments of the equilibrium distribution function f^{eq} . Comparing both methods to the numerical results by Finlay *et al.* [12] in Figure 3.5, we observe that the present improved method agrees very well with the literature, whereas our old method leads to deviations from the literature values. It can be seen that the deviations between the old method and the improved method vanish for $\eta \rightarrow 1$. This means that the error in the approximation of the forcing term in the old method becomes negligible when the resolution is sufficiently high.

We have also plotted the second critical Dean number $\mathcal{D}e_{c2}$, at which the second bifurcation from 2-cell vortex flow to 4-cell vortex flow occurs. The dependence on the aspect ratio η is shown in the inset of Figure 3.5. As

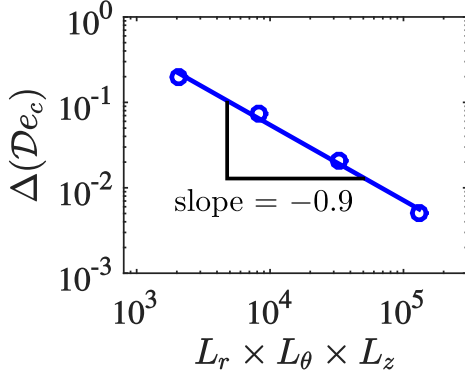


Figure 3.6: **Error of the critical Dean number vs. grid resolution.** The data points depict the relative error of the critical Dean number, denoted by $\Delta(\mathcal{D}e_c)$, as function of the number of grid points $N = L_r \times L_\theta \times L_z$ in log-log-scale for a cylindrical channel with aspect ratio $\eta = r_i/r_o = 0.9$. As can be seen, the error decreases with a power law exponent -0.9 as the resolution is increased.

can be seen, $\mathcal{D}e_{c2}$ decreases monotonically with the aspect ratio. For very narrow channels with aspect ratio $\eta > 0.95$, the second bifurcation occurs already at relatively low Dean numbers between 45 and 50.

3.2.3 Dependence on the grid resolution

To obtain an estimation of the resolution error in our simulations, we have measured the relative error of the critical Dean number for different resolutions. The relative error is defined as the relative deviation of the critical Dean number $\mathcal{D}e_c$ from the corresponding reference value $\mathcal{D}e_c^{\text{ref}}$, given by Finlay *et al.* in Ref. [12],

$$\Delta(\mathcal{D}e_c) := \frac{|\mathcal{D}e_c - \mathcal{D}e_c^{\text{ref}}|}{\mathcal{D}e_c^{\text{ref}}}.$$

Figure 3.6 depicts the dependence of the relative error on the grid resolution for a cylindrical channel with aspect ratio $\eta = r_i/r_o = 0.9$. As one can see, the relative error decreases rapidly when the grid resolution is increased. This shows that, within an error of 1%, our numerical results correspond to the physical values and are not affected by finite resolution effects.

3.3 Flows through double-curved channels

Taking advantage of the easy implementation of arbitrary metrics within our model, we now study the fluid flow through a double-curved channel, using ellipsoidal coordinates. Accordingly, the rectangular channel cross-section is bent (see Figure 3.2), which introduces a second, perpendicular curvature in the channel.

3.3.1 Geometry and simulation setup

The geometry of the double-curved channel follows from the cylindrical configuration by introducing a second curvature along the z -axis, which leads to a geometry that can best be described in terms of ellipsoidal coordinates $(x^1, x^2, x^3) = (r, \theta, \phi)$, defined by the chart

$$h(r, \theta, \phi) = \begin{pmatrix} r a \cos \theta \cos \phi \\ r b \sin \theta \cos \phi \\ r c \sin \phi \end{pmatrix},$$

where a, b, c are the lengths of the three semi-principle axes of the ellipsoid. All vector fields and tensors are expressed in terms of the standard basis $(\mathbf{e}_r, \mathbf{e}_\theta, \mathbf{e}_\phi) = (\frac{\partial h}{\partial r}, \frac{\partial h}{\partial \theta}, \frac{\partial h}{\partial \phi})$, which yields the metric tensor

$$g_{ij} = \begin{pmatrix} s_\phi^2 + c_\phi^2 (c_\theta^2 + b^2 s_\theta^2) & r (b^2 - 1) c_\phi^2 c_\theta s_\theta & r (1 - b^2) s_\theta^2 c_\phi s_\phi \\ r (b^2 - 1) c_\phi^2 c_\theta s_\theta & r^2 c_\phi^2 (s_\theta^2 + b^2 c_\theta^2) & r^2 (1 - b^2) c_\phi s_\phi c_\theta s_\theta \\ r (1 - b^2) s_\theta^2 c_\phi s_\phi & r^2 (1 - b^2) c_\phi s_\phi c_\theta s_\theta & r^2 (c_\phi^2 + s_\phi^2 (c_\theta^2 + b^2 s_\theta^2)) \end{pmatrix},$$

where we abbreviate $\sin x$ and $\cos x$ by s_x and c_x , respectively. The corresponding Christoffel symbols are given by

$$\Gamma_{ij}^r = \begin{pmatrix} 0 & 0 & 0 \\ 0 & -r c_\phi^2 & 0 \\ 0 & 0 & -r \end{pmatrix}, \quad \Gamma_{ij}^\theta = \begin{pmatrix} 0 & \frac{1}{r} & 0 \\ \frac{1}{r} & 0 & -\frac{s_\phi}{c_\phi} \\ 0 & -\frac{s_\phi}{c_\phi} & 0 \end{pmatrix}, \quad \Gamma_{ij}^\phi = \begin{pmatrix} 0 & 0 & \frac{1}{r} \\ 0 & s_\phi c_\phi & 0 \\ \frac{1}{r} & 0 & 0 \end{pmatrix}.$$

Since finite-size effects in channels of finite height are known to have a strong influence on the Dean instability (as studied in Ref. [12] for the case

3.3. FLOWS THROUGH DOUBLE-CURVED CHANNELS

of two concentric cylinders), we impose periodicity along the ϕ -direction by choosing $a = c = 1$. This corresponds to the periodicity in z -direction for the cylindrical case and avoids finite-height complications.

In the simulations, we use a uniform grid of size $L_r \times L_\theta \times L_\phi = 64 \times 64 \times 128$, for which the lattice indices $(\hat{r}, \hat{\theta}, \hat{\phi}) \in [1, L_r] \times [1, L_\theta] \times [1, L_\phi]$ are related to the physical units by

$$r = r_i + \hat{r} \cdot \Delta r, \quad \theta = \left(\hat{\theta} - \frac{L_\theta}{2} \right) \Delta \theta, \quad \phi = \left(\hat{\phi} - \frac{L_\phi}{2} \right) \Delta \phi.$$

As for the cylindrical channel, we choose $\Delta r = \Delta \theta = \Delta \phi = \Delta t = (1 - \eta)/(\eta L_r)$, where $\eta = r_i/r_o$ denotes the aspect ratio of the channel.

The inner and outer walls of the channel at $r = r_i$ and $r = r_o$ are implemented in the same way as for the cylindrical case by using Dirichlet boundary conditions for the fluid velocity, $u(r_o) = u(r_i) = 0$. We further use open boundary conditions in θ -direction as well as periodic boundaries in ϕ . Since by construction the channel is periodic in ϕ , we can restrict the simulation domain to a circular sector in ϕ (as indicated by the dotted lines in Figure 3.2). Note that by restricting to a finite sector and considering periodic boundary conditions, a symmetry condition is imposed on the solution, which might exclude some phases in the bifurcation diagram. However, since this is also the case for the cylindrical channel to which we want to compare, we do not take those phases into account. In particular, the double-curved channel is constructed in such a way that it approaches the geometry of the cylindrical channel (Figure 3.1) for increasing inner radii r_i . The open channel boundaries at $\theta = \pm \frac{L_\theta}{2} \Delta \theta$ define an inlet and an outlet for the flow, as can be seen in Figure 3.2. In order to drive the fluid through the channel, an external force in θ -direction can be applied, which for incompressible flow is physically equivalent to a pressure gradient between the inlet and the outlet.

3.3.2 Simulation results for double-curved channels

We study the bifurcation from curved channel Poiseuille flow to Dean vortex flow by varying the Dean number,

$$\mathcal{D}e = \frac{\langle v_\theta \rangle d}{\nu} \cdot \sqrt{\frac{d}{\mathcal{R}_\theta}}, \quad (3.2)$$

where $d = r_o - r_i$ and $\nu = (\tau - 1/2) c_s^2 \Delta t$. \mathcal{R}_θ denotes the streamwise curvature radius of the inner wall, given by $\mathcal{R}_\theta = r_i b^2$ at $\theta = 0$. The mean azimuthal velocity $\langle v_\theta \rangle$ is calculated as follows,

$$\langle v_\theta \rangle = \frac{1}{S} \int_S u^\theta r^2 b \cos \phi dr d\phi,$$

where $S = \int r dr d\phi$ is the cross-sectional area of the channel and u^θ is the azimuthal component of the velocity field $u = u^r \mathbf{e}_r + u^\theta \mathbf{e}_\theta + u^\phi \mathbf{e}_\phi$. Like in the cylindrical case, we measure the average vorticity in the streamwise direction at $\theta = 0$, given by

$$\langle \omega^\theta \rangle = \frac{1}{S} \int_S \left| \frac{\partial u^r}{\partial \phi} - \frac{\partial u^\phi}{\partial r} \right| r b \cos \phi dr d\phi.$$

We study two different cases: In the first case, we vary the streamwise curvature radius of the channel $\mathcal{R}_\theta = r_i b^2$ by changing the length of the semi-principal axes b while the inner radius r_i is kept fixed. In the second case, we study the effect of the cross-sectional curvature radius $\mathcal{R}_\phi = r_i$ along the ϕ direction by varying the inner radius r_i while keeping the streamwise curvature radius \mathcal{R}_θ fixed.

3.3.2.1 Variation of streamwise curvature

First, we vary the curvature radius along the flow direction, $\mathcal{R}_\theta = r_i b^2$, by varying b at fixed cross-sectional curvature radius $\mathcal{R}_\phi = r_i = 1$. For the channel, we choose an aspect ratio of $\eta = r_i/r_o = 0.9$. For all the simulations of the double-curved channel, we set the relaxation time τ to 1 in order to work in the desired parameter range of the Reynolds number (and Dean number), keeping at the same time a good computational performance. The

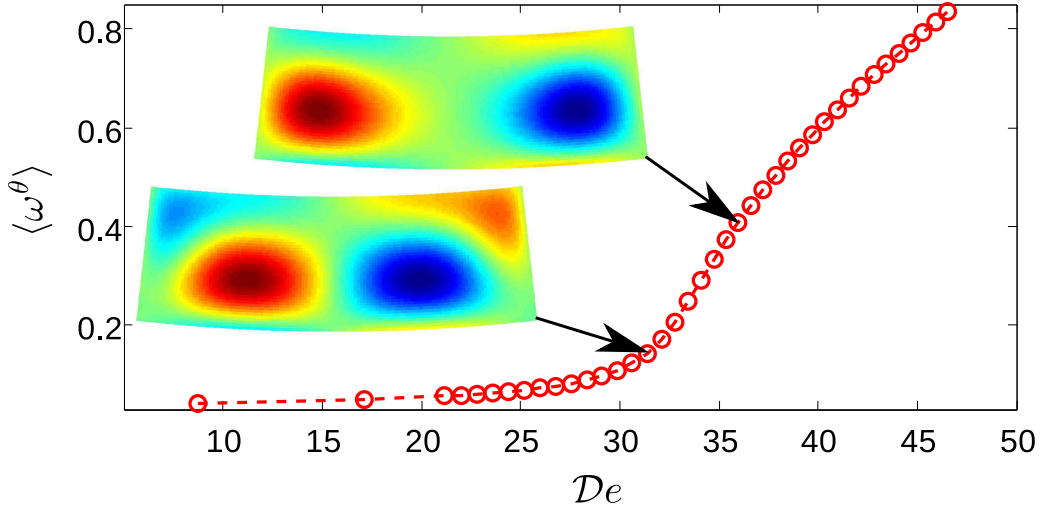


Figure 3.7: **Vorticity vs. Dean number for a double-curved channel.** The curve depicts the average vorticity $\langle \omega^\theta \rangle$ as function of the Dean number $\mathcal{D}e$ for a double-curved channel with inner radius $r_i = 1$, aspect ratio $\eta = r_i/r_o = 0.9$ and $b = 0.9$. The bifurcation from Poiseuille flow to vortex flow occurs at $\mathcal{D}e \approx 30.5$. The colored pictures depict snapshots of the vorticity, measured on a channel cross-section, where the blue (right) and red (left) spots correspond to clockwise and counterclockwise rotating vortices, respectively.

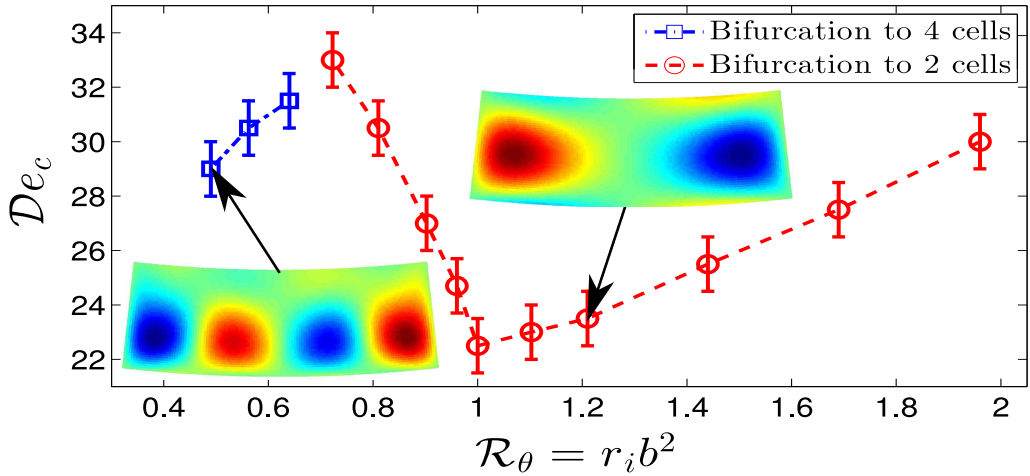


Figure 3.8: **Critical Dean number vs. streamwise curvature radius \mathcal{R}_θ for a double-curved channel.** The critical Dean number $\mathcal{D}e_c$ is measured at the first bifurcation point for a double-curved channel with aspect ratio $\eta = r_i/r_o = 0.9$. The streamwise curvature radius $\mathcal{R}_\theta = r_i b^2$ of the channel varies with b , while the inner radius r_i remains fixed. The colored pictures depict a selection of snapshots of the streamwise vorticity of the flow, measured on a channel cross-section.

fluid is initialized with a uniform mass distribution by setting $\rho = 1$ at $t = 0$. The Dean number is varied by changing the strength of the driving force.

Again, we plot the average vorticity $\langle \omega^\theta \rangle$ as function of the Dean number $\mathcal{D}e$ in order to determine the critical Dean number, at which the vorticity suddenly increases. Exemplarily, Figure 3.7 shows the vorticity curve for $b = 0.9$. As can be observed, the vorticity begins to increase at Dean number $\mathcal{D}e_c \approx 30$, which indicates an imperfect bifurcation from Poiseuille flow to 2-cell vortex flow. Compared to the cylindrical channel, this transition is however rather smooth. The colored pictures in Figure 3.7 depict the vorticity ω^θ on a cross-section.

We have measured the critical Dean number at the bifurcation point for different streamwise curvatures $\mathcal{R}_\theta = r_i b^2$. The results are depicted in Figure 3.8, where errorbars represent the uncertainty in reading off the critical Dean number from the vorticity curve. Two bifurcation points have been observed:

3.3. FLOWS THROUGH DOUBLE-CURVED CHANNELS

a bifurcation from Poiseuille flow to 2-cell vortex flow for $\mathcal{R}_\theta > 0.7$ and a bifurcation from Poiseuille flow to 4-cell vortex flow for $\mathcal{R}_\theta < 0.7$. Figure 3.8 shows that the critical Dean number for the bifurcation to 2-cell vortex flow possesses a minimum at a streamwise curvature $\mathcal{R}_\theta = 1.00 \pm 0.05$, which corresponds to the spherical geometry, where all semi-principal axes of the ellipsoid are equal. For $\mathcal{R}_\theta = 1.00 \pm 0.05$, the instability occurs already at a relatively low Dean number of $\mathcal{D}e_c \approx 22.5$.

For $\mathcal{R}_\theta > 1$, the geometry of the channel is equivalent to a streamwise stretched ellipsoid, such that the streamwise curvature is expected to have only a minor influence on the instability relative to the spherical case $\mathcal{R}_\theta = 1.00 \pm 0.05$. Still, the critical Dean number increases almost linearly with \mathcal{R}_θ for $\mathcal{R}_\theta > 1$, which suggests that the second curvature \mathcal{R}_ϕ dominates the instability in this regime.

For $\mathcal{R}_\theta < 1$, on the other hand, the geometry of the channel resembles an ellipsoid compressed in streamwise direction, and the instability is dominated by the increasing streamwise curvature. For $\mathcal{R}_\theta < 1$, we have observed the following behavior of the flow next to the bifurcation point:

Right before the vortices begin to develop, there are four regions of slightly increased vorticity: Two next to the center of the outer wall at r_o and two next to the corners of the inner wall at r_i . This can be seen in the lower colored picture in Figure 3.7, next to the bifurcation point. For $0.7 < \mathcal{R}_\theta < 1$, the two inner regions dominate and finally form two major vortices (see the upper colored picture in Figure 3.7). For $\mathcal{R}_\theta < 0.7$, on the other hand, the two vorticity regions in the corner also grow in strength and, together with the two inner regions, they finally form four major vortices (see the left colored picture in Figure 3.8). This behavior is different from the case $\mathcal{R}_\theta > 1$, where we observe only two regions of increased vorticity in the beginning, which finally form two major vortices.

3.3.2.2 Variation of cross-sectional curvature

We also have studied the effect of the cross-sectional curvature radius $\mathcal{R}_\phi = r_i$ on the Dean instability by varying the inner radius r_i of the channel.

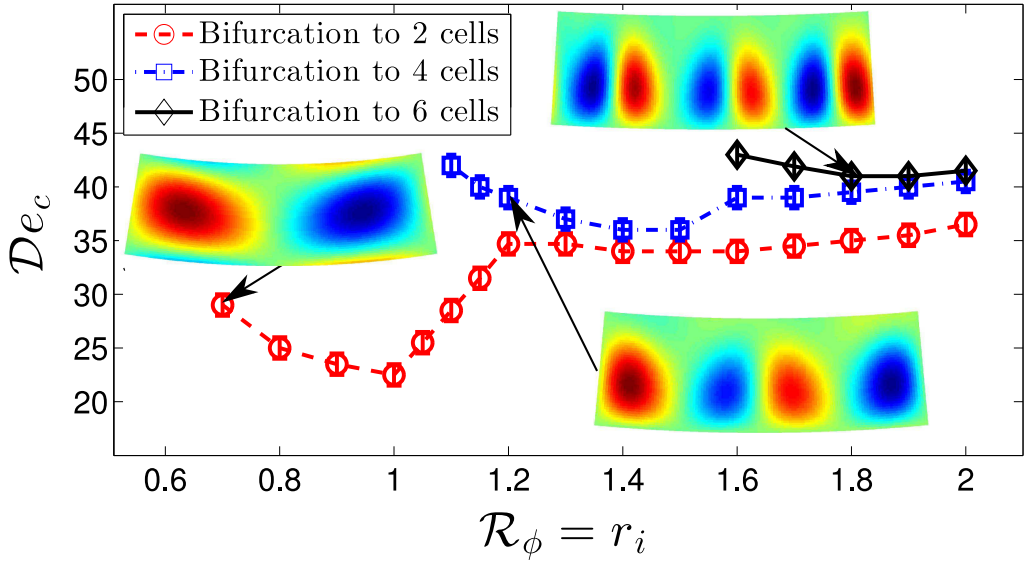


Figure 3.9: **Critical Dean number vs. cross-sectional curvature radius \mathcal{R}_ϕ for a double-curved channel.** The critical Dean number De_c varies with the inner channel radius r_i , while the aspect ratio $\eta = r_i/r_o = 0.9$ as well as the streamwise curvature radius \mathcal{R}_θ remain fixed. The colored pictures depict a selection of snapshots of the streamwise vorticity of the flow, measured on a channel cross-section.

The streamwise curvature radius $\mathcal{R}_\theta = r_i b^2$ is set to 1 and is kept fixed in all simulations by setting $b = 1/\sqrt{r_i}$. The aspect ratio of the channel is set to $\eta = 0.9$, and the lattice spacing in radial direction is given by $\Delta r = (1 - \eta)/(\eta L_r)$. In order to keep the physical dimensions of the channel fixed when r_i varies, the lattice spacings in θ - and ϕ -direction are rescaled accordingly: $\Delta\theta = \Delta r/(b r_i)$, $\Delta\phi = \Delta r/r_i$.

Like in previous studies, we have analyzed the vorticity curve as function of the Dean number. Depending on the cross-sectional curvature radius \mathcal{R}_ϕ , we have found three different bifurcations: a bifurcation from Poiseuille flow to 2-cell vortex flow, from 2 cells to 4 cells as well as from 4 cells to 6 cells. Figure 3.9 depicts the dependence of the critical Dean number at the transition points on the curvature radius \mathcal{R}_ϕ . The first bifurcation is the bifurcation from curved channel Poiseuille flow to 2-cell vortex flow. As can be

3.3. FLOWS THROUGH DOUBLE-CURVED CHANNELS

observed, the critical Dean number for this transition possesses a minimum at $\mathcal{R}_\phi = 1.00 \pm 0.05$, corresponding to a spherical channel geometry, and the minimum value of the critical Dean number, $\mathcal{D}e_c \approx 22.5$ at $\mathcal{R}_\phi = 1.00 \pm 0.05$ coincides with the corresponding value in Figure 3.8 for the spherical case ($\mathcal{R}_\theta = 1$). As can be seen in Figure 3.9, the critical Dean number increases with the cross-sectional curvature $1/\mathcal{R}_\phi$ for $\mathcal{R}_\phi < 1$. This suggests that for $\mathcal{R}_\phi < 1$ the instability is dominated by the cross-sectional curvature $1/\mathcal{R}_\phi$. For $\mathcal{R}_\phi > 1$ on the other hand, the critical Dean number grows almost linearly from 22.5 at $\mathcal{R}_\phi = 1$ to a value of about 35 at $\mathcal{R}_\phi = 1.2$, while a second bifurcation from 2-cell to 4-cell vortex flow begins to appear at higher Dean numbers. In this range, the instability is dominated by the perpendicular streamwise curvature $1/\mathcal{R}_\theta$. For $\mathcal{R}_\phi > 1.2$, the critical Dean number of the first bifurcation stays more or less constant, whereas the threshold for the second bifurcation decreases further and further until it reaches a minimum at $\mathcal{R}_\phi = 1.55 \pm 0.05$. At this point, the third bifurcation from 4-cell to 6-cell vortex flow appears, while the critical Dean number at the first bifurcation point approaches the corresponding value for the cylindrical channel in the limit $\mathcal{R}_\phi \rightarrow \infty$.

From the qualitative point of view, the three curves in Figure 3.9 show a similar behaviour: Starting from different values of \mathcal{R}_ϕ , within error bars all curves decrease to a minimum value right before the next bifurcation emerges. When the next bifurcation appears, the critical Dean number of the lower bifurcation increases to a rather constant value, which grows only slightly towards $\mathcal{R}_\phi \rightarrow \infty$.

Physically, the appearance of 4-cells or 6-cells can be explained by the splitting mechanism described in Ref. [63]: By increasing the Dean number, the Dean vortices can split up and form new vortex pairs. Although, one might wonder why there is no direct bifurcation from 4 cells to 8 cells, since in theory, the 4 vortices should be completely indistinguishable. In practice, however, the symmetry between the cells is broken by small perturbations, which leads to the splitting of only one vortex pair, resulting in the 6-cell solution. From the numerical point of view, we have checked the physicality

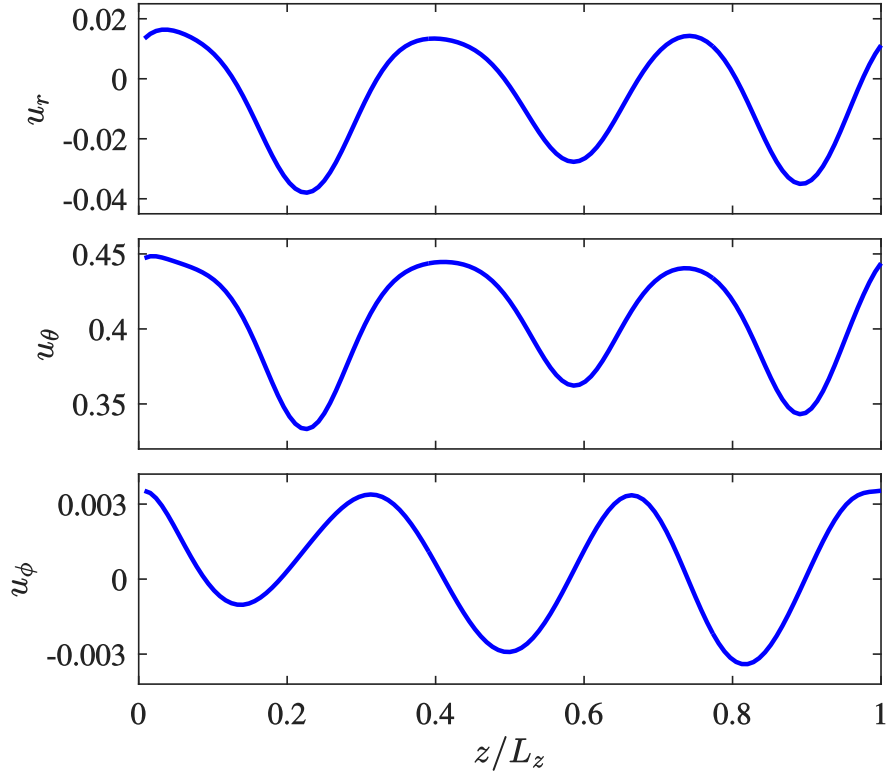


Figure 3.10: **Velocity profiles of vortex flow in a double-curved channel.** The three curves correspond to the radial, streamwise and spanwise velocity profiles, respectively, for 6-cell vortex flow in a double-curved channel with aspect ratio $\eta = 0.9$, streamwise curvature $\mathcal{R}_\theta = 1$, cross-sectional curvature $\mathcal{R}_\phi = 1.8$ and Dean number $\mathcal{D}e = 44$.

of the 6-cell solution by doubling the grid resolution as well as by changing the triggering mechanism, finding the same result in both cases. Exemplarily, Figure 3.10 shows the cross-sectional velocity profile of a 6-cell vortex flow for $\mathcal{R}_\phi = 1.8$ and $\mathcal{D}e = 44$.

3.4 Summary

Summarizing, we have studied the Dean instability in a double-curved channel, using our previously developed LB algorithm in general coordinates. The double-curved channel is characterized by a streamwise curvature as well as by a perpendicular cross-sectional curvature. In analogy with cylindrical channels, which have been widely studied in the past, we have observed a bifurcation from primary curved channel Poiseuille flow to secondary Dean vortex flow, which is characterized by counter-rotating vortices. In particular, we have measured the critical Dean number at the bifurcation points as function of the geometrical properties of the channel.

At first, we have varied the streamwise curvature radius \mathcal{R}_θ while keeping the cross-sectional curvature radius \mathcal{R}_ϕ fixed. We have found that the critical Dean number at the bifurcation from Poiseuille flow to 2-cell vortex flow is minimal for $\mathcal{R}_\theta \approx \mathcal{R}_\phi$, where the channel possesses a spherical symmetry. For channels with weaker or stronger streamwise curvature, the critical Dean number increases almost linearly. For strongly-curved channels, we even have observed bifurcations from Poiseuille flow to 4-cell vortex flow.

Secondly, we also have varied the cross-sectional curvature radius \mathcal{R}_ϕ while keeping the streamwise curvature fixed. Again, we have found that the lowest Dean number at which the Dean instability occurs corresponds to the spherically symmetric configuration, in which both curvature radii are approximately equal, $\mathcal{R}_\theta \approx \mathcal{R}_\phi$, as before. When the cross-sectional curvature decreases towards the cylindrical channel limit, $\mathcal{R}_\phi \rightarrow \infty$, higher order bifurcations from 2-cell flow to 4-cell flow and even from 4-cell flow to 6-cell vortex flow come into play, while the critical Dean number of the first bifurcation from Poiseuille flow to 2-cell flow approaches the corresponding value for the cylindrical channel.

Chapter 4

Poiseuille flow in curved spaces

This chapter is reprinted with minor editing from *J.-D. Debus, M. Mendoza, S. Succi, H. J. Herrmann: “Poiseuille flow in curved spaces”, Phys. Rev. E 93, 043316 (2016)*, Ref. [65]. Copyright (2016) by the American Physical Society.

4.1 Introduction

In this chapter, we investigate transport through intrinsically curved spaces by studying the flux of Poiseuille-like channel flow in dependence of the spatial deformation of the channel. To this end, the metric tensor, characterizing the intrinsic geometry of the channel, is equipped with local perturbations, introducing physical curvature in the medium. The motion of the fluid flow through the curved channel is then simulated according to the covariant Navier-Stokes equations, as illustrated in Figure 4.1.

For different families of curved spaces, including two- and three-dimensional channels with regularly and randomly arranged metric perturbations (see Figs. 4.2 and 4.6 for a sketch), we measure the mass flow in the stationary state in dependence of the metric parameters. Interestingly, we find that plotting the mass flow as function of the average metric perturbation, all data points – for all curved spaces considered – collapse onto a single curve, which we describe by an empirical flux law. We conclude that transport through curved spaces depends only on the average spatial deformation and

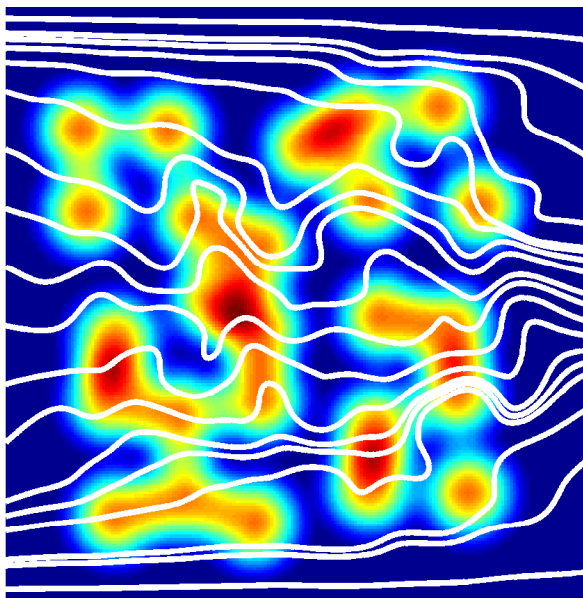


Figure 4.1: **Velocity streamlines of a fluid driven through a curved medium with randomly distributed metric perturbations.** The colors represent the strength of the perturbation (δg) added to the diagonal components of the metric tensor, ranging from flat space (blue) to high perturbation (red).

can thus be characterized by a general flux law in two and three dimensions.

For the purpose of this study, we use the LB method on manifolds with a third-order forcing term (see Section 2.5.1) to simulate fluid flow in general coordinates. In contrast to the curvilinear coordinate systems considered in the previous chapter, the metric tensor considered in this chapter gives rise to an intrinsic curvature of space, and thus describes curved spaces which are physically different from Euclidean space.

As an improvement of the forcing term used for the simulations of Dean vortex flow in Chapter 3, we employ the correction scheme presented in Section 2.5.3, canceling discrete lattice effects by a redefinition of the macroscopic moments (density and velocity). We show that due to the forcing term correction scheme the accuracy of the method is considerably improved.

4.2 Simulation setup

In order to study Poiseuille-like channel flow for different types of curved spaces, we disturb the flat space by adding local perturbations to the metric tensor, resulting in a physical curvature of space¹. In the following, we work in Cartesian-like coordinates $(x^1, x^2, x^3) = (x, y, z)$, such that the metric tensor of the flat space reads $g_0 = \mathbb{1}$. The perturbed metric tensor with N perturbations (labeled by an index i) is then given by

$$g = (1 + \delta g) \cdot \mathbb{1} = \left(1 + \sum_{i=1}^N \delta g_i \right) \cdot \mathbb{1}, \quad (4.1)$$

where δg_i denotes the contribution of the i -th perturbation. The individual metric perturbations are chosen to be of the shape

$$\delta g_i = \begin{cases} -a_0 \cos^2 \left(\pi \frac{r_i}{r_0} \right), & r_i \leq \frac{r_0}{2}, \\ 0, & r_i > \frac{r_0}{2}, \end{cases} \quad (4.2)$$

where $r_i = \|\vec{r} - \vec{r}_i\|$ denotes the distance to the center \vec{r}_i of the i -th perturbation. The parameters a_0 and r_0 characterize the amplitude and the range of

¹This has to be distinguished from a simple coordinate transformation into curvilinear coordinates, which would not introduce spatial curvature.

the perturbation, respectively. We further define the density n of the perturbations by $n = N/V_0$, where V_0 denotes the volume of the flat background medium. Since the individual perturbations possess a rotational symmetry, we will call this type “radial perturbations.”

In the simulations, the fluid is driven through the medium by a constant external force corresponding to a pressure drop of $\nabla P = 10^{-5}$ in x -direction. The channels are modeled with periodic boundary conditions in the stream-wise direction (at $x = 0, x = L_x$) and fixed walls at the perpendicular boundaries (at $y = 0, y = L_y$ and $z = 0, z = L_z$). At the walls, zero-velocity boundary conditions are imposed, entering the algorithm through the equilibrium distribution f^{eq} , which is evaluated with $u = 0$ at the wall nodes.

For all two-dimensional simulations, we use a $D3Q41$ lattice (see Table 2.2) of size $L_x \times L_y \times L_z = 256 \times 256 \times 1$, and set the discretization step to $\Delta t = \Delta x^i = 0.5$. The viscosity of the fluid is set to $\nu = c_s^2(\tau - \frac{1}{2}) \Delta t = c_s^2/4$, which fixes the relaxation parameter τ correspondingly. The three-dimensional simulations, on the other hand, are performed on a lattice of size $L_x \times L_y \times L_z = 64 \times 64 \times 64$ with $\Delta t = \Delta x^i = 1$ and $\nu = c_s^2(\tau - \frac{1}{2}) \Delta t = c_s^2/2$.

After the fluid has reached the stationary state, we measure the average flux of the flow, which in curved space is given by

$$\Phi = \frac{1}{S} \int_S g(\rho u, n_x) dS = \frac{1}{S} \int_S \rho u^x \sqrt{g} dy dz, \quad (4.3)$$

where n_x denotes the unit vector in x -direction, and the integral runs over a channel cross-section with area element $dS = \sqrt{g_{yy} g_{zz}} dy dz$ and total area $S = \int_S dS$. In particular, we are interested in the relative deviation of the flux from the corresponding flux of the standard Poiseuille flow in flat space, Φ_0 , which is described by

$$\Delta\Phi := \frac{\Phi_0 - \Phi}{\Phi_0}.$$

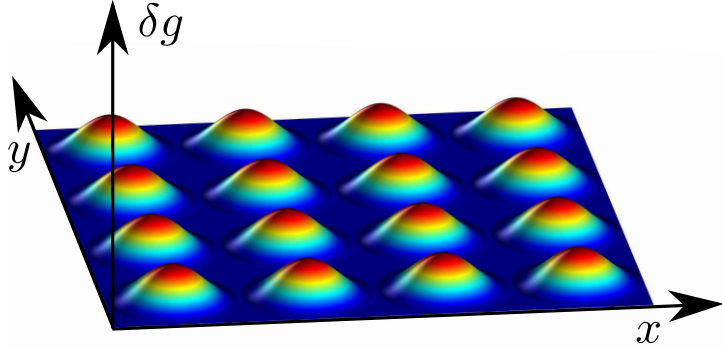


Figure 4.2: **Curved medium with regularly arranged metric perturbations.** The colors illustrate the strength of the perturbations, ranging from 0 (blue) to a_0 (red), where a_0 denotes the amplitude of the perturbations.

4.3 Poiseuille flow in curved spaces

4.3.1 Transport in 2D curved media

For simplicity, we first consider a two-dimensional periodic arrangement of metric perturbations, whose positions \vec{r}_n are confined to a regular square lattice,

$$\vec{r}_n = \vec{r}_{n_x, n_y} = (n_x, n_y) \cdot \lambda, \quad n_x, n_y \in \mathbb{Z},$$

where $\lambda = \sqrt{V_0/N}$ denotes the characteristic distance between the perturbations and $V_0 = L_x L_y \Delta x \Delta y$ is the volume of the flat background space (see Figure 4.2 for a sketch).

Because of the periodicity of the metric perturbations, one might be inclined to simulate only one perturbation with periodic boundary conditions in all directions. However, since we put walls at $y = 0, y = L_y$ and since we aim at extending this system to a random arrangement of perturbations, we simulate the entire regular system. In order to find the dependence of the flux on the perturbation amplitude a_0 , range r_0 , and density $n = N/V_0$, we have performed simulations for a wide range of parameters. Our simulations range from dilute media ($r_0 < \lambda$), for which the metric perturbations are spatially separated from each other, to very dense media ($r_0 \gg \lambda$), where the metric

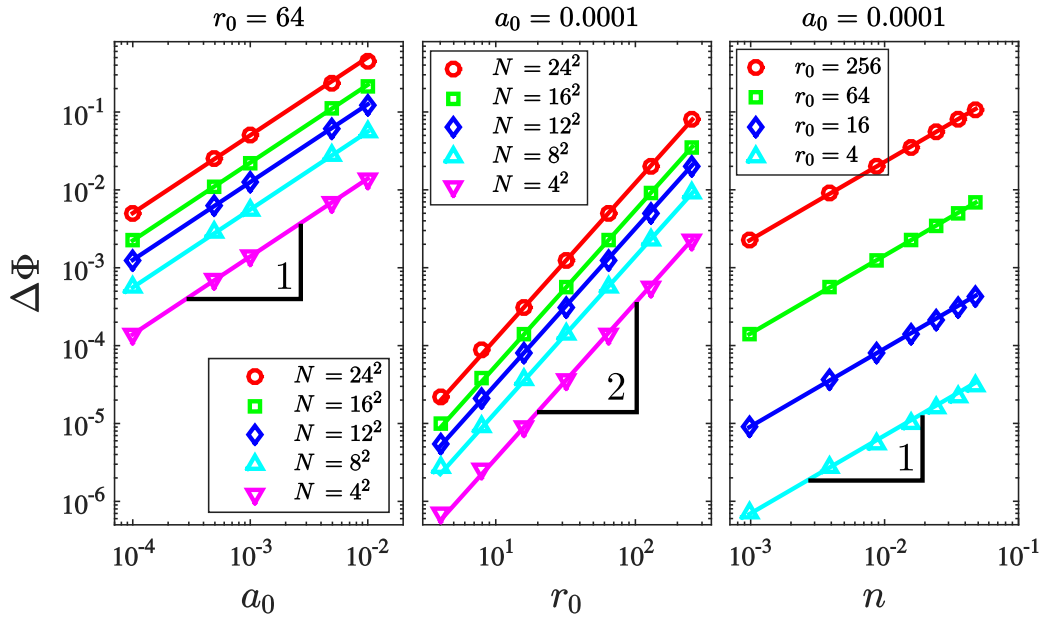


Figure 4.3: **Flux vs. metric parameters for 2D regularly arranged metric perturbations.** The data points depict the flux deficit $\Delta\Phi = \frac{\Phi_0 - \Phi}{\Phi_0}$, measured on a channel cross-section in the stationary state, as function of the amplitude a_0 (a), range r_0 (b), and density n (c) of the metric perturbations. The total number of metric perturbations is denoted by N .

4.3. POISEUILLE FLOW IN CURVED SPACES

perturbations overlap and form large clusters. As soon as the fluid reaches its equilibrium state, the average flux is measured according to Eq. (4.3). In Figure 4.3 the flux deficit $\Delta\Phi$ is plotted against the metric parameters in a double-logarithmic plot. As can be seen, all curves follow a power law with integer slopes, even in the regime of overlapping perturbations, $r_0 > \lambda$. From the power law behavior, we infer the following functional dependence of $\Delta\Phi$ on the metric parameters:

$$\Delta\Phi = C_0 a_0 r_0^2 n + \mathcal{O}(a_0^2), \quad (4.4)$$

where C_0 is a constant. We recognize that this expression resembles the average metric perturbation, which is defined as

$$\langle \delta g \rangle = \frac{1}{V_0} \int \delta g \, d^D x. \quad (4.5)$$

Plugging in the explicit expression for the radial perturbations (4.2) in two dimensions, we obtain

$$\langle \delta g \rangle = -\frac{\pi^2 - 4}{8\pi} a_0 r_0^2 n. \quad (4.6)$$

Thus, we can rewrite Eq. (4.4) as follows:

$$\Phi = \Phi_0 \cdot \left(1 + C_1 \cdot \langle \delta g \rangle + \mathcal{O}(a_0^2) \right), \quad (4.7)$$

where $C_1 = 1.500 \pm 0.003$. This relation describes the main contribution of the metric parameters to the flux. In order to check that relation (4.7) is not just a coincidence which only holds for this special type of radial perturbations, we have also studied metric perturbations of a different shape, given by the metric function

$$\delta \tilde{g}_i = \begin{cases} -a_0 \cos^2 \left(\pi \frac{|x-x_i|}{r_0} \right) \cos^2 \left(\pi \frac{|y-y_i|}{r_0} \right), & \text{if } |x-x_i| \leq \frac{r_0}{2}, |y-y_i| \leq \frac{r_0}{2}, \\ 0, & \text{else,} \end{cases} \quad (4.8)$$

where $\vec{r}_i = (x_i, y_i)$ denotes the center of the i -th perturbation. We will refer to this type as “square perturbations,” as their support is a square, and mark

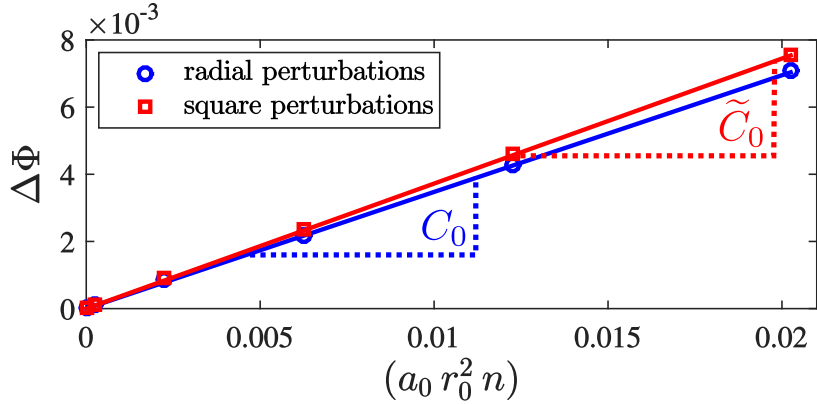


Figure 4.4: **Flux deficit for two different types of metric perturbations.** The data points depicts the flux deficit $\Delta\Phi = \frac{\Phi_0 - \Phi}{\Phi_0}$ as function of the product $a_0 r_0^2 n$ for both radial-shaped and square-shaped metric perturbations. The amplitude $a_0 = 0.001$ and range $r_0 = 16$ are kept fixed while the number of perturbations is varied. The solid lines represent linear fits with slope $C_0 = 0.350 \pm 0.004$ and $\tilde{C}_0 = 0.374 \pm 0.003$, respectively.

all related quantities with a tilde symbol. For the square perturbations, the average metric perturbation is given by

$$\langle \delta \tilde{g} \rangle = -\frac{1}{4} a_0 r_0^2 n,$$

and only differs from the corresponding expression for the radial perturbations, Eq. (4.6), in the constant prefactor. Figure 4.4 depicts the flux deficit $\Delta\Phi$ as function of the parameter combination $(a_0 r_0^2 n)$ for the two different types of metric perturbations. It can be seen that the flux in the simulations with square perturbations exhibits the same functional dependence on the metric parameters,

$$\Delta\tilde{\Phi} = \tilde{C}_0 a_0 r_0^2 n + \mathcal{O}(a_0^2),$$

yet with a different prefactor \tilde{C}_0 . From the linear fits we obtain $C_0 = 0.350 \pm 0.004$ for the slope of the radial perturbations and $\tilde{C}_0 = 0.374 \pm 0.003$ for the square perturbations. Assuming that relation Eq. (4.7) represents a universal flux law, holding for both types of perturbations, the ratio between

4.3. POISEUILLE FLOW IN CURVED SPACES

$\Delta\Phi$ and $\Delta\tilde{\Phi}$ has to be equal to the ratio between $\langle\delta g\rangle$ and $\langle\delta\tilde{g}\rangle$. We find:

$$\frac{\Delta\tilde{\Phi}}{\Delta\Phi} = \frac{\tilde{C}_0}{C_0} = 1.069 \pm 0.004,$$

$$\frac{\langle\delta\tilde{g}\rangle}{\langle\delta g\rangle} = \frac{2\pi}{\pi^2 - 4} = 1.070.$$

Thus, we conclude that — at least for the metric perturbations considered here — relation Eq. (4.7) holds independently of the specific shape of the perturbations.

As already mentioned, relation Eq. (4.7) is expected to be only a linear approximation of the real functional dependence of Φ on $\langle\delta g\rangle$. In order to find the higher-order contributions, we have also performed simulations for stronger spatial deformations, for which we expect non-linear effects. To this end, we have again varied all metric parameters within a wide range of perturbation amplitudes a_0 , and we also included the case of negative amplitudes $a_0 < 0$. Figure 4.5 shows the resulting curve of Φ/Φ_0 as a function of $\langle\delta g\rangle$. As can be seen, all data points fall indeed on one single curve, which leads to the conclusion that even beyond the first-order approximation in a_0 , the flux is well-described as a function of $\langle\delta g\rangle$. From Figure 4.5, we find the following flux law:

$$\Phi = \Phi_0 \cdot (1 + \alpha^2 \cdot \langle\delta g\rangle + 2\alpha^2\beta \cdot \langle\delta g\rangle^2), \quad (4.9)$$

where $\alpha = 1.223 \pm 0.001$ and $\beta = 0.165 \pm 0.001$ are fitting parameters. This flux law is valid for metric perturbations $|\langle\delta g\rangle| \leq 1$ and supports our expectations about transport in curved media: By adding a metric perturbation δg to the flat space, the space becomes either stretched ($\delta g > 0$) or compressed ($\delta g < 0$). In the first case, $\delta g > 0$, the cross-section of the medium is increased by the presence of the metric perturbations, such that the transport through the medium is enhanced and the flux increases compared to the flat space. For negative metric perturbations, $\delta g < 0$, on the other hand, the channel cross-section is decreased, and the fluid transport deteriorates compared to the flat space.

We also investigated the case of randomly distributed metric perturbations (see Figure 4.6 for a sketch) in order to study the dependence of the

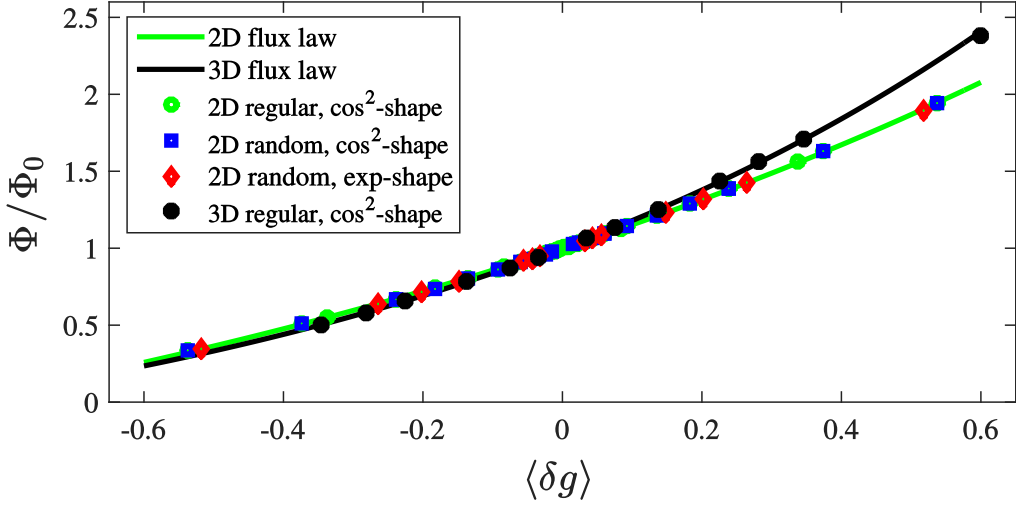


Figure 4.5: General flux law in 2D and 3D. The data points represent the flux ratio Φ/Φ_0 , measured in the stationary state, as function of the average strength of the metric perturbations $\langle\delta g\rangle$. Each point corresponds to a differently curved medium, differing by the dimension (2D and 3D), the spatial arrangement (regularly and randomly), the amplitude a_0 , range r_0 and number density n , as well as by the shape of the metric perturbations ($\delta g \sim \cos^2(\pi r/r_0)$ (4.2) and $\delta g \sim \exp(-r/r_0)$ (4.10)). As can be observed, all data points – independently of the individual shape of the media – collapse onto single common curves in 2D and 3D, which can be fitted by quadratic flux laws (depicted by the solid lines), given by Eqs. (4.9) and (4.11), respectively.

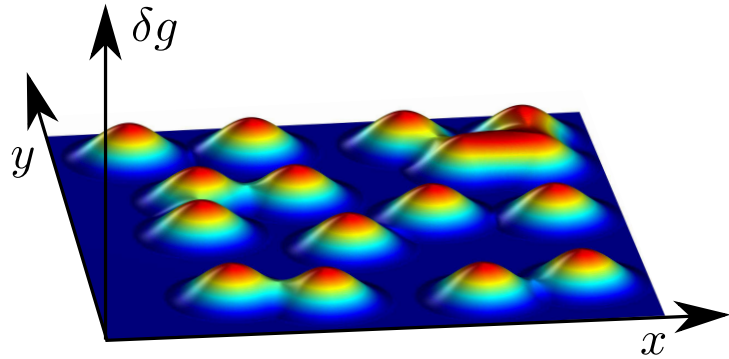


Figure 4.6: Curved medium with randomly arranged metric perturbations. The colors illustrate the strength of the metric perturbation, ranging from 0 (blue) to a_0 (red), where a_0 denotes the amplitude of the perturbations.

4.3. POISEUILLE FLOW IN CURVED SPACES

Poiseuille flow on the spatial order of the metric perturbations. For small amplitudes a_0 , the spatial arrangement of perturbations does not affect the linear order of the average metric perturbation, given by Eq. (4.6). Accordingly, we find that the dependence of $\Delta\Phi$ on the metric parameters is exactly the same as in the regular case, given by Eq. (4.4), and the flux is thus well-described as a function of $\langle \delta g \rangle$. Even for larger amplitudes a_0 , the flux curve does not change notably from the case of regularly arranged metric perturbations, as can be seen in Figure 4.5. We find that the flux follows Eq. (4.9) with fitting parameters $\alpha = 1.224 \pm 0.002$ and $\beta = 0.158 \pm 0.005$, in agreement with the corresponding values for regularly arranged metric perturbations. Thus, we conclude that — within the range of parameters studied — the spatial order of the metric perturbations does not significantly affect the behavior of the flux.

In order to check that the flux law also holds for metric perturbations with non-compact support, we performed further simulations for exponentially shaped perturbations of the form

$$\delta g_i = -a_0 \exp(-r_i/r_0), \quad (4.10)$$

distributed randomly in space. For this type, the average metric perturbation yields $\langle \delta g \rangle = -2\pi a_0 r_0^2 n$, and the simulations results have been added to Figure 4.5 with fitting coefficients $\alpha = 1.225 \pm 0.001$ and $\beta = 0.144 \pm 0.002$. As can be seen, the flux curve coincides with the other flux curves in 2D, which supports our claim that the flux law Eq. (4.9) holds universally.

Additionally, we simulated media with both positive and negative metric perturbations (see Figure 4.7 for a sketch). If the flux law Eq. (4.9) holds in general, any non-trivial configuration of perturbations with $\langle \delta g \rangle = 0$ should give the same value for the flux, namely $\Phi = \Phi_0$. To test this statement, we have performed simulations for a wide range of metric parameters, $a_0 \in \{\pm 0.0001, \pm 0.001, \pm 0.01\}$, $r_0 \in \{4, 8, 16, 32, 64, 128\}$, $N \in \{16, 64\}$, all satisfying $\langle \delta g \rangle = 0$. Indeed, we find that all simulations give the same flux Φ_0 with a standard deviation of about 0.2%.

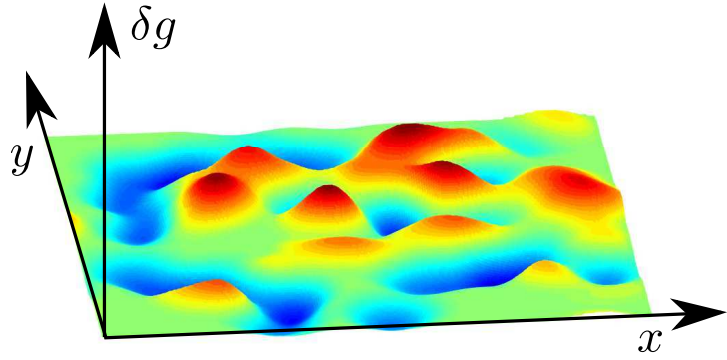


Figure 4.7: Curved medium with mixed positive and negative metric perturbations. The colors illustrate the strength of the metric perturbation, ranging from $-a_0$ (blue) to $+a_0$ (red), where a_0 denotes the amplitude of the perturbations.

4.3.2 Transport in 3D curved media

Next, we consider a three-dimensional curved channel equipped with N regularly arranged metric perturbations at positions

$$\vec{r}_n = \vec{r}_{n_x, n_y, n_z} = (n_x, n_y, n_z) \cdot \lambda, \quad n_x, n_y, n_z \in \mathbb{Z},$$

where $\lambda = \sqrt[3]{V_0/N}$ denotes the characteristic distance between the metric perturbations and $V_0 = L_x L_y L_z \Delta x \Delta y \Delta z$ is the volume of the flat background space.

Like for the two-dimensional cases, we study the dependence of the Poiseuille flow on the metric parameters, as depicted in Figure 4.8. We find that — at leading order in the metric perturbations — the flux deficit is given by

$$\Delta\Phi = C_0 a_0 r_0^3 n + \mathcal{O}(a_0^2),$$

C_0 being a constant. In analogy to the two-dimensional case, the expression $(a_0 r_0^3 n)$ corresponds to the average metric perturbation in three dimensions, given by

$$\langle \delta g \rangle = -\frac{\pi^2 - 6}{12\pi} a_0 r_0^3 n.$$

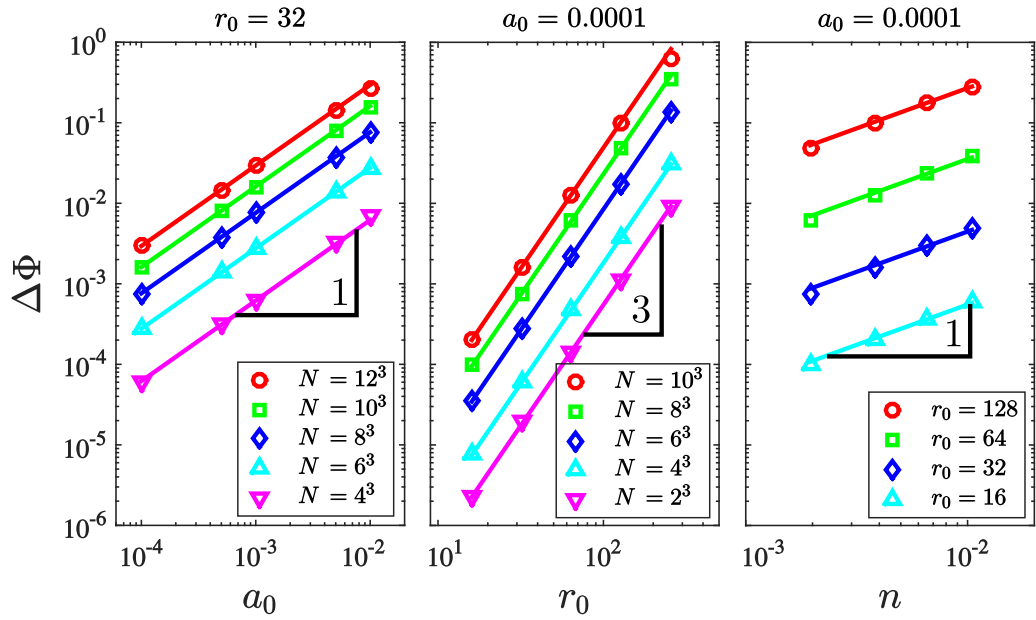


Figure 4.8: **Flux vs. metric parameters for 3D regularly arranged metric perturbations.** The data points depict the flux deficit $\Delta\Phi = \frac{\Phi_0 - \Phi}{\Phi_0}$, measured on a channel cross-section in the stationary state, as function of the amplitude a_0 (a), range r_0 (b), and density n (c) of the metric perturbations. The total number of metric perturbations is denoted by N .

Plotting the flux versus $\langle \delta g \rangle$ for $|\langle \delta g \rangle| \leq 0.6$, as shown in Figure 4.5, we again find that, even beyond the leading order, all points fall on one single curve, which can be described by the flux law

$$\Phi = \Phi_0 \cdot (1 + \alpha^3 \cdot \langle \delta g \rangle + 3\alpha^3\beta \cdot \langle \delta g \rangle^2), \quad (4.11)$$

where the fitting parameters take the values $\alpha = 1.21 \pm 0.01$ and $\beta = 0.17 \pm 0.01$ and thus agree with the corresponding values of the two-dimensional flux law, Eq. (4.9). The flux laws for two and three dimensions might be combined to a generalized law, given by

$$\Phi = \Phi_0 \cdot (1 + \alpha^D \cdot \langle \delta g \rangle + D\alpha^D\beta \cdot \langle \delta g \rangle^2), \quad (4.12)$$

where D denotes the dimension of the system, and $\alpha \approx 1.22$ and $\beta \approx 0.16$ are universal constants.

4.4 Comparison with a previous study

The findings presented in this chapter generalize the results of a previous study [1] of three-dimensional curved media equipped with randomly distributed metric perturbations of exponential shape, $\delta g_i = -a_0 \exp(-r_i/r_0)$. In the previous study, only positive amplitudes (corresponding to negative values of $\langle \delta g \rangle$) were considered, and the flux was found to obey the laws

$$\Phi_0 - \Phi = A_0 \frac{N/N_0}{1 + (N/N_0)^2}, \quad (4.13)$$

$$\Phi_0 - \Phi = A_0 \frac{(\epsilon/\epsilon_0)^3}{1 + (\epsilon/\epsilon_0)^6}, \quad (4.14)$$

where N denotes the number of metric perturbations, $\epsilon = r_0/\lambda$ the dimensionless deformation, $\lambda = \sqrt[3]{V_0/N}$ the characteristic length, V_0 the volume of the flat background space, and A_0 , N_0 , and ϵ_0 are constant fitting parameters. Calculating the average metric perturbation for this perturbation type, we obtain

$$\langle \delta g \rangle = -8\pi a_0 r_0^3 n = -8\pi a_0 \epsilon^3.$$

With that, Eqs. (4.13) and (4.14) can be combined into a single equation of the following form:

$$\frac{\Phi}{\Phi_0} \approx 1 + \tilde{A}_0 \frac{\langle \delta g \rangle / \langle \delta g \rangle_0}{1 + (\langle \delta g \rangle / \langle \delta g \rangle_0)^2}, \quad (4.15)$$

where \tilde{A}_0 and $\langle \delta g \rangle_0$ are constants. Restricting to positive amplitudes, i.e., $\langle \delta g \rangle < 0$, the flux curves depicted in Figure 4.5 are indeed well-described by Eq. (4.15), confirming that the flux law in Ref. [1] is consistent with our present results. However, Eq. (4.15) fails to describe the correct behavior for negative amplitudes (corresponding to $\langle \delta g \rangle > 0$) and should thus be replaced by our more general flux law proposed in this work. Our flux law also explains the power law dependence of the flux deficit on ϵ for small a_0 found in Ref. [1], since, at leading order in a_0 , $(\Phi_0 - \Phi) \sim \langle \delta g \rangle \sim r_0^3 n = \epsilon^3$.

4.5 Method validation

4.5.1 Improvements by cancelation of discrete lattice effects

In this section we validate the improvements of our method by the cancelation of discrete lattice effects, arising from the forcing term of the LB equation. As already mentioned in Section 2.5.3, discrete lattice effects manifest themselves as spurious source terms of order Δt in the Navier-Stokes equations (2.29)-(2.30), which — depending on the strength of the spatial deformation — can crucially affect the motion of the fluid. To illustrate this effect, we have performed two-dimensional simulations *with* and *without* the spurious source terms of order Δt for a curved medium with 8 metric perturbations of amplitude $a_0 = 0.1$ and range $r_0 = 22$. The fluid is driven through the medium by an external force, corresponding to a pressure drop of $\nabla P = 10^{-6}$ in x -direction, and the relaxation time is set to $\tau = 1$. Figure 4.9 depicts the velocity streamlines of the fluid for a simulation with discrete lattice effects (*left*) and the same simulation using the corrected method (*right*).

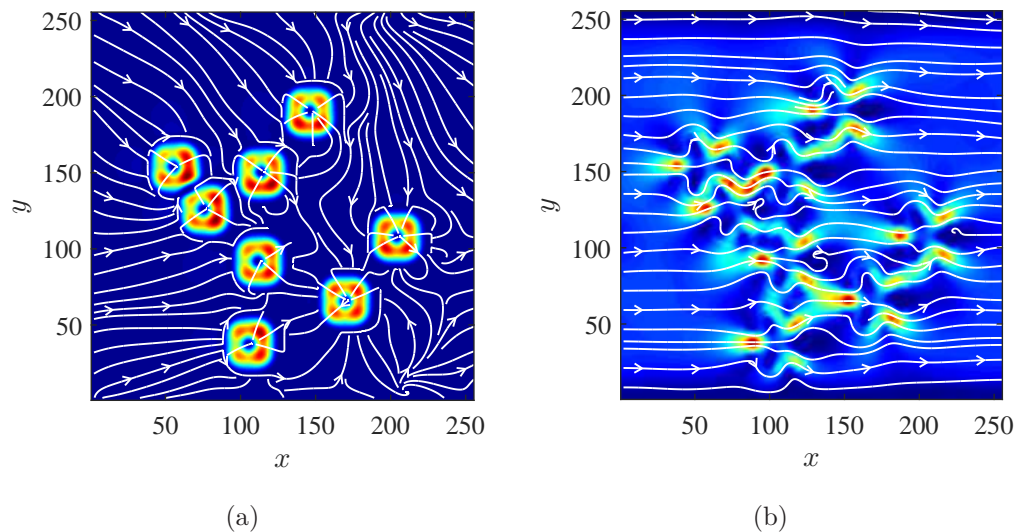


Figure 4.9: **Improvement of the velocity field by cancellation of discrete lattice effects.** The white lines illustrate the velocity streamlines and the colors the absolute value of the velocity (from 0 (blue) to high velocities (red)) for a simulation with $N = 8$ metric perturbations of amplitude $a_0 = 0.1$ and range $r_0 = 22$. (a) Simulation with discrete lattice effects: The nonphysical sinks originating from spurious source terms are well-visible and crucially distort the flow. (b) Improved model without discrete lattice effects: The sinks have disappeared, and the fluid motion appears much more physical.

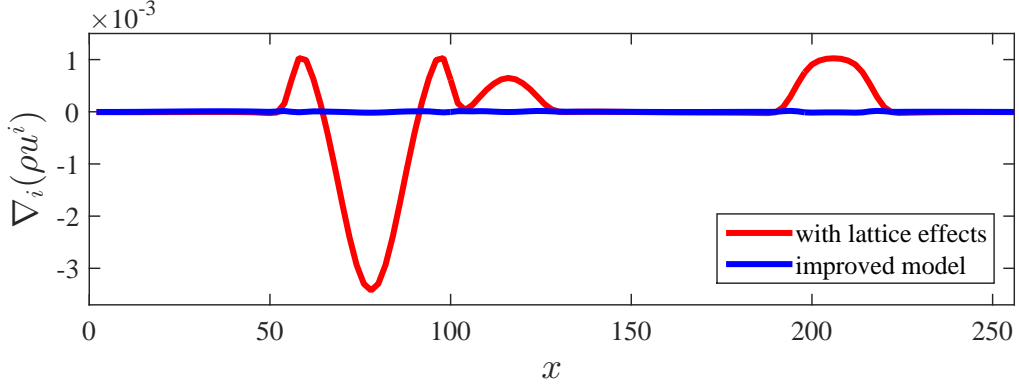


Figure 4.10: **Improvement of the divergence of the flow velocity by cancellation of discrete lattice effects.** The divergence field $\nabla_i(\rho u^i)$ is measured as function of the position x on a cross-section $y = \frac{1}{2}L_y$. The red curve corresponds to the old model, showing large fluctuations in the divergence field due to discrete lattice effects, resulting in the spurious sinks in the velocity field depicted in Figure 4.9. The blue curve represents the improved model, in which discrete lattice effects are actively canceled at order Δt . Indeed, we measure $\nabla_i(\rho u^i) \approx 0$, implying the absence of spurious sinks.

In the left figure, the large nonphysical sinks in the velocity field, originating from the spurious source terms in the Navier-Stokes equations, are clearly visible. By properly correcting the density and velocity fields in each time step, as described in Section 2.5.3, these nonphysical source terms are eliminated at order Δt , leading to the source-free velocity field depicted in Figure 4.9(b). The improvement becomes even more obvious for the divergence field of the velocity, which is plotted as function of x in Figure 4.10. According to the continuity Eq. (2.10), $\nabla_i(\rho u^i)$ must vanish identically in the stationary state, which is clearly fulfilled for the corrected method, whereas the uncorrected method causes large deviations due to the nonphysical source terms.

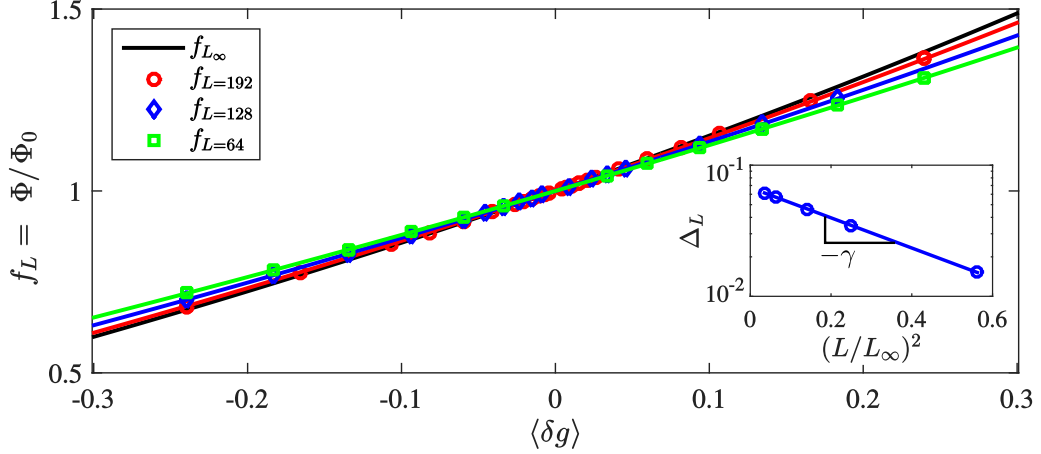


Figure 4.11: **Convergence of the numerical flux law with increasing grid resolution.** The solid lines denote the flux law, Eq. (4.9), fitted to our data for differently curved media, composed of regularly arranged metric perturbations. As can be seen, the curves converge with increasing system size. *Inset:* Relative distance between the curves, denoted by Δ_L , as function of the system size L^2 in a semi-logarithmic plot. As can be seen, the distance decays exponentially with exponent $\gamma = 2.66 \pm 0.05$.

4.5.2 Finite resolution study

To investigate the effect of the grid resolution on our data, we have compared simulations of the curved media described in Section 4.3.1) for different grid resolutions Δx (corresponding to different system lengths $L = 128/\Delta x$). Figure 4.11 depicts the flux curves for different system lengths, $L = 64$, 128, and 192, where we abbreviate the flux ratio at system length L by $f_L := \Phi/\Phi_0$. As can be seen, for increasing system lengths L , the flux curves f_L converge rapidly to the limiting function f_{L_∞} , which we approximate by the flux law given by Eq. (4.9) for $L = 256$. In order to prove the convergence quantitatively, we show that the relative distance between the curves, defined as

$$\Delta_L^2 := \frac{\|f_L - f_{L_\infty}\|^2}{\|f_{L_\infty}\|^2} = \frac{\int |f_L(x) - f_{L_\infty}(x)|^2 dx}{\int |f_{L_\infty}(x)|^2 dx}, \quad (4.16)$$

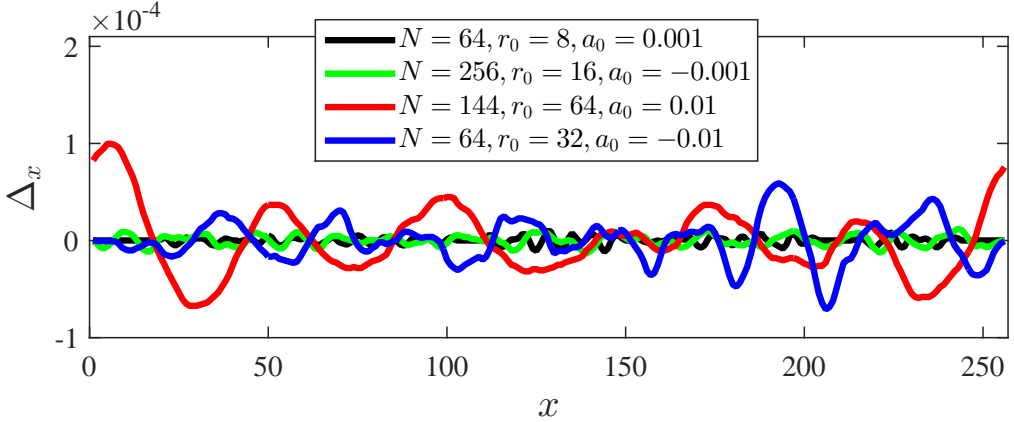


Figure 4.12: Position-dependent numerical fluctuation of the conserved flux. The colored lines depict the relative fluctuation of the flux, given by $\Delta_x = (\Phi(x) - \langle \Phi \rangle_x)/\langle \Phi \rangle_x$, as function of the channel position x , at which the flux is measured. Although the fluctuations should vanish identically due to flux conservation, we observe minor fluctuations of order 10^{-5} due to numerical errors.

converges to zero with increasing system size L^2 . In the inset of Figure 4.11, the relative distance Δ_L is depicted as function of the system size in a semi-logarithmic plot. As can be seen, the flux curves f_L converge to f_{L_∞} exponentially with L^2 ,

$$\Delta_L \sim \exp\left(-\gamma \frac{L^2}{L_\infty^2}\right),$$

with $\gamma = 2.66 \pm 0.05$. Consequently, we conclude that — within an error of about 1% — our numerical results are free of finite resolution effects.

4.5.3 Flux conservation

In order to check to which extent the flux is numerically conserved, it is insightful to plot the profiles $\Phi(x)$ along the channel direction x . In Figure 4.12, the relative fluctuation of the flux around its mean value, $\Delta_x := (\Phi(x) - \langle \Phi \rangle_x)/\langle \Phi \rangle_x$, is plotted versus x for different randomly curved media. As can be seen, the flux varies only marginally with x , with a standard deviation of $\Delta_x \approx 2 \cdot 10^{-5}$. Thus, we conclude that the flux is numerically conserved up to a negligible error of about 0.002%.

The conservation of the flux is closely connected to the improvements of the method discussed in Section 4.5.1, since the flux loss between two channel cross-sections $x = x_1$ and $x = x_2$ is proportional to the (ideally vanishing) divergence of (ρu^i) :

$$\Phi(x_2) - \Phi(x_1) = \frac{1}{S} \oint_{\partial V} g(\rho \vec{u}, \vec{n}) d(\partial V) = \frac{1}{S} \int_V \nabla_i (\rho u^i) dV,$$

where S denotes the area of the channel cross-sections, and V the volume between the cross-sections. Here, we have used Gauss' divergence theorem and the fact that the flux vanishes at the walls. Thus, the smaller the value of the divergence $\nabla_i (\rho u^i)$ (depicted in Figure 4.10), the better the conservation of the flux.

4.6 Summary

In this chapter, we have studied Poiseuille flows in curved spaces, using the LB method on manifolds. We have established a relation between the flux of the Poiseuille flow in the stationary state and the curvature parameters of the medium (e.g. amplitude a_0 , range r_0 , and density n of the metric perturbations) for different types of curved media, starting from two-dimensional media with regularly and randomly arranged metric perturbations and ending with three-dimensional media. In all cases, we found that the flux depends only on a specific combination of parameters, which we have identified as the average metric perturbation,

$$\langle \delta g \rangle \sim a_0 r_0^D n,$$

where D denotes the dimension. Even beyond leading order in the metric perturbations, the flux is well-described as a function of the average metric perturbation $\langle \delta g \rangle$. Our results can be summarized by the following law for the average flux Φ :

$$\Phi = \Phi_0 \cdot (1 + \alpha^D \cdot \langle \delta g \rangle + D \alpha^D \beta \cdot \langle \delta g \rangle^2),$$

4.6. SUMMARY

where Φ_0 denotes the average flux in flat space and α and β are fitting parameters. This relation is universal in the sense that — within the parameter range considered here — it depends neither on the specific shape nor on the spatial order of the metric perturbations and is valid both for two- and three-dimensional systems.

Chapter 5

Energy dissipation induced by curvature

5.1 Introduction

It is well known that free particles follow energy-conserving geodesic motion in curved spaces. In free fluids, i.e. in the complete absence of solid walls or obstacles, one would also expect that flows conserve energy, since there are no obvious sources of dissipation. In this chapter we show that surprisingly this is not the case: in curved spaces, the motion of fluids exhibits energy loss due only to the intrinsic curvature of space. We explain this phenomenon by the fact that the curvature of space changes the direction of the flow trajectories, leading to streamline curvature. The local change in direction of the streamlines (measured by the local change of velocity, ∇u) is directly related to the rate of the kinetic energy density ε_{kin} , since $D_t \varepsilon_{\text{kin}} \approx \nu \|\nabla u\|^2$, where $D_t = \partial_t + u^i \nabla_i$ denotes the material derivative and ν the viscosity of the fluid. In standard fluids in flat space, strong changes in direction of the flow streamlines are typically achieved in the vicinity of solid boundaries, where the fluid molecules undergo sudden changes of direction due to collisions with the solid molecules. In this chapter, we show that even in the absence of solid walls, streamline curvature is induced solely by the intrinsic curvature of space, leading to a local dissipation of energy.

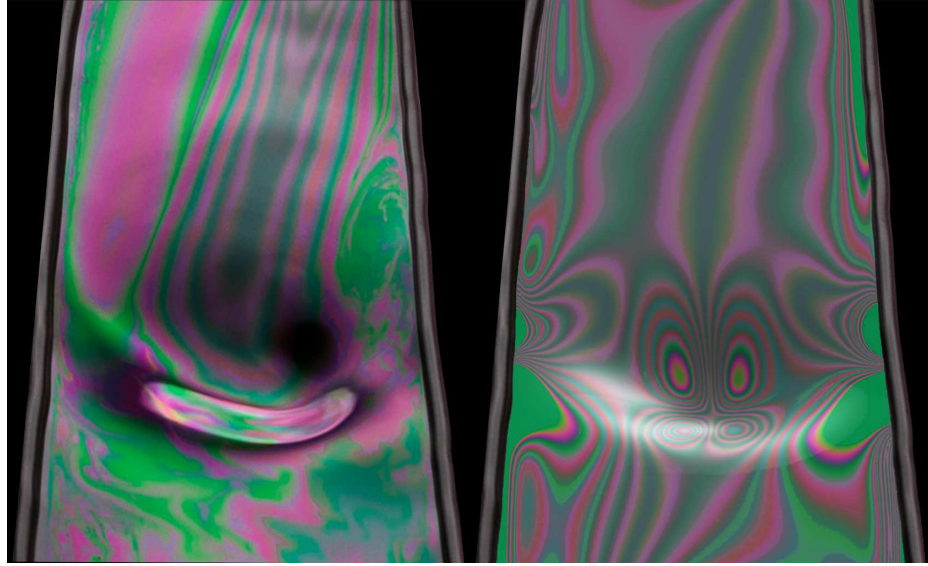


Figure 5.1: Flow down a curved soap film compared to our numerical simulation. *Left:* Soap film experiment. The soap film flows downwards between two vertical wires and possesses a local out-of-plane curvature in the center, produced by a gentle jet of air. The colors correspond to the thickness variations of the soap film and provide an excellent visualization of the film motion. As can be seen, the incoming laminar stream is considerably distorted at the curved bump.² *Right:* Numerical simulation of a soap film with a Gaussian bump in the center, showing similar patterns. Deviations from the experiment originate mainly from the fluid-air interaction which is not taken into account in the simulation.

As a daily-life application of 2D flow on curved surfaces, we consider soap films [16, 17, 19, 18], which occur in a multitude of shapes, thus allowing to study curvature effects on flowing surfaces of nearly arbitrary geometry. As an illustration, the left half of Figure 5.1 shows a self-made soap film, spanned between two vertical wires and flowing downwards, driven by gravity. With a gentle jet of air, obtained by blowing through a straw, we create an out-of-plane curvature, distorting the laminar stream, as can be clearly seen by the colored filaments of the soap film. The colored patterns originate from the thickness variations of the soap film, which are directly correlated

²I specially thank Prof. Troy Shinbrot and Damian Berger for their useful help in preparing the soap film and in the shooting of this photo.

with the vorticity field of the flow [66], and thus provide an excellent visualization of the film motion. The right half of Figure 5.1 shows our numerical simulation of the soap film experiment with a Gaussian bump in the center, showing similar patterns. The colors represent the vorticity field, being directly coupled to the thickness of the soap film [66], and thus correspond to the interference pattern of a real soap film, illuminated by white daylight. As can be seen, there are visible, quadrupol-shaped distortions in the vorticity field, implying velocity gradients and shear next to the curvature source. In this chapter, we analyze this effect in more detail and show that spatial curvature itself – even in the absence of walls, obstacles or interaction with adjacent air – generates viscous forces leading to curvature-induced energy dissipation.

5.2 Computational and experimental setup

As for the study of the Poiseuille flow through curved spaces, the motion of the fluid is described by the covariant Navier-Stokes equations (2.10). As before, we use the LB method on manifolds with an improved second-order forcing term, as described in Section 2.5.2, where discrete lattice effects are canceled by employing the trapezoidal rule for time integration in the LB equation, as presented in Section 2.5.4. Because of the reduced order of the forcing term as well as the simple implementation of the trapezoidal rule, the efficiency of the LB algorithm is considerably increased without loss of second-order accuracy.

The simulations are performed on a two-dimensional *D2Q17* lattice (see Table 2.1) of size 256×128 with a discretization step of $\Delta = \Delta t = \Delta x^i = 0.5$ and a fluid viscosity of $\nu = (\tau - \frac{1}{2}) c_s^2 \Delta t = c_s^2 / 2 \approx 0.185$, which fixes the LB relaxation parameter τ accordingly³. At the inlet and outlet, a non-equilibrium extrapolation method, following Ref. [67], is implemented to impose open boundaries with a pressure gradient, driving the fluid towards the outlet. In the directions perpendicular to the stream, periodic bound-

³All quantities are given in numerical units.

aries are used.

The soap film simulation depicted in Figure 5.1 is performed on a larger grid of size 512×128 with a discretization step of $\Delta = \Delta t = \Delta x^i = 0.5$, and the wires are accounted for by using no-slip boundaries, i.e. imposing zero flow velocity in the equilibrium distribution at the wire positions. The out-of-plane curvature of the soap film is modeled by a Gaussian perturbation of amplitude $a_0 = 15$ and width $r_0 = 28$, and the flow is driven by a pressure gradient of $\nabla P = 9.2 \times 10^{-10}$. The vorticity field is measured with a finite difference method at time $t = 1800$. The colorbar is taken from Ref. [68] and corresponds to the real thickness-dependent colors of a soap film with refraction index $n = 1.33$, illuminated by white daylight (“Illuminant D65”).

The real soap film in Figure 5.1 has been experimentally created by spanning a film, made of a commercial soap bubble solution, between two parallel vertical wires like in Ref. [17]. The flowing soap film is driven by gravity, and an out-of-plane curvature can be achieved by applying a bundled air flow normal to the film surface. In principle, out-of-plane curvature can also be achieved by applying an electrostatic field (e.g. by a charged balloon) or by bending the confining wires.

5.3 Dissipation induced by curvature

5.3.1 Flow past a deformation of space

In order to gain a deeper understanding of the underlying process, we consider a two-dimensional surface with a smooth deformation, as illustrated in Figure 5.2. The spatial deformation is described by a Gaussian perturbation of the metric tensor:

$$g_{ij} = (1 + \delta g) \delta_{ij}, \quad \text{with} \quad \delta g(r) = -a_0 \exp\left(-\frac{r^2}{2r_0^2}\right), \quad (5.1)$$

where $r = \|\vec{r} - \vec{r}_c\|$ parametrizes the distance from the center position \vec{r}_c of the perturbation, a_0 denotes the amplitude and r_0 the width of the perturbation. The corresponding curvature field can be quantified by the Ricci

5.3. DISSIPATION INDUCED BY CURVATURE

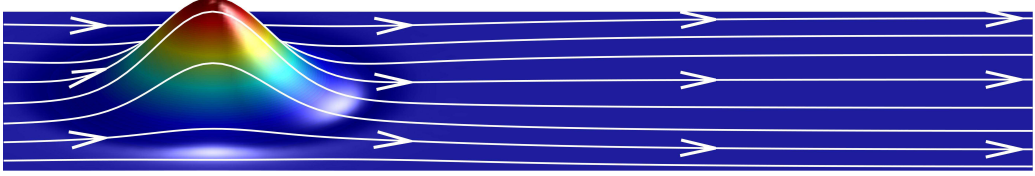


Figure 5.2: **Surface with a Gaussian-shaped deformation..** The colors correspond to the strength of the metric perturbation, from flat space (blue) to high deformation (red), and the white lines illustrate the flow streamlines of a fluid simulation.

scalar, which for this metric tensor is given by

$$R(r) = \frac{(2r_0^2(1 + \delta g(r)) - r^2)\delta g(r)}{r_0^4(1 + \delta g(r))^3}.$$

The upper plot of Figure 5.3 depicts the Ricci scalar for a metric perturbation of amplitude $a_0 = -0.1$ and width $r_0 = 6$, showing that the curvature field is positive (convex) around the center of the perturbation, thus causing an attractive inertial force field. This becomes evident when considering the geodesic lines $\gamma(t)$, starting parallelly at the inlet $x = 0$ with velocity v_0 along the x -direction. The geodesics can be calculated numerically from the geodesic equation,

$$(\nabla_{\dot{\gamma}(t)}\dot{\gamma}(t))^i = \ddot{\gamma}^i(t) + \Gamma_{jk}^i \dot{\gamma}^j(t) \dot{\gamma}^k(t) = 0,$$

by using a simple Euler integration scheme with initial conditions $\gamma(0) = (0, y_0)$, $\dot{\gamma}(0) = (v_0, 0)$. The resulting geodesic lines are depicted in the upper plot of Figure 5.3, showing that the geodesics are indeed focused towards the center by the attractive force field of the curvature source.

In the corresponding fluid simulation, the flow is driven past the metric perturbation by a pressure gradient of $|\nabla P| = 5.8 \times 10^{-9}$ in x -direction. Interestingly, we observe that the flow, interacting with the curvature source, converges to a stationary equilibrium state after sufficient time, even though we consider an open system in which the fluid is continuously driven by the constant pressure drop. The convergence to the stationary state can be quantified by plotting the flux $\Phi = \frac{1}{S} \int_S \rho u^x \sqrt{g} dy$, evaluated on an arbitrary channel cross-section S , as function of time, as depicted in Figure 5.4.

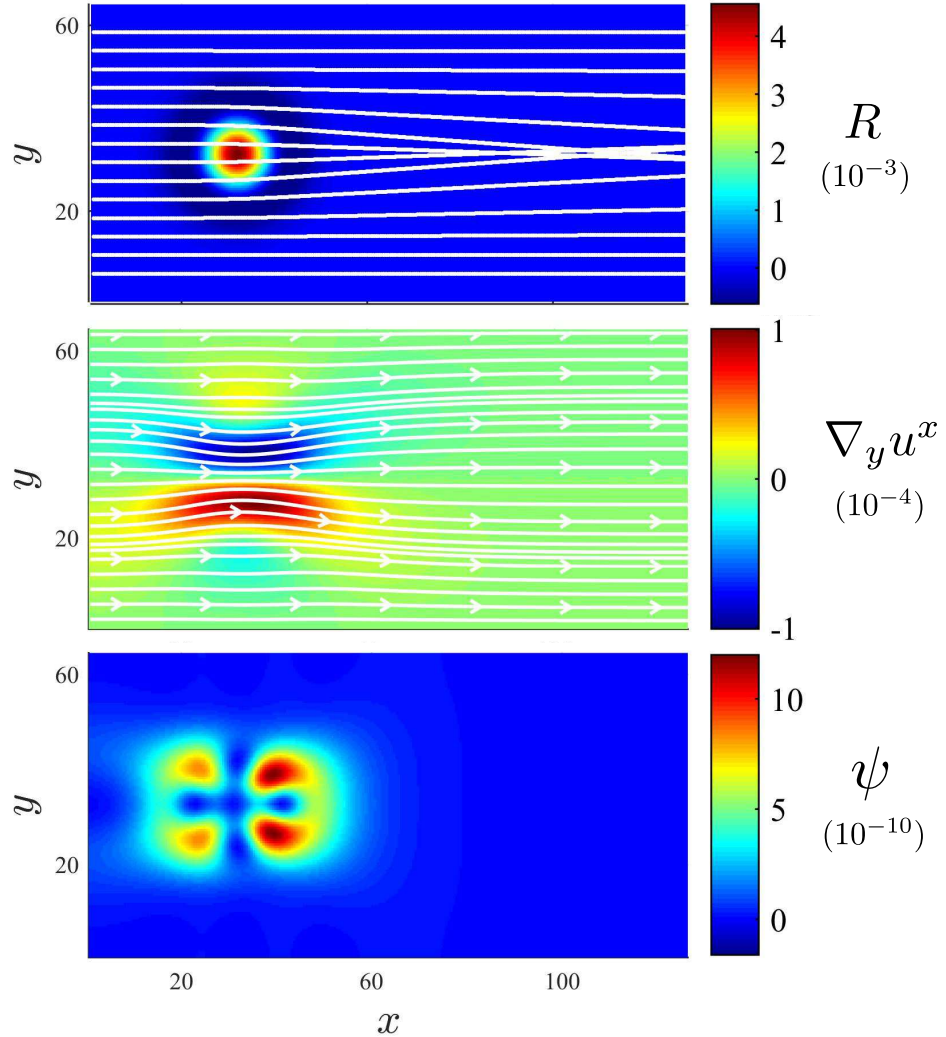


Figure 5.3: **Flow past a spatial deformation.** Simulation results for a centered metric perturbation of amplitude $a_0 = -0.1$ and width $r_0 = 6$. *Upper plot:* The colors depict the Ricci curvature scalar R , measuring the strength of the spatial deformation. The white lines represent the geodesic lines, originating parallelly from the inlet. *Middle plot:* The white lines denote the velocity streamlines of the flow, while the colors correspond to the gradient of the velocity field, $\nabla_y u^x$, forming the main component of the dissipation function $\psi \sim \nu \|\nabla u\|_g^2$. *Lower plot:* The colors represent the local energy dissipation function ψ in the stationary state. The dissipative effect around the curvature source is clearly visible.

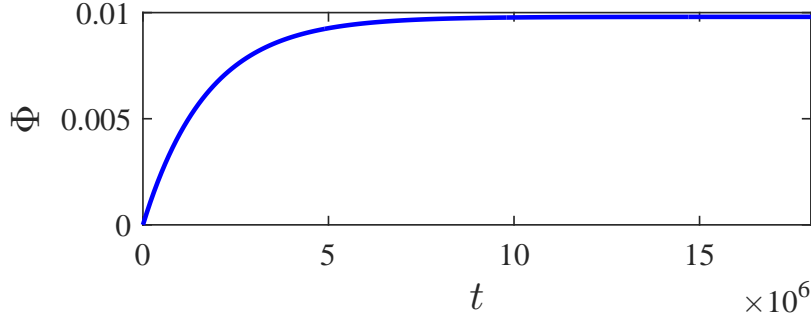


Figure 5.4: **Convergence of the flux to a stationary state.** The average flux Φ is depicted as function of time for a simulation of flow past a spatial deformation of amplitude $a_0 = -0.1$ and width $r_0 = 6$. As can be seen, the flux converges to a constant value as the flow equilibrates to a stationary state.

As can be seen, the flux indeed converges to a stationary state, which we characterize numerically by the criterion $|\Phi(t) - \Phi(t - 10^5)|/|\Phi(t)| < 10^{-6}$. The corresponding velocity streamlines in the stationary state are illustrated in the middle plot of Figure 5.3. We observe that the streamlines are narrowed next to the metric perturbation, thus introducing velocity gradients $\nabla_i u_j$ between adjacent fluid layers, as depicted by the colors. The deviation of the velocity streamlines from the geodesic lines in the upper plot might be explained by the fact that geodesics only represent the trajectories of non-interacting free particles, while in a viscous fluid the flow is also affected by collisions between particles. Macroscopically, the collisions manifest themselves as viscous stresses within the flow, resulting in the shear and distortion of the flow streamlines. These viscous stresses are quantified by the viscous stress tensor

$$\sigma^{ij} = \nu (\nabla^i(\rho u^j) + \nabla^j(\rho u^i) + g^{ij}\nabla_k(\rho u^k)),$$

where ν , the kinematic viscosity of the fluid, scales with the mean free path and thus with the average time between consecutive collisions. In the Navier-Stokes momentum equation, the viscous stresses appear as a forcing term, $\nabla_j \sigma^{ij} \sim \nu \nabla_j \nabla^i(\rho u^i)$, which directly affects the momentum of the fluid:

$$\rho D_t u^i = -\nabla^i P + \nabla_j \sigma^{ij}, \quad (5.2)$$

where D_t denotes the material derivative. This explains the convergence of the flow to a steady state, since the viscous forces oppose the pressure drop $\nabla^i P$ and thus lead to a global equilibration of the fluid. Indeed, the viscous forces are directly related to the curvature of space, since

$$\begin{aligned}\nabla_j \sigma_i{}^j &= \nu (\nabla_j \nabla_i (\rho u^j) + \nabla_j \nabla^j (\rho u_i) + \nabla_i \nabla_j (\rho u^j)) \\ &= \nu (R_{ij} \rho u^j + \Delta_g (\rho u_i) + 2 \nabla_i \nabla_j (\rho u^j)),\end{aligned}$$

where R_{ij} denotes the Ricci tensor⁴, and $\Delta_g = \nabla^2$ the Laplacian on manifolds.

The curvature-induced viscous stresses cause a space-dependent loss of kinetic energy, as can be shown by computing the rate of the local energy density,

$$\frac{1}{2} \rho D_t \|u\|_g^2 = \rho u_i D_t u^i = -u_i \nabla^i P + \nabla_i (u_j \sigma^{ij}) - (\nabla_i u_j) \sigma^{ij},$$

where the first term on the right-hand side denotes the compression work, the second term the shear work and the last term the distortion work of the fluid. The total energy dissipation rate is obtained by integrating the energy density over space, which yields

$$D_t E_{\text{kin}} = \frac{1}{2} \int_V \rho D_t \|u\|_g^2 \sqrt{g} d^2x = - \int_V (\nabla_i u_j) \sigma^{ij} \sqrt{g} d^2x = - \int_V \psi \sqrt{g} d^2x,$$

where the contributions from the compression and shear work vanish due to the Gauss' divergence theorem, and we have defined the local dissipation function by $\psi = (\nabla_i u_j) \sigma^{ij} \sim \nu \|\nabla u\|_g^2$. Since the dissipation function is positive-definite, the total kinetic energy of the fluid changes with a negative rate and is thus irreversibly dissipated from the system. The lower plot in Figure 5.3 depicts the dissipation function ψ , showing a visible increase of local energy loss around the curvature source. Interestingly, the shape of ψ resembles the quadrupole pattern of the vorticity field in Figure 5.1.

In order to characterize the flow in terms of a Reynolds number, we define a characteristic length by the effective diameter of the metric perturbations,

⁴Here, we have used a property of the Ricci tensor, $R_{ij} v^j = (\nabla_j \nabla_i - \nabla_i \nabla_j) v^j$.

$d = 2r_0$. Accordingly, the Reynolds number can be defined as $Re = \Phi d/\mu$, where Φ denotes the flux and μ the dynamic viscosity. For the simulation depicted in Figure 5.3, the Reynolds number is about $Re \approx 0.6$, and the flow is still in the laminar regime.

5.3.2 Curvature-induced dissipation in soap films

To highlight the potential impact of our results, we can think of an experiment on soap films, which can effectively be described by the two-dimensional Navier-Stokes equations. We assume a soap film as used in Ref. [17, 19], consisting of a soap-water solution with mass density $\rho^{3D} \approx 1\text{g/cm}^3$ and effective 2D dynamic viscosity $\mu^{2D} \approx 10^{-9}\text{Pa m s}$ [19]. For a soap film of width $L = 10\text{cm}$, height $h \approx 1\mu\text{m}$ [19] and a metric perturbation of range $r_0 \approx 1\text{cm}$, the effective 2D density yields $\rho^{2D} = \rho^{3D} \cdot h \approx 10^{-6}\text{g/cm}^2$. In experiments, nylon threads are used to constrain the soap film [17], which we account for by applying no-slip boundary conditions, providing an additional source of dissipation. In order to find the relative magnitude of the curvature-induced dissipation, we compare the dissipation in a flat soap film to the dissipation in a curved film, finding that the average dissipation increases by about 1% from $\langle \psi_0 \rangle = (6.348 \pm 0.002) \cdot 10^{-8}\text{J/s m}^2$ (flat film) to $\langle \psi \rangle = (6.392 \pm 0.002) \cdot 10^{-8}\text{J/s m}^2$ (curved film). Note that this increase is significantly beyond the numerical error, being of order 0.03%. This might seem a small correction, but it grows significantly with the number and strength of the metric perturbations, thus leading to non-negligible effects. For a system with 16 randomly arranged metric perturbations, for example, the dissipation increases to about 12%.

5.4 Transport law for general geometries

While in a soap film experiment, the flow is strongly affected by the confining wires, adding a significant source of dissipation to the flow, we are able to study curvature-induced dissipation in open systems without boundaries by using numerical simulations. Figure 5.5 depicts the flow through an open

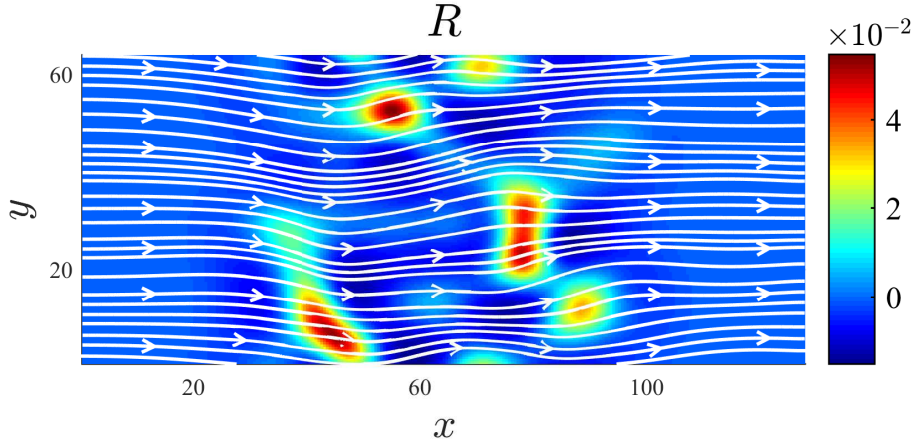


Figure 5.5: **Flow past a randomly curved medium.** The Ricci curvature scalar R for an open system with 16 randomly arranged metric perturbations of amplitude $a_0 = 0.1$ and width $r_0 = 6$. The colors illustrate the strength of the curvature, and the white lines represent the streamlines of the flow, bent by the curvature.

system with 16 randomly arranged, Gaussian-shaped metric perturbations of amplitude $a_0 = 0.1$ and width $r_0 = 6$. The colors correspond to the Ricci scalar, measuring the local strength of the curvature, and the white lines represent the streamlines of the flow, driven by a pressure gradient of $|\nabla P| = 5.8 \times 10^{-6}$ with a kinematic viscosity of $\nu = 0.185$ (in numerical units). As can be seen, the flow streamlines are bent only by the intrinsic curvature, since there are no other external influences to the flow.

A notable observation is made by plotting the pressure gradient, $|\nabla P|$, as function of the total mass flow Φ , as depicted in Figure 5.6 for a curved medium with 16 metric perturbations (amplitude $a_0 = 0.1$, width $r_0 = 4$). As can be seen, for $\Phi \lesssim 0.04$, there is a linear correlation between $|\nabla P|$ and Φ , where the flow is governed by the terms linear in the velocity in the Navier-Stokes equation (5.2), i.e. from the curvature-induced viscous forces, $\nabla_j \sigma^{ij}$, originating from the viscous stress tensor and thus from the shear $\nabla_j u^i$ induced between adjacent fluid layers. For stronger mass flows, $\Phi \gtrsim 0.04$, the transport law in Figure 5.6 requires a non-linear correction,

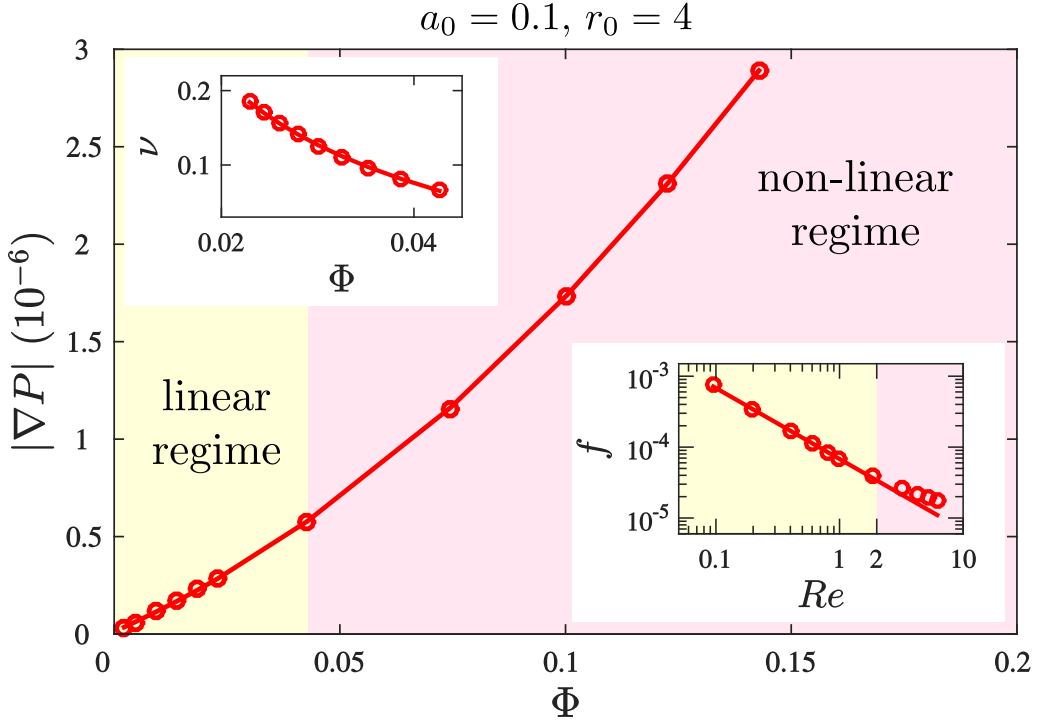


Figure 5.6: **Transport law for a curved medium with 16 metric perturbations.** The solid line in the main plot represents a fit with respect to the non-linear transport law, $|\nabla P| = \alpha\nu\Phi + \beta\Phi^2$ for $\alpha = (5.8 \pm 0.2) \times 10^{-5}$ and $\beta = (6.6 \pm 0.3) \times 10^{-5}$. *Upper inset:* Flux Φ as function of viscosity ν at constant pressure drop $|\nabla P| = 2.9 \times 10^{-7}$. The solid line represents a fit using Eq. (5.3), obtaining $\alpha = (6.01 \pm 0.06) \times 10^{-5}$ and $\beta = (6.7 \pm 0.3) \times 10^{-5}$, in agreement with the fitting values found above. *Lower inset:* Friction factor $f = |\nabla P|/\Phi^2d$ as function of the Reynolds number $Re = \Phi d/\mu$. The departure from linear transport law at $Re \approx 2$ is visible.

originating from the terms quadratic in the velocity $\sim \rho u^j \nabla_j u^i$ in Eq. (5.2). In this regime, the quadratic inertial forces $\sim \Gamma_{jk}^i \rho u^j u^k$ begin to dominate over the viscous forces, causing a break down of the linear law. This becomes even clearer when plotting the ratio between the shear stress and the kinetic energy, expressed by the friction factor $f = |\nabla P|/\Phi^2d$, as function of the Reynolds number $Re = 2r_0\Phi/\nu$, as depicted in the lower inset of Figure 5.6. We observe a linear power law, $f = \alpha/Re$, for small Reynolds numbers,

$Re \lesssim 2$, where the flow is dominated by viscous shear forces, while for higher Reynolds numbers, $Re \gtrsim 2$, the quadratic terms induce non-linear corrections. Finally, the upper inset of Figure 5.6 depicts the dependence of the flux on the viscosity, measured at constant pressure drop, finding an anti-correlation between Φ and ν . All these results can be summarized in the following transport law, describing both the linear regime and the non-linear effects:

$$|\nabla P| = \alpha\nu\Phi + \beta\Phi^2, \quad (5.3)$$

where α and β are parameters, which can be interpreted as reciprocal permeabilities, and ν denotes the kinematic viscosity.

Interestingly, Eq. (5.3) is similar to the Darcy-Forchheimer's law for porous media [69, 3], where the dissipation originates from the interaction of the flow with solid obstacles. However, there are major physical differences regarding the underlying mechanisms in the two types of media. In a porous medium, the obstacles are impermeable solid structures, while the fluid motion is governed by the Navier-Stokes equation in flat space. In a curved medium, however, the background space itself is curved, inducing viscous stresses and thus dissipation. Furthermore, since the metric perturbations are permeable to the fluid, the flow typically does not form sharp channel-like paths as in a porous medium.

In order to formulate a transport law for general geometries, we study the dependence of the coefficients α and β on the parameters of the curved space. We have performed simulations for a wide range of metric parameters by varying the amplitude a_0 , the range r_0 and the number density $n = N/V$ of the metric perturbations, where V denotes the volume of the curved space. We observe that all the data collapse onto a single common curve when plotting α and β as function of the non-dimensionalized average metric perturbation $K = a_0 n(\varepsilon^2 - \varepsilon_0^2)$, where $\varepsilon = r_0/\lambda$ denotes the non-dimensionalized perturbation range, normalized by the characteristic distance between the perturbations, $\lambda = \sqrt{V/N}$, and $\varepsilon_0 \approx 1.3$. The resulting curves are depicted in Figure 5.7, showing a linear increase of α and β with the average metric perturbation K , where the solid lines represent

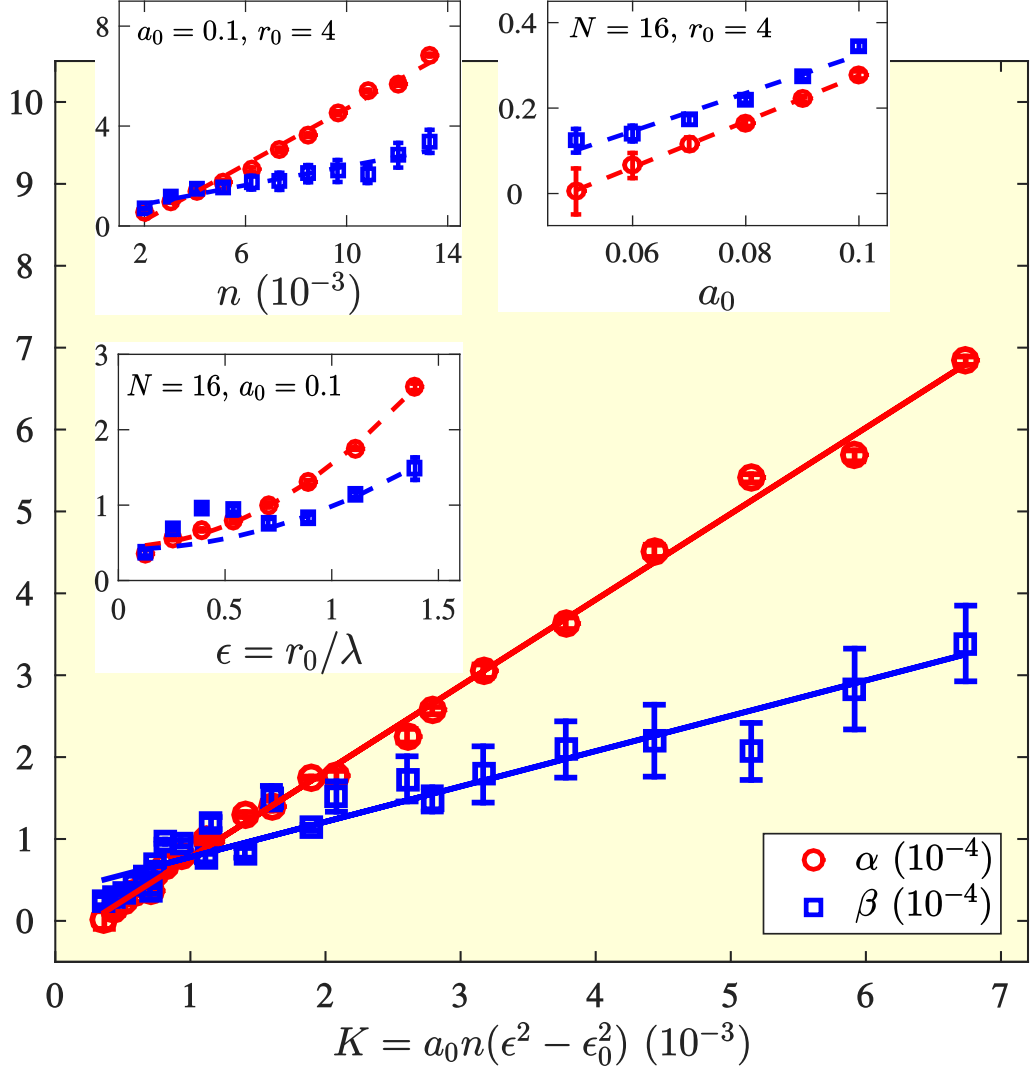


Figure 5.7: **Dependence of the reciprocal permeabilities α and β on the geometry.** *Insets:* α and β as function of the amplitude a_0 , dimensionless range $\varepsilon = r_0/\lambda$ and number density $n = N/V$ of the metric perturbations. *Main plot:* Data collapse when plotting α and β as function of the dimensionless average metric perturbation $K = a_0 n (\varepsilon^2 - \varepsilon_0^2)$ for $\varepsilon_0 \approx 1.3$. In all plots, the error bars originate from fitting the non-linear transport law, $|\nabla P| = \alpha \nu \Phi + \beta \Phi^2$, to our data.

linear fits (see Table 5.1 for the fitting coefficients). Consequently, the permeability of the medium decreases with increasing strength of the metric perturbation. Accordingly, the permeability $\kappa = \alpha^{-1}$ as well as the inertial permeability $\kappa_1 = \beta^{-1}$ decrease with the average strength of the metric perturbation. This behavior agrees with our expectation, since the stronger the metric perturbations in the medium, the larger the effective resistance against the flow will be.

$\alpha(n)$	$=$	$(5.6 \pm 0.5) \times 10^{-2}n - (8.9 \pm 3.9) \times 10^{-5}$
$\beta(n)$	$=$	$(1.9 \pm 0.4) \times 10^{-2}n - (5.0 \pm 3.8) \times 10^{-5}$
$\alpha(a_0)$	$=$	$(1.07 \pm 0.04) \times 10^{-3}a_0 - (5.2 \pm 0.3) \times 10^{-5}$
$\beta(a_0)$	$=$	$(8.9 \pm 2.6) \times 10^{-4}a_0 - (2.4 \pm 2.0) \times 10^{-5}$
$\alpha(\epsilon)$	$=$	$(1.1 \pm 0.8) \times 10^{-4}\epsilon^2 - (4.5 \pm 0.7) \times 10^{-5}$
$\beta(\epsilon)$	$=$	$(5.7 \pm 1.3) \times 10^{-5}\epsilon^2 - (4.1 \pm 1.4) \times 10^{-5}$
$\alpha(K)$	$=$	$(1.05 \pm 0.03) \times 10^{-1}K - (2.8 \pm 0.8) \times 10^{-5}$
$\beta(K)$	$=$	$(4.3 \pm 0.6) \times 10^{-2}K - (3.5 \pm 1.6) \times 10^{-5}$

Table 5.1: **Fitting functions for the reciprocal permeabilities α and β .** n denotes the density, a_0 the amplitude and ϵ the dimensionless range of the metric perturbations. K denotes the dimensionless average metric perturbation.

5.5 Method validation

To prove the physicality of our LB simulations, we have performed a finite resolution study. To this end, we have measured the transport law, $|\nabla P| = \alpha\nu\Phi + \beta\Phi^2$, for a curved medium with 16 metric perturbations ($a_0 = 0.1$, $r_0 = 4$) for different grid resolutions Δ^{-1} , as depicted in Figure 5.8. As can be seen, the distance between the curves decreases rapidly with increasing resolution, which can be quantified by the relative L^2 -difference (cf. Chapter 4, Eq. (4.16)), being less than 1% between the dashed ($\Delta = \frac{1}{2}$) and solid ($\Delta = \frac{1}{4}$) curve. Furthermore, we measured the finite resolution effects on the average dissipation, $\langle\psi\rangle = \frac{1}{V} \int \psi dV$, for a single metric perturbation of amplitude $a_0 = -0.1$ and width $r_0 = 6$. In the inset of Figure 5.8,

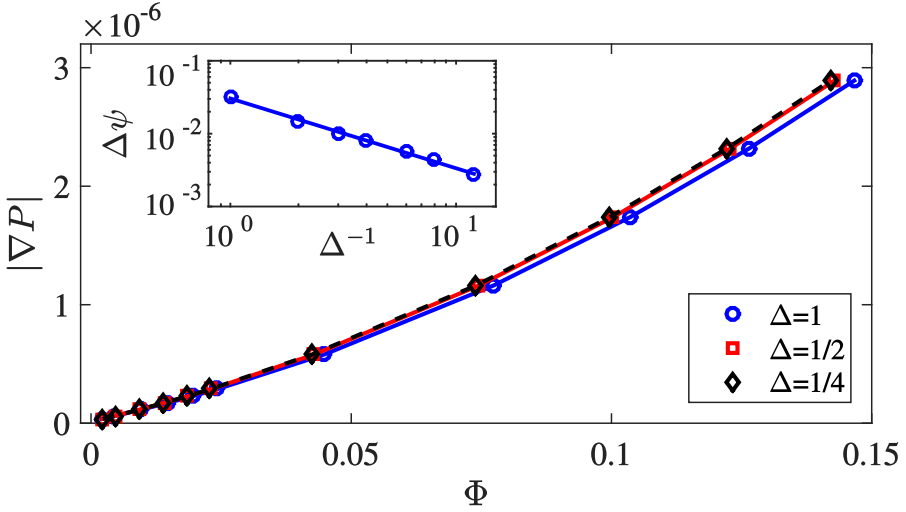


Figure 5.8: **Dependence of the simulation results on the grid resolution.** The nonlinear transport law, Eq. (5.3), is measured for different grid spacings Δ for a curved medium with 16 metric perturbations ($a_0 = 0.1$, $r_0 = 4$). As can be seen, the curves converge with increasing grid resolution $\sim \Delta^{-1}$. *Inset:* Log-log plot of the relative error of the total dissipation function, $\Delta\psi$, as function of the grid resolution Δ^{-1} for a single metric perturbation ($a_0 = -0.1$, $r_0 = 6$). For $\Delta = \frac{1}{2}$, as used for all simulations in this chapter, the error falls below 1%.

the relative error $\Delta\psi = |\langle\psi\rangle - \langle\psi\rangle_\infty|/\langle\psi\rangle_\infty$ is depicted as function of the resolution Δ^{-1} , where $\langle\psi\rangle_\infty = (2.991 \pm 0.002) \times 10^{-9}$ has been determined by extrapolation. As can be seen, the error decreases rapidly with the grid resolution, falling below 1% for $\Delta^{-1} \geq 2$. Altogether, this shows that our simulation results are not appreciably affected by finite resolution effects (up to an error of about 1% for $\Delta = \frac{1}{2}$).

We also have checked that our simulation results are not constrained by the positions of the inlet and outlet. To this end, we have performed additional simulations, putting inlet and outlet twice as far from the metric perturbations. We observed that our simulation results do not change with the inlet and outlet positions (if they are sufficiently apart as in all the simulations presented in the paper).

5.6 Summary

A fundamental physical process inherent to fluid dynamics in curved space has been presented in this chapter, namely curvature-induced dissipation. We have shown that local sources of curvature generate viscous stresses, which tend to narrow or widen the streamlines and thus introduce velocity gradients between adjacent fluid layers, leading to an irreversible dissipation of energy, induced by the spatial curvature. In order to demonstrate the far-reaching consequences of curvature-induced dissipation, we have studied media with various randomly-distributed curvature sources. We have observed that the flow converges to a stationary equilibrium state solely due to curvature-induced dissipation. As a consequence, the flow has been found to satisfy a non-linear transport law, $|\nabla P| = \alpha\nu\Phi + \beta\Phi^2$, where the viscous forces are induced by the spatial curvature in the system. We have further shown that the reciprocal permeabilities α and β are linearly correlated with the average metric perturbation in the medium.

Chapter 6

Quantum lattice Boltzmann in curved space

6.1 Introduction

In this chapter, we study the Dirac equation in flat and curved spaces numerically by using the quantum lattice Boltzmann (QLB) algorithm, which has been developed during the last decade to simulate Dirac fermions in flat space [4, 47, 48]. In this work, we extend the QLB method to curved spaces, allowing us to study quantum field theory on manifolds. We validate our method on the basis of different analytical solutions of the Dirac equation in both flat and curved space, finding perfect agreement between simulation and theory.

As an application of the QLB method on manifolds, we investigate the electronic properties of curved graphene sheets. Graphene is one of the most widely studied materials of the last decades due to its extraordinary mechanical, electronic and optical properties [35, 36, 37]. It consists of a monolayer of carbon atoms, arranged on a honeycomb crystal structure as illustrated in Figure 6.1. The electronic band structure of graphene is well-described by the tight-binding Hamiltonian, approximating the electronic

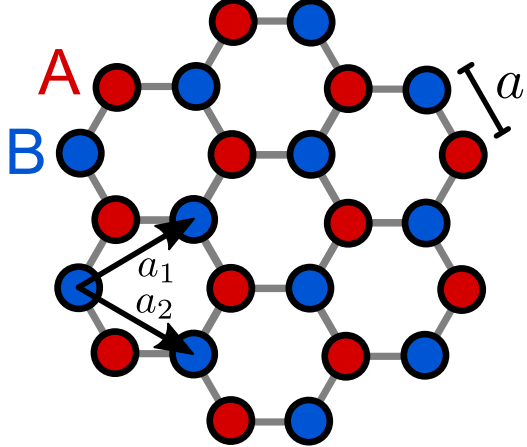


Figure 6.1: **Graphene lattice.** The graphene atoms form a honeycomb lattice structure, consisting of two triangular Bravais sublattices A and B , generated by the lattice unit vectors a_1 and a_2 . In an ideal graphene sheet, the atoms are uniformly separated by the lattice spacing a .

system by a superposition of local wave functions for isolated atoms [37]:

$$H_{t.b.} = -t \sum_{\langle i,j \rangle, \sigma} (a_{\sigma,i}^\dagger b_{\sigma,j} + H.c.) - t' \sum_{\langle\langle i,j \rangle\rangle, \sigma} (a_{\sigma,i}^\dagger a_{\sigma,j} + b_{\sigma,i}^\dagger b_{\sigma,j} + H.c.), \quad (6.1)$$

where $a_{\sigma,i}$ and $a_{\sigma,i}^\dagger$ denote the annihilation and creation operators for electrons with spin $\sigma = \pm \frac{1}{2}$ on sublattice A , while $b_{\sigma,i}$ and $b_{\sigma,i}^\dagger$ correspond to electrons on sublattice B , respectively. The sums run over all pairs of nearest-neighbors $\langle i,j \rangle$ or next nearest-neighbors $\langle\langle i,j \rangle\rangle$, respectively, and $H.c.$ denotes the Hermitian conjugate. As can be seen, the first term in the Hamiltonian describes the hopping of electrons from sublattice A to sublattice B (and vice versa) with hopping energy t , while the second term corresponds to hopping within the same sublattice with hopping energy t' . Here and in the following, we work in natural units by measuring all quantities in units of the universal constants such as the speed of light c (for graphene: the Fermi speed v_F), the Planck constant \hbar , the electron charge e and the electron mass m_e .

Interestingly, it can be shown that for the low-energetic electronic states, the tight-binding Hamiltonian (6.1) converges into an effective Dirac Hamil-

6.1. INTRODUCTION

tonian for massless particles in the continuum limit [36, 37]. The latter is given by

$$H_D = -iv_F \int \Psi^\dagger \gamma^0 \gamma^i \partial_i \Psi d^2x, \quad (6.2)$$

where Ψ denotes the Dirac spinor and γ^μ the Dirac matrices, given by

$$\gamma^0 = \begin{pmatrix} 1 & 0 & 0 & 0 \\ 0 & 1 & 0 & 0 \\ 0 & 0 & -1 & 0 \\ 0 & 0 & 0 & -1 \end{pmatrix}, \quad \gamma^1 = \begin{pmatrix} 0 & 0 & 0 & 1 \\ 0 & 0 & 1 & 0 \\ 0 & -1 & 0 & 0 \\ -1 & 0 & 0 & 0 \end{pmatrix}, \quad \gamma^2 = \begin{pmatrix} 0 & 0 & 0 & -i \\ 0 & 0 & i & 0 \\ 0 & i & 0 & 0 \\ -i & 0 & 0 & 0 \end{pmatrix}, \quad \gamma^3 = \begin{pmatrix} 0 & 0 & 1 & 0 \\ 0 & 0 & 0 & -1 \\ -1 & 0 & 0 & 0 \\ 0 & 1 & 0 & 0 \end{pmatrix}. \quad (6.3)$$

Furthermore, the Fermi velocity is given by $v_F = \frac{3}{2}ta$, where t denotes the hopping energy and a the lattice spacing. The Dirac spinor $\Psi = (\Psi_A^+, \Psi_B^+, \Psi_A^-, \Psi_B^-)$ describes electrons (positive-energy solutions, +) and holes (negative-energy solutions, -) on the two sublattices A and B , which are interpreted as a “pseudo-spin”, $\sigma = (A, B)$. By using the Dirac formalism as an effective theory for the study of electron transport in graphene, the complexity of the problem is considerably reduced.

Real graphene sheets are not perfectly flat, but instead possess out-of-plane deformations (ripples) [43, 42]. As described in the following sections, these ripples are naturally taken into account by the Dirac Hamiltonian in curved space, being a generalization of the Hamiltonian mentioned above to curved manifolds [70]. For graphene under nonuniform strain, the Dirac Hamiltonian is slightly modified due to the strain-induced shift of the Dirac points [6]. In this work, we implement this correction by using an effective metric tensor in order to recover the correct effective Hamiltonian derived in Ref. [6]. Thus, we show that also nonuniformly strained graphene can be described by the original Dirac formalism in curved spacetime and validate our model on rippled graphene, for which we correctly recover the space-dependent Fermi velocity and the inhomogeneous carrier density mentioned in Refs. [71, 5, 6]. We then proceed with the study of rippled graphene in a magnetic field, finding discrete energy levels: the Landau levels. Interestingly, we observe that the Landau levels are shifted due to the curvature of the graphene sheet. We characterize this shift in terms of the average spatial deformation.

6.2 The Dirac equation in curved space

The Dirac equation in a curved $(D + 1)$ -dimensional spacetime, described by a Riemann manifold with spacetime metric $g_{\mu\nu}$, reads [72]

$$i\gamma^\mu D_\mu \Psi - m\Psi = 0, \quad (6.4)$$

where Ψ denotes the spinor wave function, γ^μ the generalized, space-dependent Dirac matrices, D_μ the covariant spinor derivative, and Greek indices run from 0 to $(D + 1)$ ¹. The generalized Dirac matrices satisfy the anticommutation relation $\{\gamma^\mu, \gamma^\nu\} = 2g^{\mu\nu}\mathbb{1}$, where $g^{\mu\nu}$ denotes the inverse metric tensor. They can be constructed from the standard flat-space Dirac matrices γ^α by using the tetrad formalism [73]: $\gamma^\mu = \gamma^\alpha e_\alpha^\mu$, where the tetrad e_α^μ is a set of $(D + 1)$ basis vectors $\{e_0^\mu, e_1^\mu, \dots, e_D^\mu\}$ of the tangent space, defining an orthonormal frame with respect to the flat Minkowski metric $\eta_{\alpha\beta} = \text{diag}(+, -, \dots, -)$, i.e.

$$e_\alpha^\mu g_{\mu\nu} e_\beta^\nu = \eta_{\alpha\beta}, \quad \text{or, equivalently,} \quad g^{\mu\nu} = e_\alpha^\mu \eta^{\alpha\beta} e_\beta^\nu.$$

Thus, the tetrad can be viewed as the “square root of the metric tensor”. In two dimensions, the tetrad can be computed directly from the metric tensor:

$$e_i^a = \frac{g_{ai} + \delta_{ai}\sqrt{g}}{\sqrt{\text{Tr}(g) + 2\sqrt{g}}}, \quad (6.5)$$

where $\text{Tr}(g) = \sum_i g_{ii}$ denotes the trace, and \sqrt{g} the square root of the determinant of the metric tensor.

The covariant spinor derivative D_μ appearing in the Dirac equation (6.4) is a consistent generalization of the partial spacetime derivative ∂_μ to the spinor bundle on a manifold. Explicitly, the spinor derivative acts on the spinor Ψ as follows:

$$D_\mu \Psi = \partial_\mu \Psi + \Gamma_\mu \Psi,$$

¹Here and in the following, we use Greek indices from the first half of the alphabet (α, β, \dots) to refer to objects in flat Minkowski space (e.g. $\eta_{\alpha\beta}$), whereas Greek indices from the second half of the alphabet (μ, ν, \dots) correspond to the curved space-time (e.g. $g_{\mu\nu}$). As usual, indices are raised or lowered by contraction with the corresponding metrics, e.g. $e^{\alpha\mu} = \eta^{\alpha\beta} e_\beta^\mu$, $e_{\alpha\mu} = g_{\mu\nu} e_\alpha^\nu$, $e_\mu^\alpha = \eta^{\alpha\beta} g_{\mu\nu} e_\beta^\nu$.

6.2. THE DIRAC EQUATION IN CURVED SPACE

where Γ_μ denotes the *spin connection*, representing the connection coefficients of the spinor derivative. Explicitly, the spin connection matrices are given by

$$\Gamma_\mu = -\frac{i}{4}\omega_\mu^{\alpha\beta}\sigma_{\alpha\beta}, \quad \text{where} \quad \sigma_{\alpha\beta} = \frac{i}{2}[\gamma_\alpha, \gamma_\beta] \quad \text{and} \quad \omega_\mu^{\alpha\beta} = e_\nu^\alpha \nabla_\mu e^\nu{}^\beta. \quad (6.6)$$

Here, ∇ denotes the usual covariant derivative acting on spacetime vectors, as depicted in Eq. 2.3. In contrast to flat space, the spinor derivative also acts on the space-dependent Dirac matrices γ^μ , which can be considered as “spinor vectors”, on which the spinor derivative acts in a more general way [74]:

$$D_\mu \gamma^\nu = \partial_\mu \gamma^\nu + \Gamma_{\mu\rho}^\nu \gamma^\rho + [\Gamma_\mu, \gamma^\nu].$$

Here, $\Gamma_{\mu\rho}^\nu$ are the Christoffel symbols, defined in Eq. (2.2), and Γ_μ the spin connection matrices (6.6). In fact, it can be shown that $D_\mu \gamma^\nu = 0$ (the generalized Dirac matrices are covariantly constant) and thus $D_\mu e_a^\nu = 0$ (compatibility with the tetrad). By construction, the covariant spinor derivative satisfies the standard properties of a derivative, such as the product rule, $D_\mu(A B) = (D_\mu A)B + B(D_\mu A)$, and compatibility with Hermitian conjugation, $D_\mu(A^\dagger) = (D_\mu A)^\dagger$ [75].

An important property of the Dirac equation is the conservation of probability, which is expressed by the conservation equation $\nabla_\mu J^\mu = 0$, where the Dirac current is defined by $J^\mu = \bar{\Psi} \gamma^\mu \Psi \in \mathbb{R}$, and $\bar{\Psi} := \Psi^\dagger \gamma^0$.

In the following, we consider a static spacetime metric of the shape

$$g_{\mu\nu} = \begin{pmatrix} 1 & 0 \\ 0 & -g_{ij} \end{pmatrix},$$

neglecting the curvature of time, where Latin indices run only over the spatial directions 1 to D^2 . Under these assumptions, the Dirac equation can be written as

$$i\gamma^0 \partial_t \Psi + i\gamma^a e_a^i D_i \Psi = m\Psi, \quad (6.7)$$

²Analogously to before, we use Latin indices from the first half of the alphabeth (a, b, c, \dots) to label Minkowski space objects, whereas Latin indices from the second half of the alphabeth (i, j, k, \dots) label tensors in curved space. For example, $\gamma^i = \gamma^a e_a^i$.

where $D_i\Psi = \partial_i\Psi + \Gamma_i\Psi = \partial_i\Psi - \frac{i}{4}\omega_i^{ab}\sigma_{ab}\Psi$, such that the probability conservation equation simplifies to

$$\partial_t\rho + \nabla_i J^i = 0,$$

where $\rho = \Psi^\dagger\Psi$ denotes the probability density and $J^i = \bar{\Psi}\gamma^i\Psi$ the probability current. The corresponding conserved quantity is the total probability

$$\mathcal{P} = \int \rho \sqrt{g} d^Dx = \int \Psi^\dagger\Psi \sqrt{g} d^Dx. \quad (6.8)$$

Furthermore, the Dirac equation conserves energy and momentum, which can be derived from the energy-momentum tensor

$$T^{\mu\nu} = i\bar{\Psi}\gamma^\mu D^\nu\Psi, \quad \text{satisfying} \quad \nabla_\mu T^{\mu\nu} = 0.$$

For the static spacetime metric introduced above, the energy and momentum density, ε and π^i , together with their corresponding conserved quantities, the total energy E and total momentum p^i , are given by

$$\varepsilon = T^{00} = i\bar{\Psi}\gamma^0\partial_t\Psi \implies E = \int \varepsilon \sqrt{g} d^Dx, \quad (6.9)$$

$$\pi^i = T^{i0} = i\bar{\Psi}\gamma^i\partial_t\Psi \implies p^i = \int \pi^i \sqrt{g} d^Dx. \quad (6.10)$$

An external vector potential $A_i(x)$, representing for example a magnetic field, can be added to the Dirac equation by minimal coupling, replacing $D_i \rightarrow (D_i - iA_i)$. On the other hand, scalar potentials $V(x)$, representing for example electric fields, can be introduced in the Dirac equation (6.7) in three different ways as discussed in Ref. [76]: Firstly, as the zeroth component of a four-vector potential A_μ , secondly, as a scalar term $\sim V(x)\Psi$, or, thirdly, as a pseudoscalar term $\sim \gamma^0\gamma^a\gamma^0V(x)$. In this work, we will use the second approach, the scalar term, which is best suited for our simulations of the relativistic quantum harmonic oscillator. In particular, the scalar term is the only implementation leading to an infinite set of bound states with discrete and equally spaced energy eigenvalues (in analogy to the non-relativistic harmonic oscillator solution of Schrödinger's equation)³.

³In general, the four-vector potential and the pseudovector potential fail to produce bound states with equally-spaced energy eigenvalues, as discussed in Ref. [76], and are thus unsuitable for our purposes.

Summarizing, the Dirac equation with external potentials $A_i(x)$ and $V(x)$ becomes

$$i\gamma^0\partial_t\Psi + i\gamma^a e_a^i(D_i - iA_i)\Psi = (m - V)\Psi. \quad (6.11)$$

6.3 Quantum lattice Boltzmann method

A recently developed method to numerically solve the Dirac equation (in flat space) is the quantum lattice Boltzmann (QLB) method, which exploits the strong conceptual similarities between the Dirac equation and the Boltzmann equation [4, 47, 48]. Here, we review the QLB algorithm proposed in Ref. [48] and generalize the method to arbitrarily curved spaces by lifting the wave function onto a general manifold, characterized by a static Riemann metric g_{ij} . This requires the introduction of a generalized covariant spinor derivative as well as generalized Dirac matrices, as discussed in the previous section, to take into account curvature effects on the manifold. Here, we present the QLB method for a three-dimensional manifold, however, the method can be applied straightforwardly to lower-dimensional manifolds as well⁴.

The algorithm is based on the Dirac equation in curved space (6.7), which can be rewritten as follows:

$$\partial_t\Psi + \sigma^a\partial_a\Psi = \mathcal{C}\Psi + \mathcal{F}\Psi, \quad (6.12)$$

Here, $\Psi = (\Psi_1^+, \Psi_2^+, \Psi_1^-, \Psi_2^-) \in \mathbb{C}^4$ denotes the complex spinor and $\sigma^a := \gamma^0\gamma^a$. While the left-hand side of the Dirac equation (6.12) can be interpreted as ‘free streaming’ along complex, matrix-valued ‘velocities’ σ^i , the right-hand side contains a ‘collision term’

$$\mathcal{C} = -(im\gamma^0 + \sigma^a e_a^i \Gamma_i)$$

as well as a forcing term

$$\mathcal{F} = -\sigma^a(e_a^i - \delta_a^i)\partial_i. \quad (6.13)$$

⁴For higher-dimensional manifolds, a higher-dimensional representation of the Dirac matrices is needed.

The latter originates from the generalized Dirac matrices $\gamma^i = e_a^i \gamma^a$ and covers the curvature effects. To avoid interpolation during the streaming step, the partial derivative is distributed among an on-grid streaming part (left-hand side of the Dirac equation (6.12)) and the forcing term. In this way, we obtain a lattice-compatible streaming operator of the form $(\partial_t + v^a \partial_a)$ with integer-valued velocities v^a . The partial derivative in the forcing term (6.13), on the other hand, can be approximated by a simple finite-difference scheme on the lattice.

In order to obtain a diagonal streaming operator, the complex σ -matrices have to be diagonalized first, which yields a diagonal velocity matrix with eigenvalues $v^a = \pm 1$ [48]:

$$X_a^\dagger \sigma^a X_a = \begin{pmatrix} 1 & 0 & 0 & 0 \\ 0 & 1 & 0 & 0 \\ 0 & 0 & -1 & 0 \\ 0 & 0 & 0 & -1 \end{pmatrix} = \gamma^0 \quad \text{for } a = 1, 2, 3.$$

The corresponding unitary transformation matrices of the diagonalization are given by

$$X_1 = \frac{1}{\sqrt{2}} \begin{pmatrix} 1 & 0 & -1 & 0 \\ 0 & 1 & 0 & -1 \\ 0 & 1 & 1 & 0 \\ 1 & 0 & 1 & 0 \end{pmatrix}, \quad X_2 = \frac{1}{\sqrt{2}} \begin{pmatrix} 0 & i & 0 & 1 \\ -i & 0 & i & 0 \\ -1 & 0 & -1 & 0 \\ 0 & -1 & 0 & -i \end{pmatrix}, \quad X_3 = \frac{1}{\sqrt{2}} \begin{pmatrix} 1 & 0 & 0 & -1 \\ 0 & -1 & 1 & 0 \\ 1 & 0 & 0 & 1 \\ 0 & 1 & 1 & 0 \end{pmatrix}.$$

Since it is not possible to diagonalize all three σ -matrices simultaneously, the streaming and collision operations are performed in successive steps, using operator splitting⁵ [47]:

$$\begin{aligned} \Psi(t + \frac{1}{D} \Delta t) &= \exp(-\Delta t \sigma^1 \partial_1 + \frac{\Delta t}{D} (\mathcal{C} + \mathcal{F})) \Psi(t), \\ \Psi(t + \frac{2}{D} \Delta t) &= \exp(-\Delta t \sigma^2 \partial_2 + \frac{\Delta t}{D} (\mathcal{C} + \mathcal{F})) \Psi(t + \frac{1}{D} \Delta t), \\ \Psi(t + \Delta t) &= \exp(-\Delta t \sigma^3 \partial_3 + \frac{\Delta t}{D} (\mathcal{C} + \mathcal{F})) \Psi(t + \frac{2}{D} \Delta t). \end{aligned} \quad (6.14)$$

Each streaming step can now be diagonalized by multiplying X_a^\dagger from the left:

$$X_a^\dagger \exp(-\Delta t \sigma^a \partial_a + \frac{\Delta t}{D} (\mathcal{C} + \mathcal{F})) \Psi = \exp\left(-\Delta t \gamma^0 \partial_a + \Delta t (\tilde{\mathcal{C}}_a + \tilde{\mathcal{F}}_a)\right) \tilde{\Psi}_a \quad (6.15)$$

⁵As mentioned in Ref. [47], the operator splitting introduces an error of order $\mathcal{O}(\Delta t^2)$, since $e^{\Delta t X} \cdot e^{\Delta t Y} = e^{\Delta t(X+Y)+\frac{1}{2}\Delta t^2[X,Y]} = e^{\Delta t(X+Y)} + \mathcal{O}(\Delta t^2)$.

where we used $X_a^\dagger X_a = \mathbb{1}$, $X_a^\dagger \sigma^a X_a = \gamma^0$, and defined

$$\tilde{\Psi}_a := X_a^\dagger \Psi, \quad \tilde{\mathcal{F}}_a := \frac{1}{D} X_a^\dagger \mathcal{F} X_a, \quad \tilde{\mathcal{C}}_a := \frac{1}{D} X_a^\dagger \mathcal{C} X_a$$

for $a = 1, 2, 3$. (Note that here and in the following, a is not summed over, although it might appear repeatedly.) Now, the streaming operator $(\partial_t + \gamma^0 \partial_a)$ is indeed diagonal in each direction a . The exponential in Eq. (6.15) can be approximated by

$$\begin{aligned} & \exp \left(-\Delta t \gamma^0 \partial_a + \Delta t (\tilde{\mathcal{C}}_a + \tilde{\mathcal{F}}_a) \right) \tilde{\Psi}_a \\ &= \left(\mathbb{1} - \Delta t \gamma^0 \partial_a + \Delta t \tilde{\mathcal{F}}_a + \left(\mathbb{1} - \frac{\Delta t}{2} \tilde{\mathcal{C}}_a \right)^{-1} \left(\mathbb{1} + \frac{\Delta t}{2} \tilde{\mathcal{C}}_a \right) \right) \tilde{\Psi}_a + \mathcal{O}(\Delta t^2). \end{aligned} \quad (6.16)$$

Here, the collision operator $e^{\Delta t \tilde{\mathcal{C}}_a}$ is expanded in a unitary way to conserve the norm of the spinor exactly during each collision step [48]. Ideally, the streaming operator $e^{-\Delta t \gamma^0 \partial_a}$ as well as the forcing operator $e^{\Delta t \tilde{\mathcal{F}}_a}$ should also be expanded unitarily, however, since these terms consist of derivative operators, an expansion analogous to the collision operator does not seem to be possible, thus limiting the numerical accuracy regarding the conservation of the probability norm to order Δt^2 .

Now, we have all ingredients at hand to assemble the curved space QLB algorithm, transporting the spinor $\Psi = (\Psi_1^+, \Psi_2^+, \Psi_1^-, \Psi_2^-)$ from time t to $t + \Delta t$ on the manifold. The manifold itself is described by a chart h , defined on a linear space (as described in Section 2.1), which we discretize on a regular rectangular lattice. According to the operator splitting (6.14), the following steps are performed consecutively for each lattice direction $n_1 = (1, 0, 0)$, $n_2 = (0, 1, 0)$, $n_3 = (0, 0, 1)$, labeled by $a = 1, 2, 3$. (As before, a is never summed over, although it might occur repeatedly.)

1. Rotation. At first, the spinor is rotated by X_a in order to obtain a diagonal streaming operator:

$$\tilde{\Psi}_a(x, t) = X_a^\dagger \Psi(x, t).$$

2. Collisions and curvature effects. Second, collisions and forces are applied on the rotated spinor,

$$\tilde{\Psi}_a^*(x, t) = \left(\mathbb{1} - \frac{\Delta t}{2} \tilde{\mathcal{C}}_a \right)^{-1} \left(\mathbb{1} + \frac{\Delta t}{2} \tilde{\mathcal{C}}_a \right) \tilde{\Psi}_a(x, t) + \Delta t \tilde{\mathcal{F}}_a \tilde{\Psi}_a(x, t),$$

where $\tilde{\Psi}_a^*$ denotes an auxiliary field. The collision operator and the forcing term are given by

$$\tilde{\mathcal{C}}_a = \frac{1}{D} X_a^\dagger \mathcal{C} X_a = -\frac{i}{D} m (X_a^\dagger \gamma^0 X_a) - \gamma^0 e_a^i \Gamma_i, \quad (6.17)$$

and

$$\tilde{\mathcal{F}}_a \tilde{\Psi}_a(x, t) = \sum_{i=1}^D (e_a^i - \delta_a^i) \left(\tilde{\Psi}_a(x \mp n_i \Delta t, t) - \tilde{\Psi}_a(x, t) \right), \quad (6.18)$$

respectively. Here and in the following, the upper sign of the plus-minus operator applies for the spin-up components (Ψ_1^+, Ψ_2^+) , and the lower sign for the spin-down components (Ψ_1^-, Ψ_2^-) .

3. Streaming. Third, the spinor components stream to the neighboring grid points along the lattice directions $\pm n_a$:

$$\tilde{\Psi}_a(x, t + \frac{\Delta t}{D}) = \tilde{\Psi}_a^*(x \mp n_a \Delta t, t).$$

4. Inverse Rotation. Fourth, the spinor is rotated back by X_a :

$$\Psi(x, t + \frac{\Delta t}{D}) = X_a \tilde{\Psi}_a(x, t + \frac{\Delta t}{D}).$$

5. Continue with step 1 for the next spatial direction $(a + 1)$.

External potentials, such as a scalar potential $V(x)$ or a vector potential $A_i(x)$, can be introduced straightforwardly into the algorithm by adding the potentials to the collision operator in Eq. (6.17) in the following way:

$$\tilde{\mathcal{C}}_a = -\frac{i}{D} (m - V)(X_a^\dagger \gamma^0 X_a) - \gamma^0 e_a^i (\Gamma_i - iA_i).$$

6.4 Method validation

In the following subsections, we validate the QLB on manifolds on different benchmark examples, such as free quantum particles, the quantum harmonic oscillator, and plane waves in curved spaces.

6.4.1 Free quantum particle

As a first validation example, following Ref. [47], we consider the free-particle solution of the Schrödinger equation in two-dimensional flat space⁶, given by

$$i\partial_t \phi = \frac{1}{2m} \Delta \phi.$$

A free particle is represented by a Gaussian wave packet,

$$\phi(t) = \frac{1}{\sqrt{2\pi\Delta(t)^2}} \exp\left(-\frac{x^2 + y^2}{4\Delta(t)^2}\right),$$

where the time-dependent spread is given by

$$\Delta(t) = \sqrt{\Delta_0^2 + \frac{t^2}{4m^2\Delta_0^2}}. \quad (6.19)$$

Since the Dirac equation converges into the Schrödinger equation in the non-relativistic limit, we initialize the positive-energy, spin-up component of the Dirac spinor with the solution of the Schrödinger equation,

$$\Psi(0) = (\Psi_1^+, \Psi_2^+, \Psi_1^-, \Psi_2^-) = (\phi(0), 0, 0, 0),$$

and measure the spread $\Delta(t)$ at time t by

$$\Delta(t) = \sqrt{\int \frac{x^2 + y^2}{2} |\Psi_1^+|^2 dV} / \sqrt{\int |\Psi_1^+|^2 dV}, \quad (6.20)$$

as proposed in Ref. [47]. Figure 6.2 depicts snapshots of the probability density for a simulation of a particle with mass $m = 0.35$ and initial spread $\Delta_0 = 14$ at different time steps. The particle is placed in the center of a quadratic box of side length $l = 100$, which is discretized on a lattice of $L_x \times L_y = 128 \times 128, 256 \times 256$ or 512×512 grid points with discretization step $\Delta t = l/L_x$, using periodic boundaries. As can be seen, the Gaussian wave packet spreads in time, which can be quantified by the spread $\Delta(t)$, depicted in Figure 6.3. As can be seen, the numerical results agree very

⁶In flat space, $g_{ij} = \delta_{ij}$, $e_a^i = \delta_a^i$, $\Gamma_i = 0$.

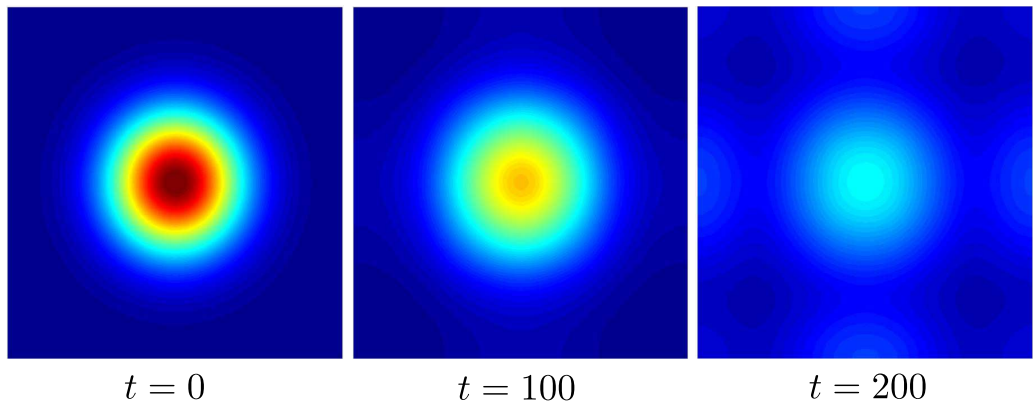


Figure 6.2: **Probability density of a free quantum particle.** Snapshots of the probability density $\rho = \Psi^\dagger \Psi$ of a Gaussian wave packet at different times. Blue and red colors denote low and high probabilities, respectively.

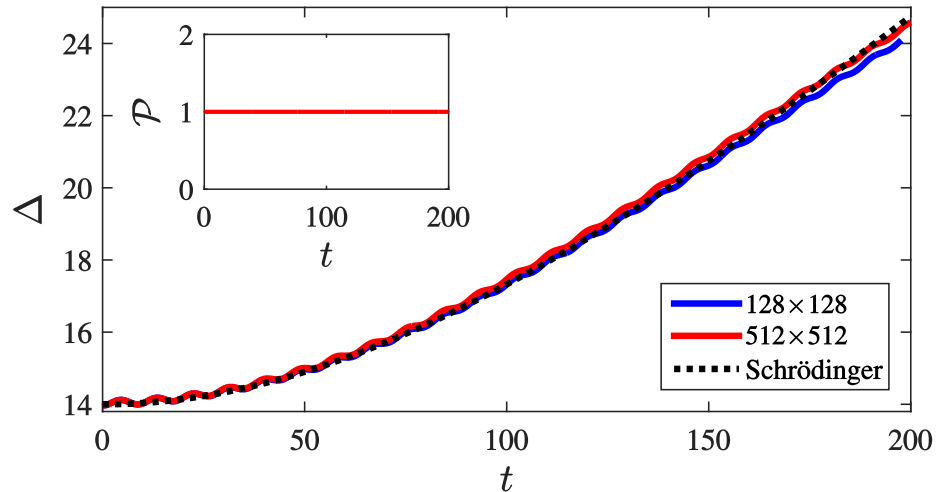


Figure 6.3: **Spread and total probability of a free quantum particle.** The time evolution of the simulated spread $\Delta(t)$ agrees very well with the analytical solution, improving with increasing system size. *Inset:* Total probability $\mathcal{P} = \int |\Psi|^2 dV$, showing perfect conservation of probability.

well with the theoretical curve, given by Eq. (6.19), and the numerical error decreases considerably with the grid resolution. The oscillations around the analytical solution (“Zitterbewegung”) are physical and originate from relativistic effects covered by the Dirac equation. In order to show that our simulations indeed conserve the probability norm of the wave function, we also measure the total probability $\mathcal{P} = \int \Psi^\dagger \Psi dV$ as function of time, as depicted in the inset of Figure 6.3. Indeed, the total probability is perfectly conserved at the level of machine precision, thanks to the unitary expansion of the collision operator, Eq. (6.16).

6.4.2 Quantum harmonic oscillator

As a second example, we consider the harmonic oscillator solution of the Schrödinger equation in two-dimensional flat space by introducing a harmonic potential, $V = -\frac{1}{2}m\omega^2(x^2 + y^2)$, where ω denotes the oscillation frequency. Due to the presence of the harmonic potential, the solution is spatially confined, leading to discrete energy levels $E_{n_x, n_y} = \omega(n_x + n_y + 1)$. The full solution of the Schrödinger equation is given by

$$\phi_{n_x, n_y}(t) = \frac{\beta}{\sqrt{\pi 2^{n_x} 2^{n_y} n_x! n_y!}} H_{n_x}(\beta x) H_{n_y}(\beta y) e^{-\frac{\beta^2}{2}(x^2+y^2)}, \quad (6.21)$$

where n_x and n_y label the energy quantum numbers, $H_n(x)$ denotes the n -th Hermite polynomial and $\beta = \sqrt{m\omega}$. For the ground state, $n_x = n_y = 0$, the solution is given by a Gaussian wave packet, as in the previous subsection. In contrast to the free particle solution, the spread of the Gaussian is constant in time, since the particle is confined within the harmonic potential:

$$\phi_{0,0}(t) = \frac{1}{\sqrt{2\pi\Delta_0}} \exp\left(-\frac{x^2 + y^2}{4\Delta_0^2}\right),$$

where $\Delta_0 = \frac{1}{\sqrt{2m\omega}}$. As before, we initialize the Dirac spinor by $\Psi(0) = (\phi(0), 0, 0, 0)$ for a particle with mass $m = 0.1$ and initial spread $\Delta_0 = 14$, confined in a potential with frequency $\omega = \frac{1}{2m\Delta_0^2} = 0.0255$. The particle is placed in the center of a quadratic box of side length $l = 100$, simulated by $L_x \times L_y = 128 \times 128, 256 \times 256$ and 512×512 grid points with discretization step $\Delta t = l/L_x$, using periodic boundaries. The harmonic potential is

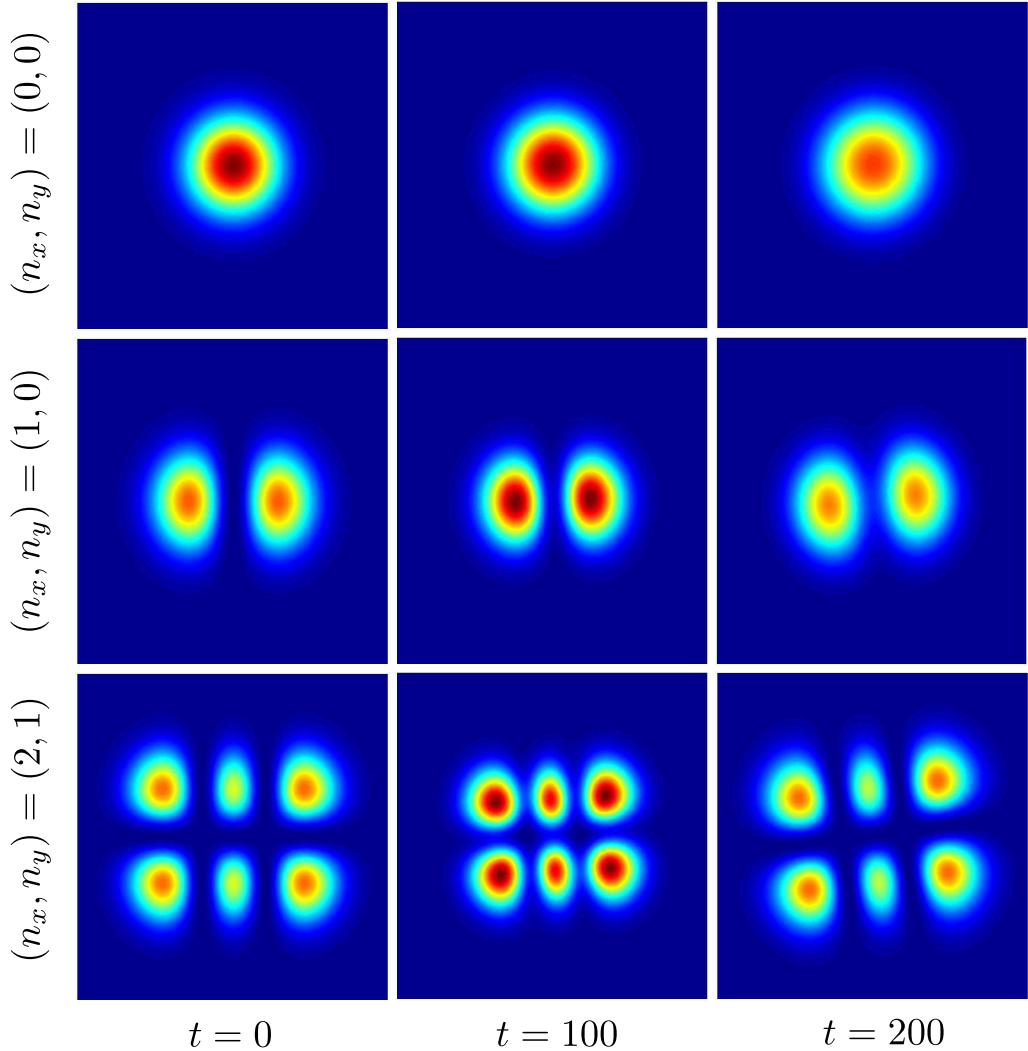


Figure 6.4: **Probability density of a quantum harmonic oscillator.** Snapshots of the probability density $\rho = \Psi^\dagger \Psi$ of a quantum harmonic oscillator at different times and energy levels, labeled by the energy quantum numbers n_x and n_y . Blue and red colors denote low and high probabilities, respectively.

implemented as a scalar potential⁷ according to Eq. (6.11). Figure 6.4 depicts snapshots of the probability density at different times and energy

⁷Implementing the scalar potential as the zeroth component of the four-vector potential would not give rise to a finite discrete energy spectrum and would thus not confine the Dirac particle, as discussed in Ref. [76].

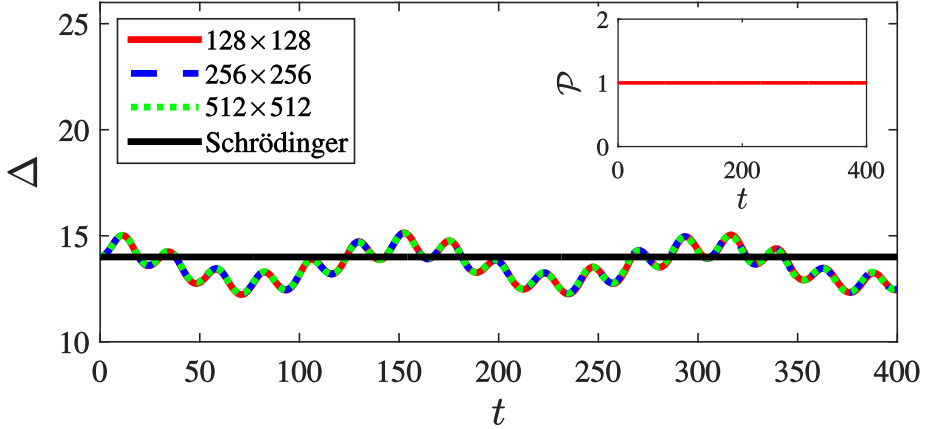


Figure 6.5: **Spread and total probability of a particle confined in a harmonic potential.** The simulated spread $\Delta(t)$ oscillates around the non-relativistic, stationary solution. *Inset:* Total probability $\mathcal{P} = \int |\Psi|^2 dV$, showing perfect conservation of probability.

levels (n_x, n_y) , showing that the initial wave function remains indeed confined within the harmonic potential. The deviations from the initial state correspond to oscillations around the stationary Schrödinger solution and originate from the relativistic effects inherent to the Dirac equation. Figure 6.5 depicts the spread $\Delta(t)$, measured using Eq. (6.20), showing high-frequency quantum oscillations around the constant initial value $\Delta_0 = 14$. We have also measured the total probability $\mathcal{P} = \int \Psi^\dagger \Psi dV$, which is perfectly conserved in our simulations, as shown in the inset of Figure 6.5. Because of the confining effect of the harmonic potential, the wave function stays bounded and stable during the full time span of the simulation and oscillates periodically around the initial value of the spread. In addition, the stability of our solution is not sensitive on the grid resolution. This is a considerable improvement compared to the simulations reported in Ref. [47], which suffer from instabilities, probably originating from an unsuited implementation of the scalar potential.

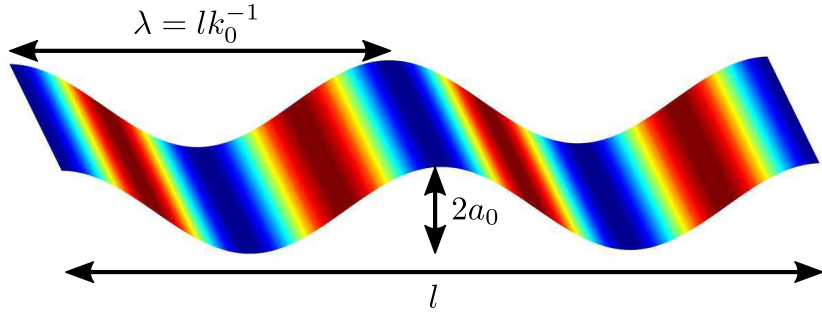


Figure 6.6: **Curved wavy surface.** The height of the curved surface is described by $h = a_0 \cos\left(\frac{2\pi k_0 x}{l}\right)$. The colors denote the first metric component $g_{xx} = 1 + h_x^2$, where blue and red regions correspond to low and high values, respectively.

6.4.3 Dirac plane waves in curved space

Next, we present the first application of the Dirac formalism in curved space, by considering a two-dimensional rippled surface of length l , equipped with periodic out-of-plane displacements, as illustrated in Figure 6.6. The surface is parametrized by

$$\vec{r} = (x, y, h(x, y)) \quad \text{with} \quad h(x, y) = a_0 \cos\left(\frac{2\pi k_0 x}{l}\right), \quad (6.22)$$

where a_0 denotes the amplitude and k_0 the wave vector of the surface ripples. The corresponding metric reads

$$g = \begin{pmatrix} 1 + h_x^2 & 0 \\ 0 & 1 \end{pmatrix}, \quad \text{where} \quad h_x := \partial_x h(x, y).$$

With this metric tensor, the Dirac equation becomes:

$$\left(i\gamma^0 \partial_t + i \frac{\gamma^1 \partial_x}{\sqrt{1 + h_x^2}} + i\gamma^2 \partial_y \right) \Psi = m\Psi.$$

We want to focus on the plane wave solutions of this equation, which in curved space are defined as the eigenfunctions of the Laplacian operator, i.e. $\Delta_g \Psi = k^2 \Psi$, where the eigenvalues k correspond to the particle's momentum. In our case, this eigenvalue equation becomes

$$\Delta_g \Psi = \frac{1}{\sqrt{g}} \partial_i (\sqrt{g} g^{ij} \partial_j \Psi) = \frac{1}{\sqrt{1+h_x^2}} \partial_x \left(\frac{1}{\sqrt{1+h_x^2}} \partial_x \Psi \right) + \partial_y^2 \Psi = k^2 \Psi,$$

6.4. METHOD VALIDATION

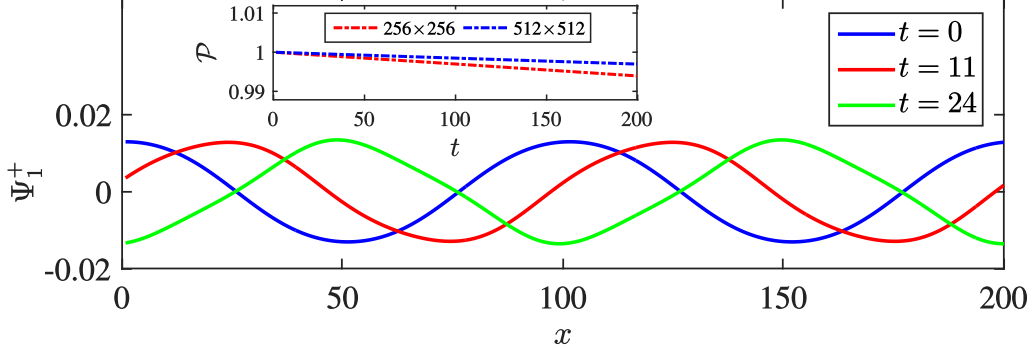


Figure 6.7: **Dirac plane wave in curved space.** Snapshots of the positive-energy spin-up component of a wave function with mass $m = 0.1$ and momentum quantum number $n_x = 1$, evolving on a curved surface ($a_0 = 10$, $k_0 = 2$) according to the Dirac equation in curved space. The simulated solution coincides with the analytical expression. *Inset:* Total probability \mathcal{P} as function of time for different grid resolutions.

which is solved by $\Psi \sim e^{i(k_x \ell(x) + k_y y)}$, where $\ell(x) = \int^x \sqrt{1 + h_x^2(x')} dx'$ represents the generalized phase of the plane wave in curved space. The full solution of the Dirac equation is given by [77]

$$\Psi_{(k_x, k_y)} = N \begin{pmatrix} 1 \\ 0 \\ 0 \\ \frac{k_x + ik_y}{E+m} \end{pmatrix} e^{i(k_x \ell(x) + k_y y - Et)}, \quad (6.23)$$

with normalization constant $N = (V(1 + \frac{k_x^2 + k_y^2}{(E+m)^2}))^{-1/2}$, surface area $V = \int \sqrt{g} dx dy$ and energy $E = \sqrt{k_x^2 + k_y^2 + m^2}$.

In the simulations, we consider a quadratic sheet with side length $l = 200$, curved by a periodic displacement with amplitude $a_0 = 10$ and wave vector $k = 2$. We neglect the trivial propagation of the plane wave in y -direction by setting $k_y = 0$, which allows us to model the sheet by $L_x \times L_y = 256 \times 1$ grid points with discretization step $\Delta t = l/L_x$, using periodic boundary conditions in x - and y -direction. Because of the periodicity, the x -momentum of the plane wave is quantized into discrete values $k_x = 2\pi n_x / \ell(l)$, where $n_x \in \mathbb{Z}$ represents the momentum quantum number. Figure 6.7 depicts

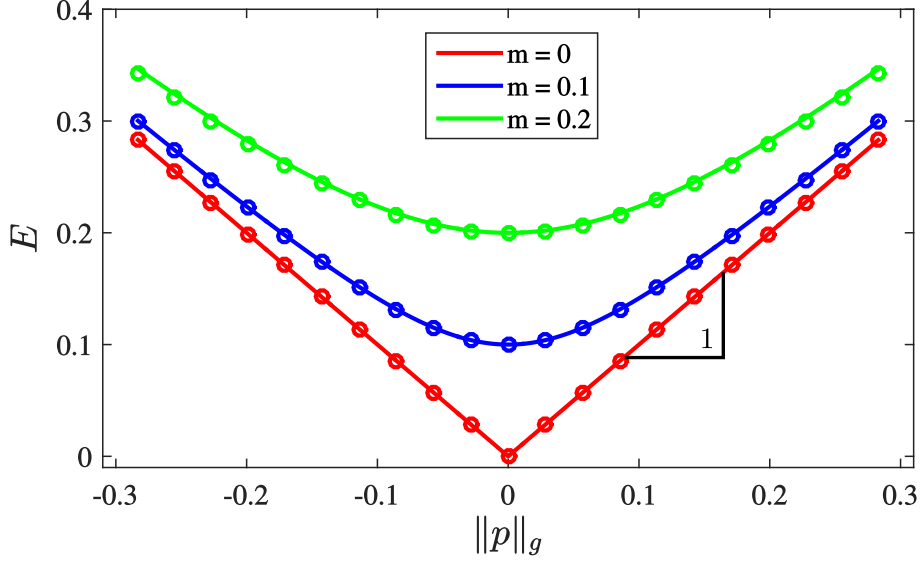


Figure 6.8: **Energy-momentum relation of a plane wave in curved space.** Shown is the energy E as function of the absolute momentum $\|p\|_g = \sqrt{p^i g_{ij} p^j}$, measured from the energy-momentum tensor of the wave function. All data points are in excellent agreement with the theoretical relation $E = \sqrt{\|p\|_g^2 + m^2}$, denoted by the solid lines. For $m = 0$, the slope of the Dirac cone yields the correct value for the speed of light, $c = 1$ in Planck units, recovered at machine precision.

snapshots of a wave function with mass $m = 0.1$ and momentum quantum number $n_x = 1$, propagating in x -direction and following the analytical expression given by Eq. (6.23). The inset shows the conserved probability $\mathcal{P} = \int \Psi^\dagger \Psi dV$ as function of time, decreasing slightly due to numerical errors originating from non-unitary expansion of the forcing term in Eq. (6.16). However, for increasing grid resolutions, the loss of probability improves considerably to about 0.1% per 100 time units for a grid of size $L_x \times L_y = 512 \times 1$.

To prove that our simulations recover the correct energy-momentum relation, we measure the energy E as function of the total momentum $\|p\|_g = \sqrt{p^i g_{ij} p^j}$ for different momentum quantum numbers $n_x \in [-10..10]$ and particle masses $m \in \{0, 0.1, 0.2\}$, as depicted in Figure 6.8. As can be seen, all simulations agree very well with the theoretical energy-momentum

relation, given by $E = \sqrt{\|p\|_g^2 + m^2}$ and denoted by the solid lines. We have checked that the result does not depend on the time step at which the measurement was performed, since energy and momentum are conserved in our simulations.

6.5 Dirac formalism for strained graphene

After having validated our model on standard benchmark problems, we now consider an important application of the Dirac formalism, namely electron transport in nonuniformly strained graphene. The low-energetic electronic states we are interested in are described by the massless effective Dirac Hamiltonian [6],

$$H_D^* = -i \int \Psi^\dagger \sigma^a (v_a^{*i} \partial_i + \Gamma_a^* - i A_a^*) \Psi d^2x, \quad (6.24)$$

where $v_a^{*i} = (\delta_{ai} + u_{ai} - \beta \epsilon_{ai})$ denotes the space-dependent Fermi-velocity, $\Gamma_a^* = \frac{1}{2} \partial_j v_a^{*j}$ a complex vector field, and A_a^* a pseudovector potential given by $A_a^* = (A_1^*, A_2^*) = \frac{\beta}{2a} (\epsilon_{xx} - \epsilon_{yy}, -2\epsilon_{xy})$. Here, β is a material-dependent parameter, a the lattice spacing, and $\epsilon_{ij} = u_{ij} + \frac{1}{2} \partial_i h \partial_j h$ denotes the generalized strain tensor, where u_{ij} and h correspond to in-plane and out-of-plane displacements, respectively.

On the other hand, the Hamiltonian corresponding to the original Dirac equation in curved spacetimes (6.11) reads

$$H_D = \int \Psi^\dagger \mathcal{H}_D \Psi d^2x = -i \int \Psi^\dagger \sigma^a e_a^i (\partial_i + \Gamma_i - i A_i) \Psi \sqrt{g} d^2x, \quad (6.25)$$

where \mathcal{H}_D denotes the Hamiltonian density, e_a^i the tetrad, Γ^i the spin connection and A_i an external vector potential. As can be seen, this Hamiltonian is different from the effective Hamiltonian for graphene (6.24), meaning that the original Dirac formalism for curved spacetimes cannot be applied straightforwardly to the study of graphene. Still, we find that it is indeed possible to match both Hamiltonians, H_D^* and H_D , if the following relations are fulfilled:

$$v_a^{*i} = \sqrt{g} e_a^i, \quad \Gamma_a^* = \sqrt{g} e_a^i \Gamma_i, \quad A_a^* = \sqrt{g} e_a^i A_i. \quad (6.26)$$

From the first equation, the effective metric tensor g can be derived by using the explicit expression of the tetrad, given by Eq. (6.5). Because of the Hermitianity of the Dirac Hamiltonian H_D , the second equation for the spin connection Γ_i holds automatically once the first equation is satisfied. Thus, by using an effective metric tensor, we are able to simulate nonuniformly strained graphene by means of the original Dirac formalism for curved spacetimes.

As an example, we consider the same out-of-plane deformation $h(x)$ along the x -axis as used in Ref. [6], setting $\beta = 1$. The corresponding generalized strain tensor ϵ , the Fermi velocity v^* , the complex vector field Γ^* as well as the pseudovector potential A^* are given by

$$\epsilon_{ij} = \begin{pmatrix} f(x) & 0 \\ 0 & 0 \end{pmatrix}, \quad v_a^{*i} = \begin{pmatrix} 1 - f(x) & 0 \\ 0 & 1 \end{pmatrix}, \quad \Gamma_a^* = \left(-\frac{f'(x)}{2}, 0\right), \quad A_a^* = (0, 0),$$

where $f(x) = \frac{1}{2}(\partial_x h(x))^2$. The corresponding effective metric tensor g_{ij} , the spin connection Γ^i and the external vector potential A_i are found from relations (6.26):

$$g_{ij} = \begin{pmatrix} 1 & 0 \\ 0 & (1 - f(x))^2 \end{pmatrix}, \quad \Gamma_i = \left(-\frac{f'(x)}{2(1-f(x))}, 0\right), \quad A_i = (0, 0). \quad (6.27)$$

Accordingly, using the Hamiltonian density defined in Eq. (6.25), the Dirac equation becomes ⁸:

$$i\partial_t \Psi = \mathcal{H}_D \Psi = -i\sigma^a e_a^i (\partial_i + \Gamma_i + iA_i) \Psi \sqrt{g} = -i \left(\sigma^1 \left(\partial_1 - \frac{f'(x)}{2} \right) + \sigma^2 \partial_2 \right) \Psi,$$

and is solved by

$$\Psi_{(k_x, k_y)} = \frac{N}{\sqrt{1 - f(x)}} \begin{pmatrix} 1 \\ 0 \\ 0 \\ \frac{k_x + ik_y}{E} \end{pmatrix} e^{i(k_x \ell(x) + k_y y - Et)}, \quad (6.28)$$

⁸Note the additional factor of \sqrt{g} originating from the volume element of the space integral in (6.25), which must be taken into account in the QLB algorithm by replacing $\tilde{\mathcal{C}}_a \rightarrow \sqrt{g}\tilde{\mathcal{C}}_a$ in Eq. (6.17) and $e_a^i \rightarrow \sqrt{g}e_a^i$ in Eq. (6.18).

where $N = (2 \int \frac{dxdy}{1-f(x)})^{-1/2}$ denotes the normalization constant, $\ell(x) = \int^x \frac{dx'}{1-f(x')}$ the generalized phase and $E = \sqrt{k_x^2 + k_y^2}$ the energy.

As an example, we consider a periodic arrangement of ripples, modeled by an out-of-plane deformation

$$h(x, y) = a_0 \cos(qx), \quad \text{with } q = \frac{2\pi k_0}{l}, \quad (6.29)$$

where a_0 denotes the amplitude, q the wave vector, l the length of the sheet and k_0 the mode of the ripples, as depicted in Figure 6.6. For this type of deformation, the Dirac spinor (6.28) becomes:

$$\Psi_{(k_x, k_y)} = \frac{N}{\sqrt{1 - \frac{1}{2}a_0^2 q^2 \sin^2(qx)}} \begin{pmatrix} 1 \\ 0 \\ 0 \\ \frac{k_x + ik_y}{E} \end{pmatrix} e^{i(k_x \ell(x) + k_y y - Et)}, \quad (6.30)$$

with $\ell(x) = \frac{1}{q\sqrt{1 - \frac{1}{2}a_0^2 q^2}} \arctan\left(\sqrt{1 - \frac{1}{2}a_0^2 q^2} \tan(qx)\right).$

As noted in Ref. [6], this solution does not only give rise to a position-dependent Fermi-velocity, but also to an inhomogeneous carrier probability density, given by

$$v_F = 1 - \frac{1}{2}a_0^2 q^2 \sin^2(qx) \quad \text{and} \quad \|\Psi\|^2 = \frac{N}{1 - \frac{1}{2}a_0^2 q^2 \sin^2(qx)}. \quad (6.31)$$

In order to measure the position-dependent Fermi velocity, we consider the local energy-momentum relation by measuring the energy density $\varepsilon = i\Psi^\dagger \partial_t \Psi$ (6.9) and momentum density $\pi^i = i\Psi^\dagger \sigma^a e_a^i \Psi$ (6.10). To compare the results in curved space with the solution obtained in Ref. [6], the curved-space momentum density has to be transformed into the laboratory frame: $\pi_{\text{lab}}^a = \frac{1}{\sqrt{g}} e^a_i \pi^i$, where the additional factor $1/\sqrt{g}$ originates from the volume element contained in the Hamiltonian density in Eq. (6.25). Figure 6.9 depicts the local energy-momentum relation for differently curved, periodic graphene sheets with side length $l = 200$, discretized into $L_x \times L_y = 256 \times 1$ grid points. The data points correspond to a wide range of momenta, $k_x = 2\pi n_x / \ell(l)$, $n_x \in [-10..10]$, and we only consider propagation in x -direction

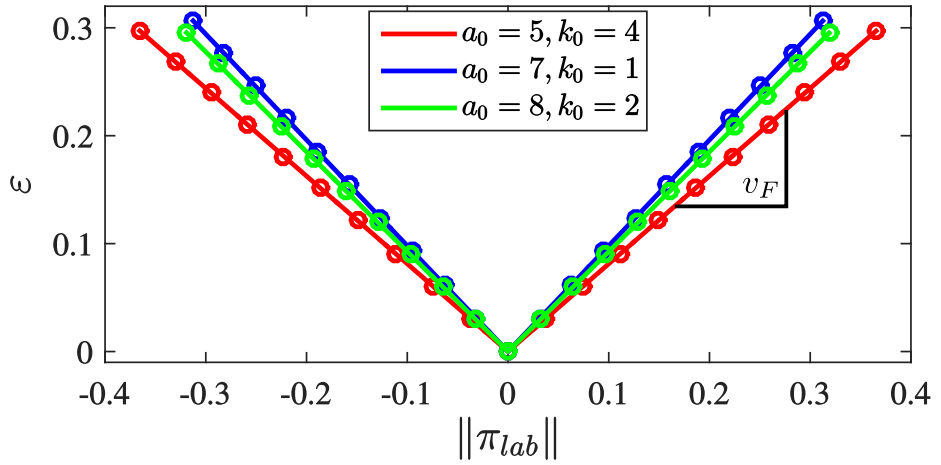


Figure 6.9: **Position-dependent energy-momentum relation in rippled graphene.** The curves depict the energy density ε as function of the momentum density $\|\pi_{\text{lab}}\| = \sqrt{\pi_{\text{lab}}^a \pi_{\text{lab}}^a}$, measured at position $x = 37$ for three graphene sheets, differing by the amplitude a_0 and mode k_0 of the ripples. The slope of the Dirac cones corresponds to the curvature- and position-dependent Fermi velocity v_F , and all data points agree excellently with the theoretical prediction $\varepsilon = v_F(x)\|\pi_{\text{lab}}\|$, denoted by the solid lines.

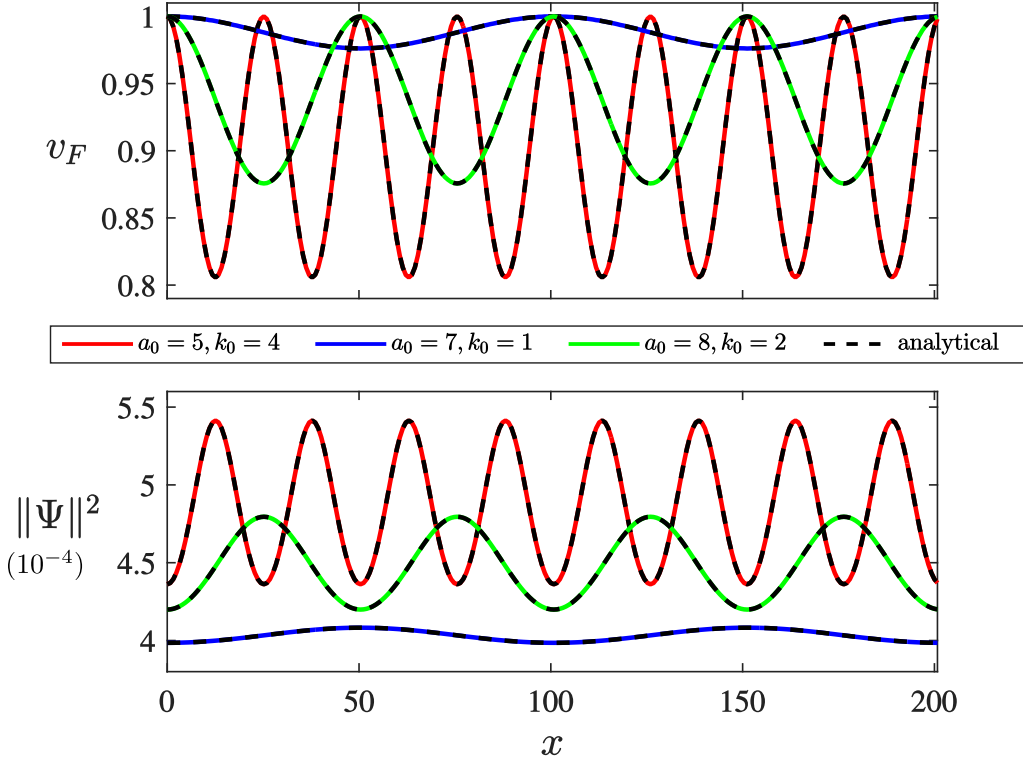


Figure 6.10: **Position-dependent Fermi velocity and carrier density.** The upper plot depicts the Fermi velocity v_F and the lower plot the probability density $\|\Psi\|^2$ as function of the position x for three graphene sheets, differing by the amplitude a_0 and the mode k_0 of the ripples. All curves perfectly match the theoretical predictions, denoted by the dashed black lines.

by setting $k_y = 0$. As can be seen, all data points fall perfectly in line with the analytically predicted Dirac cones, and we have checked that the shape of the Dirac cone does not depend on the time at which measurement has been taken. The corresponding space-dependent Fermi velocities $v_F(x)$ can be measured from the slope of the local Dirac cones, given by $\varepsilon = v_F \|\pi_{\text{lab}}\|$. The results are shown in the upper plot of Figure 6.10, in excellent agreement with the theory, Eq. (6.31). Finally, we also measure the carrier probability density, $\rho = \Psi^\dagger \Psi$, as depicted in the lower plot of Figure 6.10, observing the predicted position-dependent inhomogeneity, Eq. (6.31).

6.6 Landau levels in curved graphene

Another interesting phenomenon in graphene is the Landau quantization, describing the discretization of the electronic energy spectrum in the presence of a magnetic field. We consider a two-dimensional graphene sheet of size $l_x \times l_y$, oriented in the x - y -plane and pervaded by a uniform magnetic field of strength B in z -direction. The vector potential corresponding to the magnetic field can be written in Landau gauge as $A^a = (0, Bx)$ and is added to the Dirac equation by minimal coupling, as explained in Eq. (6.11). Due to the presence of the magnetic potential, the electrons are confined to discrete cyclotron orbits, corresponding to discrete energy levels (the Landau levels), which for relativistic particles are given by

$$E_n = \text{sgn}(n) \sqrt{2B|n|}, \quad \text{for } n \in \mathbb{Z}, \quad (6.32)$$

where n denotes the energy quantum number.

In flat space, the Dirac equation can be solved analytically, which for the magnetic potential introduced above yields [78]

$$\Psi_{n,k_y} = \frac{C_n}{\sqrt{l_y}} \begin{pmatrix} \text{sgn}(n) i^{|n|-1} \phi_{|n|-1}(x) \\ 0 \\ 0 \\ i^{|n|} \phi_{|n|}(x) \end{pmatrix} e^{i(k_y y - E_n t)}, \quad (6.33)$$

where the normalization constant is given by

$$C_n = \begin{cases} 1 & n = 0, \\ \frac{1}{\sqrt{2}} & n \neq 0, \end{cases}$$

and

$$\phi_n(x) = \frac{1}{\sqrt{\sqrt{\pi} 2^n n! \ell^2}} H_n \left(\frac{x - x_0}{\ell} \right) \exp \left(-\frac{(x - x_0)^2}{2\ell^2} \right),$$

where $\ell = 1/\sqrt{|B|}$ denotes the magnetic length, and $x_0 = k_y \ell^2$ the shift of the center of the wave function. It should be noted that ϕ_n resembles the wave function of the harmonic oscillator, shifted by x_0 (cf. Eq. (6.21)), explaining the discrete energy spectrum.

In our simulations, we use the same geometrical setup as in the previous section (see Figure 6.6), where the ripples are characterized by the amplitude a_0 and mode k_0 . As before, we neglect the trivial propagation in y -direction by setting $k_y = 0$. Instead of initializing the numerical wave function with the analytical energy eigenfunctions (6.33), we initialize Ψ with a Gaussian wave packet, given by

$$\Psi(t=0) = \frac{\beta}{\sqrt{4\pi}} \begin{pmatrix} 1 \\ 0 \\ 0 \\ i \end{pmatrix} e^{-\frac{\beta^2}{2}x^2}. \quad (6.34)$$

Although this wave function is not a pure eigenfunction of the Dirac Hamiltonian, it can still be decomposed in an infinite sum of energy eigenfunctions Ψ_n , whose individual intensities a_n depend on the amount of overlap with the initial wave function:

$$\Psi = \sum_{n \in \mathbb{Z}} a_n \Psi_n, \quad \text{where } \mathcal{H}_D \Psi_n = E_n \Psi_n.$$

Knowing that the time evolution of the eigenfunctions is given by $\Psi_n(t) = \Psi_n(0) \exp(-iE_n t)$, the time evolution of the full Dirac spinor yields

$$\Psi(t) = \sum_{n \in \mathbb{Z}} a_n \Psi_n(t) = \sum_{n \in \mathbb{Z}} a_n \Psi_n(0) e^{-iE_n t}.$$

Thus, the energy eigenvalues E_n can be measured by a Fourier transformation:

$$\begin{aligned} \mathcal{F}[\Psi](E) &= \int \Psi(t) e^{iEt} dt \\ &= \sum_{n \in \mathbb{Z}} a_n \Psi_n(0) \cdot \int e^{i(E-E_n)t} dt \\ &= \sum_{n \in \mathbb{Z}} a_n \Psi_n(0) \cdot 2\pi \delta(E - E_n). \end{aligned}$$

As can be seen, the energy spectrum consists of discrete peaks at energies $E = E_n$, which correspond to the Landau levels.

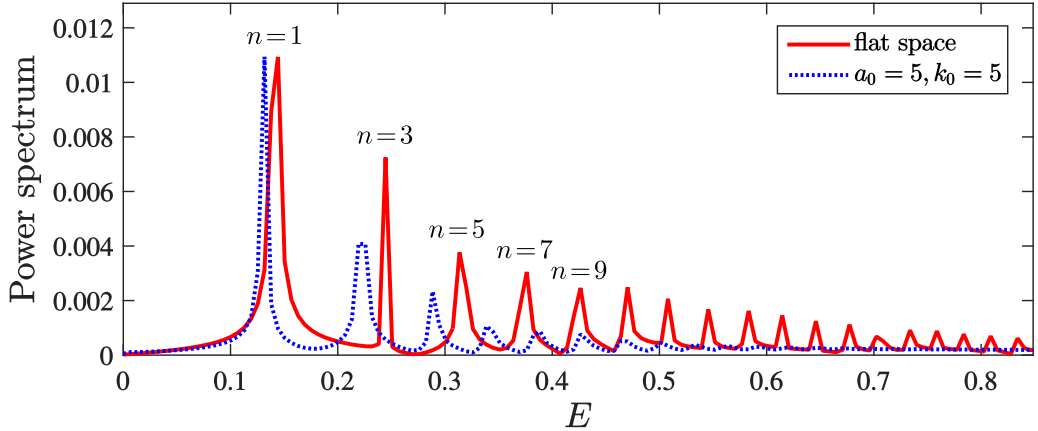


Figure 6.11: **Landau levels in a magnetic field.** The curves depict the energy spectrum, obtained by a fast Fourier transform of the time evolution of the spinor component Ψ_1^+ , for flat and curved graphene sheets. As can be seen, the spectrum consists of regularly spaced, quantized energy peaks, which correspond to the Landau levels, labeled by the energy quantum number n . For the curved sheet ($a_0 = 5$, $k_0 = 5$), the Landau levels are shifted.

At first, we consider a periodic, flat graphene sheet with side length $l_x = 200$, discretized into $L_x \times L_y = 512 \times 1$ grid points, and apply a magnetic field of strength $B = 0.01$. Figure 6.11 depicts the energy power spectrum for a Gaussian wave packet (6.34) with $\beta = 0.5$, obtained by a fast Fourier transform based on a time span of 1000 units of time. Indeed, we find regularly-spaced energy peaks corresponding to the Landau levels $n = 1, 3, 5, \dots$. Since the initial wave function is symmetric, only half of the energy eigenstates are excited, since there is no overlap with the antisymmetric eigenfunctions. Plotting the positions of the energy peaks in Figure 6.11 as function of the energy quantum number n , as depicted in Figure 6.12(a), we observe that the energy eigenvalues E_n scale with \sqrt{n} . Indeed, for $n \lesssim 20$, the simulation results agree very well with the theoretical prediction for the Landau levels in flat space, $E_n = \sqrt{2Bn}$, while for higher n , a finer grid resolution is needed to resolve the high frequent oscillations corresponding to larger energy eigenvalues.

To study the influence of spatial curvature on the Landau levels, we

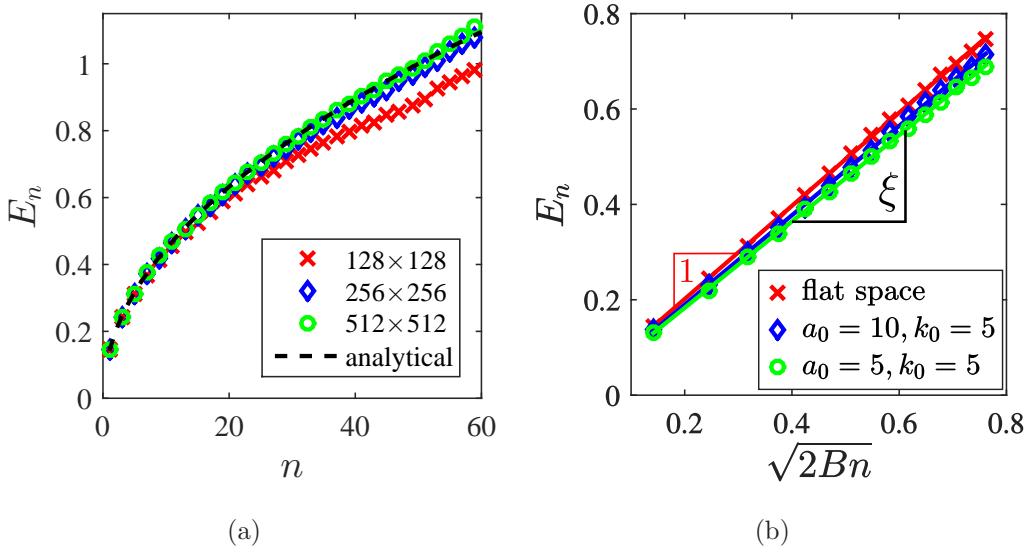


Figure 6.12: **Landau level energies vs. energy quantum number for flat and curved graphene sheets.** (a) Energy of the Landau levels E_n vs. n for a flat graphene sheet and different grid resolutions. For increasing resolution, the curves converge fast towards the analytical curve. (b) Landau energies E_n as function of \sqrt{n} for differently curved graphene sheets, characterized by the amplitude a_0 and mode k_0 of the ripples. The solid lines denote linear fits with slope ξ , showing very good agreement with the data points. For the flat space, we find $\xi = (0.98 \pm 0.01) \approx 1$, as expected from the analytical expression (6.32).

consider a curved graphene sheet with periodic ripples of the same shape as used in the previous sections, given by

$$h(x, y) = a_0 \cos(qx), \quad \text{with } q = \frac{2\pi k_0}{l},$$

where a_0 denotes the amplitude, q the wave vector, l the length of the sheet and k_0 the mode of the ripples, as depicted in Figure 6.6. The corresponding effective metric tensor and the spin connection are given by

$$g_{ij} = \begin{pmatrix} 1 & 0 \\ 0 & (1 - f(x))^2 \end{pmatrix}, \quad \Gamma_i = \left(-\frac{f'(x)}{2(1-f(x))}, 0 \right), \quad A_i = (0, 0),$$

where $f(x)$, the deformation function, is given by

$$f(x) := \frac{1}{2}(\partial_x h(x))^2 = \frac{2\pi^2}{l^2} a_0^2 k_0^2 \sin^2 \left(\frac{2\pi k_0 x}{l} \right).$$

In analogy to flat graphene sheets, we measure the positions of the discrete energy peaks in the Fourier spectrum of the wave function and determine the dependence of the Landau levels E_n on the quantum number n . Figure 6.12(b) depicts the resulting curves for three differently curved sheets, where the energy levels are plotted as function of $\sqrt{2Bn}$. We find that even on curved graphene sheets, the energy levels follow the same functional dependence as in flat space, $E_n \sim \sqrt{2Bn}$, however, the slopes of the curves differ with the ripple parameters. Thus, we claim that – within the range of parameters studied – the Landau levels in curved space are given by

$$E_n = \xi(a_0, k_0) \sqrt{2Bn}, \quad \text{for } n \in \mathbb{N},$$

where $\xi(a_0, k_0)$ depends on the deformation of the sheet. In order to characterize $\xi(a_0, k_0)$, we have performed various simulations for a range of ripple amplitudes $a_0 \in [0..10]$ and modes $k_0 \in [0..6]$. For each simulation, we determine ξ by measuring the slope of E_n as function of $\sqrt{2Bn}$ as shown in Figure 6.12(b). The results are depicted in the insets of Figure 6.13, revealing a quadratic dependence of ξ on a_0 and k_0 . The solid lines denote parabolic fits to the simulation data, and the corresponding fitting coefficients are listed

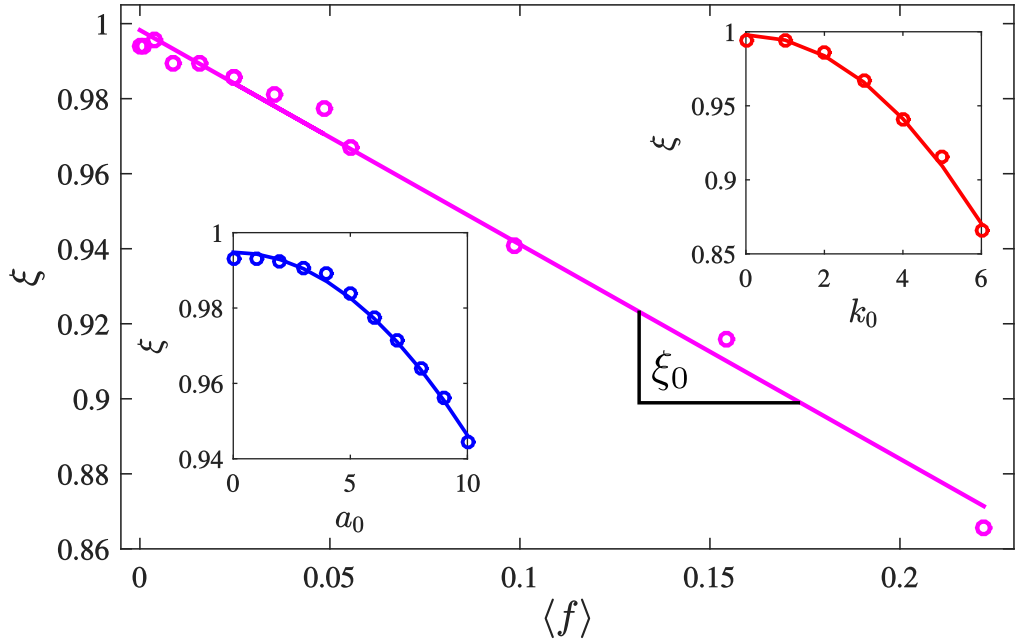


Figure 6.13: ξ vs. deformation parameters of the graphene sheet. *Insets:* Parameter ξ as function of the amplitude a_0 and mode k_0 , respectively, showing a quadratic behavior in both cases. The solid lines denote quadratic fits (for the fitting coefficients see Table 6.1). For $a_0 = 0$ and $k_0 = 0$, the difference of the curves from the theoretical value $\xi = 1$ is a measure for the numerical error, being less than 1%. *Main plot:* Data collapse, plotting ξ as function of the average spatial deformation $\langle f \rangle$.

$\xi(a_0)$	$=$	$(0.995 \pm 0.001) - (4.9 \pm 0.2) \times 10^{-4} a_0^2$
$\xi(k_0)$	$=$	$(0.998 \pm 0.006) - (3.5 \pm 0.3) \times 10^{-3} k_0^2$
$\xi(\langle f \rangle)$	$=$	$(0.998 \pm 0.003) - (0.57 \pm 0.04) \langle f \rangle$

Table 6.1: **Fitting functions for ξ .** Here, a_0 and k_0 denote the amplitude and mode of the ripples, respectively, and $\langle f \rangle$ denotes the average spatial deformation.

in Table 6.1. Interestingly, we observe, that all data points collapse onto a single line when plotting ξ as function of average deformation, defined by

$$\langle f \rangle = \frac{1}{l} \int_0^l f(x) dx,$$

as depicted in Figure 6.13, where the slope of the curve is given by $\xi_0 = -(0.57 \pm 0.04)$. As a conclusion, the Landau energies on rippled graphene sheets can be characterized by

$$E_n = (1 + \xi_0 \langle f \rangle) \sqrt{2Bn},$$

which for flat graphene sheets, $f(x) = 0$, agrees with expression (6.32).

6.7 Summary

In this chapter, we have studied the Dirac equation in curved spaces by extending the QLB method to general manifolds. To validate our model, we considered different analytically solvable problems, such as the motion of free quantum particles, the quantum harmonic oscillator and Dirac plane waves on curved surfaces. In all cases, our numerical simulations agreed excellently with the theoretical solutions. Furthermore, we studied the electronic properties of curved graphene sheets, described by an effective Dirac Hamiltonian at low temperatures. Ab initio, the original Dirac formalism in curved space-times does not match the Hamiltonian for nonuniformly strained graphene. To solve this problem, we used an effective metric tensor, resulting in the correct Hamiltonian for graphene. Indeed, we were able to correctly recover the space-dependent Fermi velocity as well as the inhomogeneous carrier density predicted in Refs. [71, 5, 6].

6.7. SUMMARY

Finally, we simulated graphene sheets in a magnetic field B , finding that the Landau levels are shifted due to the spatial curvature of the sheets. We proposed a generalized relation for the Landau energies E_n in curved graphene sheets, given by

$$E_n = (1 + \xi_0 \langle f \rangle) \sqrt{2Bn},$$

where $\langle f \rangle$ denotes the average spatial deformation, $n \in \mathbb{N}$ labels the Landau levels, and $\xi_0 \approx -0.57$ is a constant. We expect that our findings also influence the quantum Hall effect in graphene, which is closely related to the Landau quantization.

Chapter 7

Conclusion and Outlook

7.1 Summary and significance

In this thesis, we studied different kinds of flows in curved spaces by using lattice Boltzmann (LB) methods on manifolds.

Firstly, we studied the Dean instability in double-curved channels by analyzing how the curvature of the channel walls affects the bifurcation from laminar flow to Dean vortex flow. We showed that the critical Dean number at the bifurcation point depends considerably on the streamwise and cross-sectional curvature radii of the channel. For the case in which both curvature radii were equal, the critical Dean number became minimal. In the simulations, we used the LB method on manifolds to implement curvilinear coordinates, adapted perfectly to the curved walls of the channel. Although our findings are mainly of theoretical kind, they might inspire engineers to utilize the properties of Dean vortex flow in order to optimize fluid transport through curved pipes. In this context, the curvature radii of the channel walls play an essential role for the transition to vortex flow, as we have shown in this work.

Secondly, we considered flows through spaces with intrinsic curvature, as they may occur on curved two-dimensional surfaces and films. We showed that laminar, Poiseuille-like flow is considerably affected by the intrinsic curvature of space, resulting either in an enhancement or in a decrease of mass flow. We analyzed that the flux through an intrinsically curved chan-

nel depends mainly on the average perturbation of the metric tensor, which allowed us to formulate a universal flux law for general, smooth geometries in two and three dimensions. For the simulations, we used and improved the LB method with a general metric tensor, giving rise to intrinsic curvature. Indeed, our findings might have interesting applications for hydrodynamic systems with curved geometries, such as two-dimensional fluid films, since they reveal a clear correlation between the geometrical deformation of space and the transport properties of the flow. This might be of particular importance for curved lipid membranes, whose hydrodynamic properties influence the biological function of the cell membranes.

Thirdly, we investigated the effect of curvature on the fluid flow on a more fundamental basis, by considering free fluid motion past a local deformation of space, implemented as a perturbation of the metric tensor. We found that even in the absence of solid obstacles or walls, the flow exhibits loss of energy when passing the spatial deformation. Indeed, we observed that next to the metric perturbation, velocity gradients between adjacent fluid layers emerge, generating viscous stresses and thus energy dissipation. As a consequence, the flow equilibrates to a stationary state due to the curvature-induced viscous forces opposing the driving pressure drop. The effect of curvature-induced dissipation in free fluids is certainly one of the most intriguing findings of this work. In particular, since our results are general, and curvature is present in nature at all physical scales, this effect might have important implications on physical systems described by hydrodynamics on curved manifolds. For example, curvature-induced dissipation is expected to influence the two-dimensional fluidity and thus the biological function of curved lipid bilayers, constituting the cell membranes. In particular, the diffusive motion of the tracer particles used to measure the membrane viscosity [79] is probably affected by the curvature. Furthermore, curvature-induced dissipation might influence astrophysical hydrodynamic processes, such as gas dynamics in stars or clouds, and might even play a role in controversial cosmological questions concerning e.g. the fluid dynamical description of dark matter and dark energy [80, 81] or the energy

7.2. EXTENSIBILITY AND FUTURE PROSPECTS

conservation in the universe, which is still considered an open issue.

Fourthly, we studied numerical solutions to the Dirac equation in curved space by extending the quantum lattice Boltzmann (QLB) method to general manifolds. After validating our method on benchmark examples, we applied the Dirac formalism to graphene, studying several interesting effects related to electronic transport on curved graphene sheets. We were able to recover the previously predicted space-dependent Fermi velocity as well as the inhomogeneity of the carrier density. In addition, we studied the dependence of the Landau levels, triggered by a magnetic field, on the spatial deformation of the graphene sheet, finding a curvature-dependent shift of the discrete energy spectrum. We characterized the energy relation of the Landau levels in terms of the average spatial deformation of the graphene sheet.

7.2 Extensibility and future prospects

The systems studied in this work give rise to many interesting new questions with both practical and scientific relevance.

As a possible extension of our study of flows through curved channels, it would be interesting to generalize the idealized shapes of the channels to more complex geometries, resembling real physical systems in nature or engineering. Even dynamical shapes could be considered, which may be simulated by using a time-dependent metric tensor, adapting dynamically to the current shape of the channel. The fluid simulations might even be coupled to other numerical solvers, simulating the material intrinsic properties of the channel walls subject to deformations and stresses. This would offer a broad applicability to a variety of engineering problems related to hydrodynamic flows through dynamically deforming pipes.

Regarding our findings for flow through intrinsically-curved spaces, it would be interesting to address the macroscopic effects of curvature-induced dissipation from a more basic perspective, for example from kinetic theory or even molecular dynamics in curved space. In the latter model, parti-

cles would follow energy-conserving geodesic trajectories between collisions, meaning that kinetic energy would only be lost (i.e. converted into other forms of energy) during the collisions. Thus, the energy dissipation rate of the system would crucially depend on the characteristic time between consecutive collisions. In addition, on a curved manifold, the collision time may even be position-dependent, taking into account that the mean free path of the particles varies with the curvature of space. Macroscopically, the collision time affects the kinematic viscosity of the flow, thus resulting in space-dependent dissipation. It would be interesting to further develop these ideas, and to apply them to the extreme cases, such as collisionless gases or Euler fluids (i.e. gases with zero mean free path).

Furthermore, the QLB method on manifolds offers a wide spectrum of interesting new applications, ranging from relativistic quantum particles in curved geometries to solid state physics on curved surfaces. Regarding the former application, the method might be particularly useful for the study of quantum field theories in curved spaces, which is a very active area of research, aiming to find the “theory of everything” by combining quantum field theory with general relativity. In this regard, our numerical solver may provide insights into theories which are inaccessible to analytical tools, such as strongly coupled field theories. On the other hand, it would be intriguing to explore the curvature-dependent properties of electronic transport in graphene sheets to a greater extent. Since we found that curvature affects the Landau levels in graphene, it would be interesting to also study the consequences of spatial deformation on the quantum Hall effect, which has already been observed experimentally in graphene [82], and which is directly related to the Landau levels.

Beside the physical applications mentioned above, there is a list of possible technical improvements of the numerical methods, which may be implemented in the future. Firstly, the local precision of the LB method on manifolds may be considerably improved by implementing local grid refinement, meaning that the resolution of the lattice is locally increased in order to better resolve the strongly curved regions of the manifold. Secondly, the

7.2. EXTENSIBILITY AND FUTURE PROSPECTS

LB method on manifolds may be improved to become capable of simulating highly turbulent flows in curved spaces by using for example entropic LB models [83], which have been shown to achieve outstanding numerical stability for turbulent flows in flat space. Thirdly, an extension of the LB method to simulate thermal flows on manifolds would be desirable, following for example the “passive scalar” approach presented in Ref. [60]. It would be interesting to study the effect of curvature-induced dissipation with a thermal model, taking into account the energy conservation equation as well. Probably, the loss of kinetic energy would be converted into thermal energy, which might give rise to interesting new effects. Fourthly, the boundary conditions of the LB algorithm have always been a delicate issue for the study of curved-space flow, since standard inter-/extrapolation techniques cannot be generalized straightforwardly to curved manifolds. Although we have carefully checked that the boundary conditions chosen in this thesis yield the correct results, it might be interesting to test more sophisticated boundary conditions, such as improved Tamm-Mott-Smith (TMS) boundary conditions, as described in Ref. [84], which promise high accuracy and stability.

Regarding the simulations of electronic transport in graphene, it would be desirable to couple our QLB solver to time-dependent metric tensors, coming either from real experiments or from equivalent molecular dynamics simulations of real graphene sheets. In that way, the experimental findings could directly be compared to the numerical simulations. Besides that, the accuracy of the QLB method might be significantly improved by lifting the precision of the algorithm to second-order in space and time. This can be done by applying smart operator-splitting techniques, for example second-order Strang splitting [85]. Moreover, the conservation of the total probability in curved spaces may be improved by implementing the streaming operator in a unitary way, which is not as straightforward as for the collision operator, since it contains derivative expressions. Furthermore, one might change the underlying rectangular lattice to a honeycomb lattice, being perfectly adapted to the natural hexagonal structure of graphene. In

this way, lattice artifacts will probably be canceled by construction, thus improving the method’s overall precision.

Finally, many interesting ideas have arisen during this work, which could unfortunately not be fully developed in the course of this work due to time constraints.

One of these ideas is the coupling of the energy-stress tensor of the fluid to the Einstein field equations in curved space, leading to a self-consistent evolution of the metric tensor subject to the motion of the fluid matter. Only a few analytical solutions to the Einstein equations are known so far, and even numerical calculations are extremely difficult due to the high complexity of the equations. Thus, a simple and efficient numerical solver for general relativity is highly desirable. Indeed, there already exist promising applications of the LB method for numerical relativity, based e.g. on the so-called “Z4 formulation” of the Einstein equations [86]. A lattice-kinetic description of Einstein’s equations would provide a wide range of applications, starting from simulations of matter flow in stars and ending with the cosmological evolution of the universe.

Some of the ideas mentioned in this outlook might be implemented straightforwardly, while others will probably require a large amount of detailed work and physical intuition. Still, some ideas definitely deserve further investigation.

Appendix

A.1 Navier-Stokes equation from discrete LB equation

In this section, we prove that in the hydrodynamic limit, the curved-space LB equation,

$$f_\lambda(x + c_\lambda \Delta t, t + \Delta t) - f_\lambda(x, t) = -\frac{1}{\tau} (f_\lambda - f_\lambda^{\text{eq}}) + \Delta t \mathcal{F}_\lambda, \quad (\text{A.1})$$

converges to the covariant Navier-Stokes equations,

$$\partial_t \rho + \nabla_i (\rho u^i) = 0, \quad \partial_t (\rho u^i) + \nabla_j T^{ij} = 0,$$

describing fluid flows in curved spaces. To this end, we first perform a Taylor expansion of the distribution function in Eq. (A.1), which yields:

$$\Delta t D_t f_\lambda + \frac{\Delta t^2}{2!} D_t^2 f_\lambda + \dots = -\frac{1}{\tau} (f_\lambda - f_\lambda^{\text{eq}}) + \Delta t \mathcal{F}_\lambda, \quad (\text{A.2})$$

where $D_t := \partial_t + c_\lambda^i \partial_i$ denotes the material derivative, and the dots indicate irrelevant higher order terms $\sim \mathcal{O}(\Delta t^3)$. In order to prove that our model correctly recovers the hydrodynamic conservation equations (covariant Navier-Stokes equations), we perform a Chapman-Enskog multiscale expansion by expanding the distribution function as well as the time and space derivatives in terms of the Knudsen number ε [87, 88]:

$$f = f^{(0)} + \varepsilon f^{(1)} + \varepsilon^2 f^{(2)} + \dots, \quad \partial_t = \varepsilon \partial_t^{(1)} + \varepsilon^2 \partial_t^{(2)} + \dots, \\ (\partial_i, \mathcal{F}, A, B^i, C^{ij}) = \varepsilon (\partial_i^{(1)}, \mathcal{F}^{(1)}, A^{(1)}, B^{(1),i}, C^{(1),ij}).$$

Plugging everything into Eq. (A.2) and comparing orders of ε , we obtain the following set of equations:

$$\mathcal{O}(\varepsilon^0) : \quad f_\lambda^{(0)} = f_\lambda^{\text{eq}}, \quad (\text{A.3})$$

$$\mathcal{O}(\varepsilon^1) : \quad D_t^{(1)} f_\lambda^{(0)} = -\frac{1}{\tau\Delta t} f_\lambda^{(1)} + \mathcal{F}_\lambda^{(1)}, \quad (\text{A.4})$$

$$\mathcal{O}(\varepsilon^2) : \quad \partial_t^{(2)} f_\lambda^{(0)} + \left(1 - \frac{1}{2\tau}\right) D_t^{(1)} f_\lambda^{(1)} = -\frac{1}{\tau\Delta t} f_\lambda^{(2)} - \frac{\Delta t}{2} D_t^{(1)} \mathcal{F}_\lambda^{(1)}. \quad (\text{A.5})$$

The moments of $f_\lambda^{(0)} = f_\lambda^{\text{eq}}$ and $f_\lambda^{(1)}$ can be deduced from the fact that the collision operator conserves mass and momentum, i.e.

$$\sum_\lambda f_\lambda \sqrt{g} = \sum_\lambda f_\lambda^{\text{eq}} \sqrt{g} = \rho, \quad \sum_\lambda f_\lambda c_\lambda^i \sqrt{g} = \sum_\lambda f_\lambda^{\text{eq}} c_\lambda^i \sqrt{g} = \rho u^i$$

Thus we find:

$$\begin{aligned} \sum_\lambda f_\lambda^{(0)} \sqrt{g} &= \rho, & \sum_\lambda f_\lambda^{(1)} \sqrt{g} &= 0, \\ \sum_\lambda f_\lambda^{(0)} c_\lambda^i \sqrt{g} &= \rho u^i, & \sum_\lambda f_\lambda^{(1)} c_\lambda^i \sqrt{g} &= 0, \\ \sum_\lambda f_\lambda^{(0)} c_\lambda^i c_\lambda^j \sqrt{g} &= \Pi^{(0),ij} = \Pi^{\text{eq},ij}, & \sum_\lambda f_\lambda^{(1)} c_\lambda^i c_\lambda^j \sqrt{g} &= \Pi^{(1),ij}, \\ \text{where } \Pi^{\text{eq},ij} &= \rho (c_s^2 g^{ij} + u^i u^j). \end{aligned}$$

Moments of Eq. (A.4-A.5)

Taking the moments of Eq. (A.4) yields:

$$\sum_\lambda (A.4) \sqrt{g} : \quad \partial_t^{(1)} \rho + \bar{\partial}_i^{(1)} (\rho u^i) = A^{(1)}, \quad (\text{A.6})$$

$$\sum_\lambda c_\lambda^i (A.4) \sqrt{g} : \quad \partial_t^{(1)} (\rho u^i) + \bar{\partial}_j^{(1)} \Pi^{(0),ij} = B^{(1),i}, \quad (\text{A.7})$$

where A and B^i are the moments of the forcing term (2.23-2.24) and $\bar{\partial}_i := \partial_i - \Gamma_{ij}^j$. Here, the additional Christoffel symbol term in the derivative $\bar{\partial}_i$ originates from the metric determinant \sqrt{g} :

$$\sum_\lambda c_\lambda^i \partial_i f_\lambda^{(0)} \sqrt{g} = \left(\partial_i - \frac{\partial_i \sqrt{g}}{\sqrt{g}} \right) \sum_\lambda c_\lambda^i f_\lambda^{(0)} \sqrt{g} = \partial_i (\rho u^i) - \Gamma_{ij}^j (\rho u^i) =: \bar{\partial}_i (\rho u^i),$$

where we have used the identity $\partial_i \sqrt{g} = \Gamma_{ij}^j \sqrt{g}$. The moments of Eq. (A.5) are given by

$$\sum_\lambda (A.5) \sqrt{g} : \quad \partial_t^{(2)} \rho = -\frac{\Delta t}{2} \left(\partial_t^{(1)} A^{(1)} + \bar{\partial}_i^{(1)} B^{(1),i} \right), \quad (\text{A.8})$$

$$\sum_\lambda c_\lambda^i (A.5) \sqrt{g} : \quad \partial_t^{(2)} (\rho u^i) = \bar{\partial}_j^{(1)} \sigma^{(1),ij} - \frac{\Delta t}{2} \partial_t^{(1)} B^{(1),i}, \quad (\text{A.9})$$

where $\sigma^{(1),ij}$, the viscous stress tensor (rescaled by ε), is defined by

$$\sigma^{(1),ij} = -\left(1 - \frac{1}{2\tau}\right) \Pi^{(1),ij} = -\left(1 - \frac{1}{2\tau}\right) \sum_\lambda c_\lambda^i c_\lambda^j f_\lambda^{(1)} \sqrt{g}. \quad (\text{A.10})$$

Continuity Equation

For the continuity equation, we add $\varepsilon \cdot (A.6)$ and $\varepsilon^2 \cdot (A.8)$:

$$\partial_t \rho + \bar{\partial}_i (\rho u^i) = A - \frac{\Delta t}{2} (\partial_t A + \bar{\partial}_i B^i)$$

After inserting the explicit expression for A (2.23), we obtain the continuity equation at first order in Δt :

$$\partial_t \rho + \nabla_i (\rho u^i) = 0 + \mathcal{O}(\Delta t) \quad (\text{A.11})$$

where ∇ denotes the covariant derivative.

Momentum Equation

Adding $\varepsilon \cdot (A.7)$ and $\varepsilon^2 \cdot (A.9)$ yields the momentum conservation equation:

$$\partial_t (\rho u^i) + \bar{\partial}_j \Pi^{(0),ij} = \bar{\partial}_j \sigma^{ij} + B^i - \frac{\Delta t}{2} \partial_t B^i.$$

Inserting the explicit expressions for B^i (2.24) and $\Pi^{(0),ij}$ (2.19) yields the Navier-Stokes momentum equation at first order in Δt :

$$\partial_t (\rho u^i) + \nabla_j (\rho u^i u^j + \rho c_s^2 g^{ij}) = \nabla_j \sigma^{ij} + \mathcal{O}(\Delta t), \quad (\text{A.12})$$

where σ^{ij} is the viscous stress tensor, whose explicit form in terms of ρ and u^i will be derived in the next section.

Viscous Stress Tensor

For the derivation of the viscous stress tensor σ^{ij} , we rewrite

$$\begin{aligned} \sigma^{ij} &\stackrel{(A.10)}{=} -\left(1-\frac{1}{2\tau}\right)\varepsilon\sum_{\lambda}c_{\lambda}^ic_{\lambda}^jf_{\lambda}^{(1)}\sqrt{g} \\ &\stackrel{(A.4)}{=} \left(\tau-\frac{1}{2}\right)\Delta t\varepsilon\sum_{\lambda}c_{\lambda}^ic_{\lambda}^j\left(D_t^{(1)}f_{\lambda}^{(0)}-\mathcal{F}_{\lambda}^{(1)}\right)\sqrt{g} \\ &\approx \left(\tau-\frac{1}{2}\right)\Delta t\left(\bar{\partial}_k\Sigma^{\text{eq},ijk}-C^{ij}\right), \end{aligned}$$

where we have assumed that $\left(\tau-\frac{1}{2}\right)\Delta t\partial_t^{(1)}\Pi^{(0),ij}\ll 1$. After plugging in the explicit expressions for $\Sigma^{\text{eq},ijk}$ (2.20) and C^{ij} (2.25), we obtain

$$\sigma^{ij}=\nu\left(\nabla^j(\rho u^i)+\nabla^i(\rho u^j)+g^{ij}\nabla_k(\rho u^k)\right), \quad (\text{A.13})$$

where we have defined $\nu:=\left(\tau-\frac{1}{2}\right)\Delta tc_s^2$ and neglected terms of the order $\mathcal{O}(u^3)\sim\mathcal{O}(\text{Ma}^3)$, Ma being the Mach number.

A.1.1 Cancelation of discrete lattice effects by moment corrections

We show that the spurious discrete lattice effects appearing in the Navier-Stokes equations (A.11-A.12) can be canceled at first order in Δt by a redefinition of the density $\rho\rightarrow\hat{\rho}$ and the velocity $u^i\rightarrow\hat{u}^i$. Inspired by Refs. [55, 89], we make the following ansatz for the corrected quantities $\hat{\rho}$ and \hat{u}^i :

$$\hat{\rho}=\rho+\Delta t S(\hat{\rho},\hat{u})=\sum_{\lambda}f_{\lambda}\sqrt{g}+\Delta t S(\hat{\rho},\hat{u}), \quad (\text{A.14})$$

$$\hat{\rho}\hat{u}^i=\rho u^i+\Delta t U^i(\hat{\rho},\hat{u})=\sum_{\lambda}f_{\lambda}c_{\lambda}^i\sqrt{g}+\Delta t U^i(\hat{\rho},\hat{u}), \quad (\text{A.15})$$

where $S(\hat{\rho},\hat{u})$ and $U^i(\hat{\rho},\hat{u})$ are correction functions whose explicit form has to be determined such that all spurious terms of order $\mathcal{O}(\Delta t)$ are canceled in the Navier-Stokes equations. The equilibrium distribution, $f^{\text{eq}}=f^{\text{eq}}(\hat{\rho},\hat{u})$, as well as the forcing term, $\mathcal{F}=\mathcal{F}(\hat{\rho},\hat{u})$, are evaluated with the corrected density $\hat{\rho}$ and velocity \hat{u} at each time step. To find the explicit expressions for the correction functions $S(\hat{\rho},\hat{u})$ and $U^i(\hat{\rho},\hat{u})$, we perform again a Chapman-Enskog expansion of the LB equation. To this end, we observe from Eqs.

(A.14) and (A.15), that the correction functions S and U^i alter the moments of $f^{(1)}$:

$$\sum_{\lambda} f_{\lambda}^{(1)} \sqrt{g} = -\Delta t S^{(1)}, \quad \sum_{\lambda} f_{\lambda}^{(1)} c_{\lambda}^i \sqrt{g} = -\Delta t U^{(1),i}. \quad (\text{A.16})$$

Accordingly, the moments of Eq. (A.4) and Eq. (A.5) receive extra contributions from S and U^i :

$$\sum_{\lambda} (A.4) \sqrt{g} : \quad \partial_t^{(1)} \hat{\rho} + \bar{\partial}_i^{(1)} (\hat{\rho} \hat{u}^i) = A^{(1)} + \frac{1}{\tau} S^{(1)}, \quad (\text{A.17})$$

$$\sum_{\lambda} c_{\lambda}^i (A.4) \sqrt{g} : \quad \partial_t^{(1)} (\hat{\rho} \hat{u}^i) + \bar{\partial}_j^{(1)} \Pi^{(0),ij} = B^{(1),i} + \frac{1}{\tau} U^{(1),i}, \quad (\text{A.18})$$

$$\sum_{\lambda} (A.5) \sqrt{g} : \quad \partial_t^{(2)} \hat{\rho} = \Delta t \left(1 - \frac{1}{2\tau} \right) \left(\partial_t^{(1)} S^{(1)} + \bar{\partial}_i^{(1)} U^{(1),i} \right) \quad (\text{A.19})$$

$$- \frac{\Delta t}{2} \left(\partial_t^{(1)} A^{(1)} + \bar{\partial}_i^{(1)} B^{(1),i} \right), \quad (\text{A.20})$$

$$\sum_{\lambda} c_{\lambda}^i (A.5) \sqrt{g} : \quad \partial_t^{(2)} (\hat{\rho} \hat{u}^i) = \bar{\partial}_j^{(1)} \sigma^{(1),ij} - \frac{\Delta t}{2} \partial_t^{(1)} B^{(1),i} \\ + \Delta t \left(1 - \frac{1}{2\tau} \right) \partial_t^{(1)} U^{(1),i}, \quad (\text{A.21})$$

where A and B^i are the moments of the forcing term (2.23-2.24), $\bar{\partial}_i := \partial_i - \Gamma_{ij}^j$, and $\sigma^{(1),ij}$ is the viscous stress tensor (A.10).

Continuity Equation

For the continuity equation, we add $\varepsilon(A.17)$ and $\varepsilon^2(A.20)$:

$$\partial_t \hat{\rho} + \bar{\partial}_i (\hat{\rho} \hat{u}^i) = A + \frac{1}{\tau} S - \frac{\Delta t}{2} (\partial_t A + \bar{\partial}_i B^i) + \Delta t \left(1 - \frac{1}{2\tau} \right) (\partial_t S + \bar{\partial}_i U^i). \quad (\text{A.22})$$

In order to cancel all spurious terms of order Δt , we first rescale the forcing term by a factor of $\left(1 - \frac{1}{2\tau} \right)$,

$$\mathcal{F}_{\lambda} \rightarrow \left(1 - \frac{1}{2\tau} \right) \mathcal{F}_{\lambda}, \\ (A, B^i) \rightarrow \left(1 - \frac{1}{2\tau} \right) (A, B^i). \quad (\text{A.23})$$

With this redefinition, Eq. (A.22) becomes

$$\partial_t \hat{\rho} + \bar{\partial}_i (\hat{\rho} \hat{u}^i) = \left(1 - \frac{1}{2\tau} \right) A + \frac{1}{\tau} S + \Delta t \left(1 - \frac{1}{2\tau} \right) \left(\partial_t \left(S - \frac{1}{2} A \right) + \bar{\partial}_i \left(U^i - \frac{1}{2} B^i \right) \right). \quad (\text{A.24})$$

Finally, to cancel all spurious terms of order Δt , we set

$$S = \frac{1}{2}A \quad \text{and} \quad U^i = \frac{1}{2}B^{\text{eq},i}, \quad (\text{A.25})$$

where $B^{\text{eq},i}$ denotes the equilibrium part¹ of B^i , given by

$$B^{\text{eq},i} = -\Gamma_{jk}^i \Pi^{\text{eq},jk} - \Gamma_{jk}^j \Pi^{\text{eq},ki} - \Gamma_{kj}^j \Pi^{\text{eq},ki}.$$

With this choice of S and U^i , Eq. (A.24) becomes

$$\partial_t \hat{\rho} + \bar{\partial}_i (\hat{\rho} \hat{u}^i) = A + \mathcal{O}(\Delta t^2),$$

which, after inserting the explicit expression for A (2.23), yields the correct continuity equation at second order in Δt :

$$\partial_t \hat{\rho} + \nabla_i (\hat{\rho} \hat{u}^i) = 0 + \mathcal{O}(\Delta t^2).$$

Momentum Equation

Adding $\varepsilon(A.18)$ and $\varepsilon^2(A.21)$ yields the momentum conservation equation:

$$\partial_t (\hat{\rho} \hat{u}^i) + \bar{\partial}_j \Pi^{(0),ij} = \bar{\partial}_j \sigma^{ij} + B^i + \frac{1}{\tau} U^i - \frac{\Delta t}{2} \partial_t B^i + \Delta t \left(1 - \frac{1}{2\tau}\right) \partial_t U^i.$$

Applying the same rescaling of the forcing term (A.23), together with the constraints (A.25), the momentum equation simplifies to

$$\partial_t (\hat{\rho} \hat{u}^i) + \bar{\partial}_j \Pi^{(0),ij} = \bar{\partial}_j \sigma^{ij} + B^i.$$

Inserting the explicit expression for B^i (2.24) and $\Pi^{(0),ij}$ (2.19) the covariant Navier-Stokes equation is recovered at second order in Δt :

$$\partial_t (\hat{\rho} \hat{u}^i) + \nabla_j (\hat{\rho} \hat{u}^i \hat{u}^j + \hat{\rho} c_s^2 g^{ij}) = \nabla_j \sigma^{ij} + \mathcal{O}(\Delta t^2),$$

where the explicit form of the viscous stress tensor σ^{ij} is given in Eq. (A.13).

¹Note that for second-order accuracy in Δt , it is sufficient to cancel the equilibrium part of $\Delta t B^i$ in Eq. (A.24), since the non-equilibrium part, $\Delta t B^{\text{neq},i}$, is of order $\mathcal{O}(\Delta t^2)$.

Newton's algorithm

The corrected density $\hat{\rho}$ and velocity \hat{u}^i are determined implicitly by the coupled Eqs. (A.14) and (A.15):

$$\begin{aligned}\hat{\rho} &= \rho + \Delta t S(\hat{\rho}, \hat{u}), \\ \hat{\rho} \hat{u}^i &= \rho u^i + \Delta t U^i(\hat{\rho}, \hat{u}),\end{aligned}$$

where S and U^i are given by Eqs. (A.25). Since $S(\hat{\rho}, \hat{u})$ and $U(\hat{\rho}, \hat{u})$ depend only linearly on $\hat{\rho}$, the density can be eliminated by defining $\mathcal{S}(\hat{u}) := S(\hat{\rho}, \hat{u})/\hat{\rho}$ and $\mathcal{U}(\hat{u}) := U(\hat{\rho}, \hat{u})/\hat{\rho}$. Now, we can rewrite Eqs. (A.14) and (A.15) as follows:

$$\frac{\rho}{\hat{\rho}} = 1 - \Delta t \mathcal{S}(\hat{u}), \quad \hat{u}^i = \frac{\rho}{\hat{\rho}} u^i + \Delta t \mathcal{U}^i(\hat{u}). \quad (\text{A.26})$$

Inserting the first equation into the second, we obtain an equation for \hat{u} which is decoupled from the density $\hat{\rho}$:

$$\hat{u}^i = (1 - \Delta t \mathcal{S}(\hat{u})) u^i + \Delta t \mathcal{U}^i(\hat{u}).$$

After defining $G^i(\hat{u}) := (1 - \Delta t \mathcal{S}(\hat{u})) u^i + \Delta t \mathcal{U}^i(\hat{u}) - \hat{u}^i$, Newton's algorithm can be used to solve $G^i(\hat{u}) = 0$. To this end, one assigns initial conditions $\hat{u}_{(0)}^i = u^i$ and iterates,

$$\hat{u}_{(n+1)}^i = \hat{u}_{(n)}^i - [J^{-1}]_j^i G^j(\hat{u}_{(n)}),$$

where $J = (\frac{dG^i}{d\hat{u}^j})$ denotes the Jacobian matrix. This procedure converges rapidly, and typically after 1–3 iterations, a sufficiently accurate solution is found. Given the solution for \hat{u} , the solution for $\hat{\rho}$ is obtained from Eq. (A.26).

A.1.2 Cancelation of discrete lattice effects by improved forcing term

Another way to cancel discrete lattice effects is to replace the original forcing term \mathcal{F}_λ in the LB equation (A.1) by an improved forcing term \mathcal{F}_λ^* , defined

by

$$\mathcal{F}_\lambda^*(x, t) := \mathcal{F}_\lambda(x, t) + \frac{1}{2} (\mathcal{F}_\lambda(x + c_\lambda \Delta t, t) - \mathcal{F}_\lambda(x, t - \Delta t)). \quad (\text{A.27})$$

With this forcing term, and after a Taylor expansion, the LB equation becomes

$$\Delta t D_t f_\lambda + \frac{\Delta t^2}{2!} D_t^2 f_\lambda + \dots = -\frac{1}{\tau} (f_\lambda - f_\lambda^{\text{eq}}) + \Delta t \mathcal{F}_\lambda + \frac{\Delta t^2}{2} D_t \mathcal{F}_\lambda + \dots,$$

where the dots denote higher order terms $\sim \mathcal{O}(\Delta t^3)$. This yields the following set of equations in the Chapman-Enskog expansion:

$$\mathcal{O}(\varepsilon^0) : \quad f_\lambda^{(0)} = f_\lambda^{\text{eq}}, \quad (\text{A.28})$$

$$\mathcal{O}(\varepsilon^1) : \quad D_t^{(1)} f_\lambda^{(0)} = -\frac{1}{\tau \Delta t} f_\lambda^{(1)} + \mathcal{F}_\lambda^{(1)}, \quad (\text{A.29})$$

$$\mathcal{O}(\varepsilon^2) : \quad \partial_t^{(2)} f_\lambda^{(0)} + \left(1 - \frac{1}{2\tau}\right) D_t^{(1)} f_\lambda^{(1)} = -\frac{1}{\tau \Delta t} f_\lambda^{(2)}. \quad (\text{A.30})$$

As can be seen, the spurious term $\frac{\Delta t}{2} D_t^{(1)} \mathcal{F}_\lambda^{(1)}$ in Eq. (A.5) got canceled and thus does not give rise to discrete lattice effects at order Δt . Correspondingly, the moments of Eqs. (A.29) and (A.30) are given by

$$\sum_\lambda (A.29) \sqrt{g} : \quad \partial_t^{(1)} \rho + \bar{\partial}_i^{(1)} (\rho u^i) = A^{(1)}, \quad (\text{A.31})$$

$$\sum_\lambda c_\lambda^i (A.29) \sqrt{g} : \quad \partial_t^{(1)} (\rho u^i) + \bar{\partial}_j^{(1)} \Pi^{(0),ij} = B^{(1),i}, \quad (\text{A.32})$$

$$\sum_\lambda (A.30) \sqrt{g} : \quad \partial_t^{(2)} \rho = 0, \quad (\text{A.33})$$

$$\sum_\lambda c_\lambda^i (A.30) \sqrt{g} : \quad \partial_t^{(2)} (\rho u^i) = \bar{\partial}_j^{(1)} \sigma^{(1),ij}, \quad (\text{A.34})$$

where A and B^i are the moments of the forcing term (2.23-2.24), $\bar{\partial}_i := \partial_i - \Gamma_{ij}^j$, and $\sigma^{(1),ij}$ is the viscous stress tensor (A.10). Summing $\varepsilon \cdot (A.31)$ and $\varepsilon^2 \cdot (A.33)$, we obtain the continuity equation at second order in Δt :

$$\partial_t \rho + \nabla_i (\rho u^i) = 0 + \mathcal{O}(\Delta t^2). \quad (\text{A.35})$$

On the other hand, summing $\varepsilon \cdot (A.32)$ and $\varepsilon^2 \cdot (A.34)$ yields the momentum equation at second order in Δt :

$$\partial_t (\rho u^i) + \nabla_j (\rho u^i u^j + \rho c_s^2 g^{ij}) = \nabla_j \sigma^{ij} + \mathcal{O}(\Delta t^2). \quad (\text{A.36})$$

where σ^{ij} is given by Eq. (A.13).

A.2 Improved discrete gradient operator

By using the lattice symmetry relations (2.14), it can be proven that the following formula yields the gradient operator at fourth order in the lattice spacing Δt :

$$\partial_i f(x) = \frac{1}{c_s^2 \Delta t} \sum_{\lambda} w_{\lambda} c_{\lambda}^i \left(f(x + c_{\lambda} \Delta t) - \frac{c_s^2 \Delta t^2}{2} (\Delta f)(x + c_{\lambda} \Delta t) \right) + \mathcal{O}(\Delta t^4). \quad (\text{A.37})$$

To this end, we consider the Taylor expansion of $f(x + c_{\lambda} \Delta t)$ in Δt , given by

$$\begin{aligned} f(x + c_{\lambda} \Delta t) &= f(x) + \Delta t c_{\lambda}^j \partial_j f(x) + \frac{\Delta t^2}{2!} c_{\lambda}^j c_{\lambda}^k \partial_j \partial_k f(x) \\ &\quad + \frac{\Delta t^3}{3!} c_{\lambda}^j c_{\lambda}^k c_{\lambda}^l \partial_j \partial_k \partial_l f(x) + \frac{\Delta t^4}{4!} c_{\lambda}^j c_{\lambda}^k c_{\lambda}^l c_{\lambda}^m \partial_j \partial_k \partial_l \partial_m f(x) + \mathcal{O}(\Delta t^5) \end{aligned}$$

Taking the sum of the Taylor expansion yields

$$\sum_{\lambda} w_{\lambda} c_{\lambda}^i f(x + c_{\lambda} \Delta t) = \Delta t c_s^2 \partial_i f(x) + \frac{\Delta t^3}{2} c_s^4 \partial_i (\Delta f)(x) + \mathcal{O}(\Delta t^5), \quad (\text{A.38})$$

where we have used the lattice symmetry relations (2.14). In order to subtract the remaining spurious term at order Δt^3 , we precompute the Laplacian Δf by using the discrete Laplacian operator (2.36),

$$(\Delta f)(x) = \frac{2}{c_s^2 \Delta t^2} \sum_{\lambda} w_{\lambda} (f(x + c_{\lambda} \Delta t) - f(x)) + \mathcal{O}(\Delta t^2).$$

The gradient of Δf can then be calculated from Eq. (2.35),

$$\partial_i (\Delta f)(x) = \frac{1}{c_s^2 \Delta t} \sum_{\lambda} w_{\lambda} c_{\lambda}^i (\Delta f)(x + c_{\lambda} \Delta t) + \mathcal{O}(\Delta t^2). \quad (\text{A.39})$$

Summing up Eq. (A.38) and (A.39) with appropriate prefactors of c_s and Δt directly yields Eq. (A.37).

References

- [1] M. Mendoza, S. Succi, and H. J. Herrmann, “Flow through randomly curved manifolds,” *Scientific reports*, vol. 3, 2013.
- [2] M. Mendoza, J.-D. Debus, S. Succi, and H. Herrmann, “Lattice kinetic scheme for generalized coordinates and curved spaces,” *International Journal of Modern Physics C*, 2014.
- [3] F. A. Dullien, *Porous media: fluid transport and pore structure*. Academic press, 2012.
- [4] S. Succi and R. Benzi, “Lattice boltzmann equation for quantum mechanics,” *Physica D: Nonlinear Phenomena*, vol. 69, no. 3, pp. 327–332, 1993.
- [5] F. de Juan, M. Sturla, and M. A. Vozmediano, “Space dependent fermi velocity in strained graphene,” *Physical review letters*, vol. 108, no. 22, p. 227205, 2012.
- [6] M. Oliva-Leyva and G. G. Naumis, “Generalizing the fermi velocity of strained graphene from uniform to nonuniform strain,” *Physics Letters A*, vol. 379, no. 40, pp. 2645–2651, 2015.
- [7] W. Dean, “Fluid motion in a curved channel,” *Proceedings of the Royal Society of London. Series A*, vol. 121, no. 787, pp. 402–420, 1928.
- [8] G. Häammerlin, “Die stabilität der strömung in einem gekrümmten kanal,” *Archive for rational mechanics and analysis*, vol. 1, no. 1, pp. 212–224, 1957.

- [9] D. B. Brewster, P. Grosberg, and A. H. Nissan, “The stability of viscous flow between horizontal concentric cylinders,” *Proceedings of the Royal Society of London. Series A. Mathematical and Physical Sciences*, vol. 251, no. 1264, pp. 76–91, 1959.
- [10] W. H. Finlay, J. B. Keller, and J. H. Ferziger, “Instability and transition in curved channel flow,” *Journal of Fluid Mechanics*, vol. 194, pp. 417–456, 1988.
- [11] W. H. Finlay, “Perturbation expansion and weakly nonlinear analysis for twodimensional vortices in curved or rotating channels,” *Physics of Fluids A: Fluid Dynamics (1989-1993)*, vol. 1, no. 5, pp. 854–860, 1989.
- [12] W. Finlay and K. Nandakumar, “Onset of two-dimensional cellular flow in finite curved channels of large aspect ratio,” *Physics of Fluids A: Fluid Dynamics (1989-1993)*, vol. 2, no. 7, pp. 1163–1174, 1990.
- [13] “Soap bubble.” <https://www.pexels.com/photo/colorful-ball-float-soap-bubble-35089>. Accessed: 2016-08-26.
- [14] L. D. Landau and E. Lifshitz, *The classical theory of fields*, vol. 2. Butterworth-Heinemann, 1975.
- [15] F. Seychelles, Y. Amarouchene, M. Bessafi, and H. Kellay, “Thermal convection and emergence of isolated vortices in soap bubbles,” *Physical review letters*, vol. 100, no. 14, p. 144501, 2008.
- [16] J. Chomaz, “The dynamics of a viscous soap film with soluble surfactant,” *Journal of Fluid Mechanics*, vol. 442, pp. 387–409, 2001.
- [17] J. Zhang, S. Childress, A. Libchaber, and M. Shelley, “Flexible filaments in a flowing soap film as a model for one-dimensional flags in a two-dimensional wind,” *Nature*, vol. 408, no. 6814, pp. 835–839, 2000.
- [18] S. Reuther and A. Voigt, “The interplay of curvature and vortices in flow on curved surfaces,” *Multiscale Modeling & Simulation*, vol. 13, no. 2, pp. 632–643, 2015.

REFERENCES

- [19] S. Vivek and E. R. Weeks, “Measuring and overcoming limits of the saffman-delbrück model for soap film viscosities,” *PloS one*, vol. 10, no. 3, p. e0121981, 2015.
- [20] “Bacillus subtilis.” https://en.wikipedia.org/wiki/File:Bacillus_subtilis.jpg, 2007. Accessed: 2016-08-26.
- [21] “Pore schematic.” https://en.wikipedia.org/wiki/File:Pore_schematic.svg, 2009. Accessed: 2016-08-26.
- [22] M. Raff, B. Alberts, J. Lewis, A. Johnson, and K. Roberts, *Molecular Biology of the Cell 4th edition*. National Center for Biotechnology Information’s Bookshelf, 2002.
- [23] M. Arroyo and A. DeSimone, “Relaxation dynamics of fluid membranes,” *Physical Review E*, vol. 79, no. 3, p. 031915, 2009.
- [24] J. W. Barrett, H. Garcke, and R. Nürnberg, “Numerical computations of the dynamics of fluidic membranes and vesicles,” *Physical Review E*, vol. 92, no. 5, p. 052704, 2015.
- [25] D. Hu, P. Zhang, and E. Weinan, “Continuum theory of a moving membrane,” *Physical Review E*, vol. 75, no. 4, p. 041605, 2007.
- [26] J. Fan, T. Han, and M. Haataja, “Hydrodynamic effects on spinodal decomposition kinetics in planar lipid bilayer membranes,” *The Journal of chemical physics*, vol. 133, no. 23, p. 235101, 2010.
- [27] R. Dimova, S. Aranda, N. Bezlyepkina, V. Nikolov, K. A. Riske, and R. Lipowsky, “A practical guide to giant vesicles. probing the membrane nanoregime via optical microscopy,” *Journal of Physics: Condensed Matter*, vol. 18, no. 28, p. S1151, 2006.
- [28] P. Cicuta, S. L. Keller, and S. L. Veatch, “Diffusion of liquid domains in lipid bilayer membranes,” *The Journal of Physical Chemistry B*, vol. 111, no. 13, pp. 3328–3331, 2007.

- [29] M. B. Amar, J.-M. Allain, N. Puff, and M. Angelova, “Stokes instability in inhomogeneous membranes: application to lipoprotein suction of cholesterol-enriched domains,” *Physical review letters*, vol. 99, no. 4, p. 044503, 2007.
- [30] L. Scriven, “On the dynamics of phase growth,” *Chemical Engineering Science*, vol. 10, no. 1, pp. 1–13, 1959.
- [31] K. D. Danov, R. Dimova, and B. Pouliquen, “Viscous drag of a solid sphere straddling a spherical or flat surface,” *Physics of Fluids (1994-present)*, vol. 12, no. 11, pp. 2711–2722, 2000.
- [32] E. R. Priest, “Solar magnetohydrodynamics,” *Springer*, 1982.
- [33] C. Cao, M. A. Rammaha, and E. S. Titi, “The navier-stokes equations on the rotating 2-d sphere: Gevrey regularity and asymptotic degrees of freedom,” *Zeitschrift für angewandte Mathematik und Physik ZAMP*, vol. 50, no. 3, pp. 341–360, 1999.
- [34] A. K. Geim and K. S. Novoselov, “The rise of graphene,” *Nature materials*, vol. 6, no. 3, pp. 183–191, 2007.
- [35] A. K. Geim, “Graphene: status and prospects,” *science*, vol. 324, no. 5934, pp. 1530–1534, 2009.
- [36] S. D. Sarma, S. Adam, E. Hwang, and E. Rossi, “Electronic transport in two-dimensional graphene,” *Reviews of Modern Physics*, vol. 83, no. 2, p. 407, 2011.
- [37] A. C. Neto, F. Guinea, N. M. Peres, K. S. Novoselov, and A. K. Geim, “The electronic properties of graphene,” *Reviews of modern physics*, vol. 81, no. 1, p. 109, 2009.
- [38] I. Torre, A. Tomadin, A. K. Geim, and M. Polini, “Nonlocal transport and the hydrodynamic shear viscosity in graphene,” *Physical Review B*, vol. 92, no. 16, p. 165433, 2015.

REFERENCES

- [39] M. Mendoza, H. Herrmann, and S. Succi, “Preturbulent regimes in graphene flow,” *Phys. Rev. Lett.*, vol. 106, no. 15, p. 156601, 2011.
- [40] Y. Mao, W. L. Wang, D. Wei, E. Kaxiras, and J. G. Sodroski, “Graphene structures at an extreme degree of buckling,” *ACS Nano*, vol. 5, no. 2, pp. 1395–1400, 2011. PMID: 21222462.
- [41] L. H. Rohwedder, “Dirac cone.” <https://commons.wikimedia.org/wiki/File:DoubleCone.png>, 2006. Accessed: 2016-08-26.
- [42] A. Fasolino, J. Los, and M. I. Katsnelson, “Intrinsic ripples in graphene,” *Nature materials*, vol. 6, no. 11, pp. 858–861, 2007.
- [43] J. C. Meyer, A. K. Geim, M. I. Katsnelson, K. S. Novoselov, T. J. Booth, and S. Roth, “The structure of suspended graphene sheets,” *Nature*, vol. 446, no. 7131, pp. 60–63, 2007.
- [44] X. Shan, X.-F. Yuan, and H. Chen, “Kinetic theory representation of hydrodynamics: a way beyond the navier-stokes equation,” *Journal of Fluid Mechanics*, vol. 550, no. 1, pp. 413–441, 2006.
- [45] S. Succi, *The lattice Boltzmann equation: for fluid dynamics and beyond*. Oxford university press, 2001.
- [46] J. G. Zhou, “Axisymmetric lattice boltzmann method,” *Phys. Rev. E*, vol. 78, p. 036701, Sep 2008.
- [47] P. Dellar, D. Lapitski, S. Palpacelli, and S. Succi, “Isotropy of three-dimensional quantum lattice boltzmann schemes,” *Physical Review E*, vol. 83, no. 4, p. 046706, 2011.
- [48] D. Lapitski and P. J. Dellar, “Convergence of a three-dimensional quantum lattice boltzmann scheme towards solutions of the dirac equation,” *Philosophical Transactions of the Royal Society of London A: Mathematical, Physical and Engineering Sciences*, vol. 369, no. 1944, pp. 2155–2163, 2011.

- [49] S. Succi, “Lattice boltzmann 2038,” *Europhys. Lett.*, vol. 109, no. 5, p. 50001, 2015.
- [50] R. Benzi, S. Succi, and M. Vergassola, “The lattice boltzmann equation: theory and applications,” *Physics Reports*, vol. 222, no. 3, pp. 145–197, 1992.
- [51] S. Chen and G. D. Doolen, “Lattice boltzmann method for fluid flows,” *Annual review of fluid mechanics*, vol. 30, no. 1, pp. 329–364, 1998.
- [52] M. Mendoza and J. D. Munoz, “Three-dimensional lattice boltzmann model for electrodynamics,” *Physical Review E*, vol. 82, no. 5, p. 056708, 2010.
- [53] M. Mendoza and J. D. Munoz, “Three-dimensional lattice boltzmann model for magnetic reconnection,” *Physical Review E*, vol. 77, no. 2, p. 026713, 2008.
- [54] M. Mendoza, B. M. Boghosian, H. J. Herrmann, and S. Succi, “Fast lattice boltzmann solver for relativistic hydrodynamics,” *Physical review letters*, vol. 105, no. 1, p. 014502, 2010.
- [55] Z. Guo, C. Zheng, and B. Shi, “Discrete lattice effects on the forcing term in the lattice boltzmann method,” *Phys. Rev. E*, vol. 65, p. 046308, Apr 2002.
- [56] Y. Choquet-Bruhat, *General relativity and the Einstein equations*. Oxford University Press, 2009.
- [57] P. L. Bhatnagar, E. P. Gross, and M. Krook, “A model for collision processes in gases. i. small amplitude processes in charged and neutral one-component systems,” *Phys. Rev.*, vol. 94, pp. 511–525, May 1954.
- [58] S. Chapman and T. G. Cowling, *The mathematical theory of non-uniform gases: an account of the kinetic theory of viscosity, thermal conduction and diffusion in gases*. Cambridge university press, 1970.

REFERENCES

- [59] C. Cercignani, *The Boltzmann equation*. Springer, 1988.
- [60] X. He, S. Chen, and G. D. Doolen, “A novel thermal model for the lattice boltzmann method in incompressible limit,” *Journal of Computational Physics*, vol. 146, no. 1, pp. 282–300, 1998.
- [61] S. P. Thampi, S. Ansumali, R. Adhikari, and S. Succi, “Isotropic discrete laplacian operators from lattice hydrodynamics,” *Journal of Computational Physics*, vol. 234, pp. 1–7, 2013.
- [62] J.-D. Debus, M. Mendoza, and H. J. Herrmann, “Dean instability in double-curved channels,” *Physical Review E*, vol. 90, no. 5, p. 053308, 2014.
- [63] Y. Guo and W. Finlay, “Splitting, merging and wavelength selection of vortices in curved and/or rotating channel flow due to eckhaus instability,” *Journal of Fluid Mechanics*, vol. 228, pp. 661–691, 1991.
- [64] P. E. Haines, J. P. Denier, and A. P. Bassom, “Dean vortices in finite-aspect-ratio ducts,” *Journal of Fluid Mechanics*, vol. 716, p. R8, 2013.
- [65] J.-D. Debus, M. Mendoza, S. Succi, and H. Herrmann, “Poiseuille flow in curved spaces,” *Physical Review E*, vol. 93, no. 4, p. 043316, 2016.
- [66] M. Rivera, P. Vorobieff, and R. E. Ecke, “Turbulence in flowing soap films: velocity, vorticity, and thickness fields,” *Physical review letters*, vol. 81, no. 7, p. 1417, 1998.
- [67] G. Zhao-Li, Z. Chu-Guang, and S. Bao-Chang, “Non-equilibrium extrapolation method for velocity and pressure boundary conditions in the lattice boltzmann method,” *Chinese Physics*, vol. 11, no. 4, p. 366, 2002.
- [68] M. Kness, “Colorpy - a python package for handling physical descriptions of color and light spectra.” <http://www.markness.net/colorpy/ColorPy.html>, 2008. Accessed: 2016-07-12.

- [69] H. Darcy, *Des principes à suivre et des formules à employer dans les questions de distribution d'eau*. Victor Dalmont, 1856.
- [70] A. Zhukov, R. Bouffanais, N. N. Konobeeva, and M. Belonenko, “On the electronic spectrum in curved graphene nanoribbons,” *JETP letters*, vol. 97, no. 7, pp. 400–403, 2013.
- [71] F. de Juan, A. Cortijo, and M. A. Vozmediano, “Charge inhomogeneities due to smooth ripples in graphene sheets,” *Physical Review B*, vol. 76, no. 16, p. 165409, 2007.
- [72] M. Arminjon and F. Reifler, “Basic quantum mechanics for three dirac equations in a curved spacetime,” *Brazilian Journal of Physics*, vol. 40, no. 2, pp. 242–255, 2010.
- [73] J. Yepez, “Einstein’s vierbein field theory of curved space,” *arXiv preprint arXiv:1106.2037*, 2011.
- [74] M. Arminjon and F. Reifler, “Equivalent forms of dirac equations in curved space-times and generalized de broglie relations,” *Brazilian Journal of Physics*, vol. 43, no. 1-2, pp. 64–77, 2013.
- [75] D. R. Brill and J. A. Wheeler, “Interaction of neutrinos and gravitational fields,” *Reviews of Modern Physics*, vol. 29, no. 3, p. 465, 1957.
- [76] F. Toyama and Y. Nogami, “Harmonic oscillators in relativistic quantum mechanics,” *Physical Review A*, vol. 59, no. 2, p. 1056, 1999.
- [77] A. Chaves, T. Frederico, O. Oliveira, W. De Paula, and M. Santos, “Optical conductivity of curved graphene,” *Journal of Physics: Condensed Matter*, vol. 26, no. 18, p. 185301, 2014.
- [78] Y. Zheng and T. Ando, “Hall conductivity of a two-dimensional graphite system,” *Physical Review B*, vol. 65, no. 24, p. 245420, 2002.
- [79] T. T. Hormel, S. Q. Kurihara, M. K. Brennan, M. C. Wozniak, and R. Parthasarathy, “Measuring lipid membrane viscosity using rotational

- and translational probe diffusion,” *Physical review letters*, vol. 112, no. 18, p. 188101, 2014.
- [80] C. H. Gibson, “Turbulent mixing, viscosity, diffusion, and gravity in the formation of cosmological structures: The fluid mechanics of dark matter,” *Journal of Fluids Engineering*, vol. 122, no. 4, pp. 830–835, 2000.
- [81] M. Bento, O. Bertolami, and A. Sen, “Generalized chaplygin gas, accelerated expansion, and dark-energy-matter unification,” *Physical Review D*, vol. 66, no. 4, p. 043507, 2002.
- [82] Y. Zhang, Y.-W. Tan, H. L. Stormer, and P. Kim, “Experimental observation of the quantum hall effect and berry’s phase in graphene,” *Nature*, vol. 438, no. 7065, pp. 201–204, 2005.
- [83] F. Bösch, S. S. Chikatamarla, and I. V. Karlin, “Entropic multirelaxation lattice boltzmann models for turbulent flows,” *Physical Review E*, vol. 92, no. 4, p. 043309, 2015.
- [84] N. Frapolli, S. Chikatamarla, and I. Karlin, “Multispeed entropic lattice boltzmann model for thermal flows,” *Physical Review E*, vol. 90, no. 4, p. 043306, 2014.
- [85] G. Strang, “On the construction and comparison of difference schemes,” *SIAM Journal on Numerical Analysis*, vol. 5, no. 3, pp. 506–517, 1968.
- [86] E. Ilseven and M. Mendoza, “Lattice boltzmann model for numerical relativity,” *Physical Review E*, vol. 93, no. 2, p. 023303, 2016.
- [87] D. A. Wolf-Gladrow, *Lattice-gas cellular automata and lattice Boltzmann models: an introduction*. Springer Science & Business Media, 2000.
- [88] J. M. Buick and C. A. Created, “Gravity in a lattice boltzmann model,” *Phys. Rev. E*, vol. 61, pp. 5307–5320, May 2000.

- [89] Q. Li, Y. L. He, G. H. Tang, and W. Q. Tao, “Improved axisymmetric lattice boltzmann scheme,” *Phys. Rev. E*, vol. 81, p. 056707, May 2010.